# Microstability and turbulence in high-performance tokamak plasmas

Oliver Beeke
Exeter College
University of Oxford

A thesis submitted for the degree of
*Doctor of Philosophy in Theoretical Physics*

Hilary 2023

# Microstability and turbulence in high-performance tokamak plasmas

Oliver Beeke

Exeter College, University of Oxford

*Submitted for the degree of Doctor of Philosophy in Theoretical Physics*

Hilary 2023

Turbulence, driven by microscale instabilities, is known to reduce the performance of fusion devices by exacerbating the radial transport of heat and particles from the high-pressure core where fusion can occur. In this Thesis, we study two ways of reducing this turbulent transport, focusing in particular on microstability and turbulence at high plasma pressure where electromagnetic effects are important. Local $\delta f$ gyrokinetic simulations are used throughout. We uncover a novel destabilizing effect of increased elongation that is manifest in plasmas with steep pressure gradients. This is explained as the competition between local magnetic shear and finite-Larmor-radius damping as elongation is varied. At high $\beta$, we show that this effect can lead to the removal of second stability of the kinetic ballooning mode (KBM) with increased elongation, which could have severe implications for future high-performance tokamaks for which access to second stability is crucial for good performance. In the second half of the Thesis, we study a JET pulse exhibiting an internal transport barrier in the ion temperature. By a combination of linear and nonlinear studies, we determine a mechanism that allows the steepest radial gradients of temperature to coexist with low levels of transport. We propose that electromagnetic effects stabilize the ion-temperature-gradient instabilities that otherwise drive significant transport well above experimental levels. The KBM that is usually destabilized at high plasma $\beta$ is stabilized by significant negative magnetic shear, and equilibrium flow shear should be avoided as it rapidly destabilizes the KBM via the parallel velocity gradient. In determining this mechanism, we matched experimental fluxes simultaneously in multiple transport channels at multiple radial locations, validating the use of local $\delta f$ gyrokinetics for the further study of transport barriers.

# Acknowledgements

During the past few years spent working towards this Thesis, I have had the good fortune of meeting some wonderful people without whom this process would have been far more challenging. I could not imagine a better mentor to guide me through my DPhil than Michael Barnes. Not only does he have a brilliant mind and an ability to communicate complex ideas succinctly, but he has also been caring and supportive when I have needed it most. I would also like to thank Michele for helping me with the experimental side of my work and introducing me to the JT-60SA collaboration.

I would like to acknowledge, in particular, the members of the Oxford plasma theory group who had the misfortune of enduring my ongoing cereal addiction when we shared the same office space over the past 3 years. To Mantas, Nicolas, Michael H and Alexander, thank you for keeping our work environment precariously balanced on the boundary between intellectual stimulation and friendly banter. To the rest of the ‘Plasmaniacs’ (special mentions go to Juan, Plamen, Valerian, Alessandro and Toby) with whom I was lucky enough to cross paths during my time at Oxford, thank you for all the good times we shared over the years during lunches, seminars and more.

I’d also like to thank the Exeter MCR community, in particular Kate and Thomas, for making me feel so welcome at Exeter college, and OUES members like Patrick, Wes and Cal for the good times both on and off the (virtual) pitch. To Chris and Amane, little did I know that my adjacent roommates would end up being my closest friends for years to come – thank you for all the good memories we’ve made together. To my partner Jess –

we are just a short way into our time together, but you've already made me immeasurably happy and I can't wait to continue our journey.

Finally, I would like to thank my family – in particular my parents. No words can describe how much they have supported me and shaped my character. My successes are a reflection of the sacrifices they have made to get me here, and I am infinitely grateful to them both.

# Contents

# List of Figures

# Chapter 1

# Introduction

The challenge of effecting terrestrial nuclear fusion for energy production is fascinating and complex. It brings together scientists and engineers from a wide variety of fields including plasma physics, materials science and structural engineering. Not only does it require the understanding of complex phenomena to control and harness the energy source that powers our sun, but it also provides an opportunity to tackle significant real-world issues such as climate change. In this Thesis, we will explore the plasma instabilities and turbulence that exist in magnetic confinement fusion devices called tokamaks. Specifically, we focus on relatively exotic equilibria that contain steep gradients of mean plasma parameters such as temperature and pressure. In doing so, we answer questions about the validity of the so-called gyrokinetic framework to model these exotic systems, and unearth novel phenomena along the way that may have significant consequences for transport in high-performance tokamaks.

In the remainder of this Chapter, we will introduce some basic concepts and themes that are used and developed throughout this Thesis. We begin in Section 1.1 by introducing the motivation behind the use of terrestrial nuclear fusion as a source of energy. In Section 1.2, we introduce some of the fundamental concepts central to magnetic confinement fusion, including the microscale instabilities that drive 'stiff' transport in tokamaks. Section 1.3 introduces the local $\delta f$ gyrokinetic framework that is often used to study microscale instabilities and transport via codes such as `GS2`, which is used throughout this Thesis [1, 2]. In Section 1.4, we present the physical basis for some mechanisms, referenced throughout this Thesis, that can mitigate the microinstabilities. Finally, in Section 1.5, we present the main contributions of this Thesis along with an outline of the remaining chapters.

## 1.1 Motivation

It is generally accepted within the relevant scientific communities that one of the major threats to humanity is man-made climate change caused by the release of greenhouse gases into the Earth's atmosphere [3]. These gases are generally produced by burning traditional fuels, such as oil and gas, for energy. Alternative energy sources exist, but all have associated drawbacks that hinder their uptake as significant contributors to the grid. Nuclear fission, for example, can produce significant energy on demand, but its public perception is tainted by the very-real issues that it produces long-lived radioactive waste and has the potential for catastrophic failure [4]. Renewables such as wind and solar produce no by-products, but cannot be relied upon for constant energy production without significant improvements being made to electricity storage infrastructure [5]. In comparison, nuclear fusion, the process by which a heavier final-state nucleus is produced from multiple lighter initial-state nuclei, is relatively flawless. It produces no carbon emissions or long-lived radioactive waste, has abundant fuel and is not reliant on weather for continuous power output. However, until late 2022, the scientific community had failed to demonstrate net energy production using terrestrial nuclear fusion [6]. In fact, the closest to break-even up to that point was at the Joint European Torus (JET) experiment in 1997, which produced via fusion 62% of the input heating power [7]. This, however, does not take into account the power required to generate the magnetic fields used to confine the fusion plasma. Nor does it take into account the engineering losses associated with transforming the heat energy extracted to electrical energy. Before we explain some of the key challenges facing nuclear fusion from a microstability perspective, we first describe the process itself and how we try to effect it on Earth.

## 1.2 Fundamentals of Terrestrial Nuclear Fusion

Nuclear fusion is governed by the competing effects of the mutual electrostatic repulsion between nuclei and the attractive strong nuclear force. The electrostatic Coulomb force is weak but long ranged compared to the strong nuclear force, which can only act over nuclear length scales. To get close enough for fusion to occur, nuclei must be energetic enough to overcome the electrostatic potential barrier. The temperatures[1] required for an appreciable fusion rate are of order $10^4 - 10^5$ eV, depending on the reactants. At these energies, atoms are fully ionized and exist in a plasma state with free nuclei and electrons. Without applying any confinement measures, a volume of such hot plasma would expand rapidly and damage whatever material vessel were being used to contain it. For context, the energy stored within the JET tokamak is of order $10^7$ J – enough to melt around 10 kg of steel initially at room temperature.

### 1.2.1 Tokamak equilibria

Stars, which are powered by nuclear fusion, use their own gravity to confine the plasma, but this is clearly not feasible on Earth. Instead, we confine plasma using the fact that moving charged particles, under the influence of the Lorentz force, follow helical orbits around magnetic field lines. The orbit radius is known as the gyro- or Larmor radius. Consequently, the plasma's constituent particles are confined perpendicular to field lines but can stream rapidly along them. As a result, any device with magnetic field lines that intersect exclusively the device walls will still exhibit poor confinement. To avoid this, most modern fusion devices, known as tokamaks, use an axisymmetric toroidal magnetic field topology. The equilibrium magnetic field is comprised of toroidal and poloidal components as illustrated schematically in Figure 1.1. We denote the toroidal and poloidal angles via $\zeta$ and $\theta$, respectively. The toroidal component of the confining magnetic field is generated by external field coils that wrap around the plasma, much like a solenoid bent around on itself. The poloidal component is sourced by a current that runs through the plasma itself; this current can be induced externally

---

[1] Throughout this Thesis, we will use energy and temperature interchangeably, ignoring the Boltzmann constant for brevity.

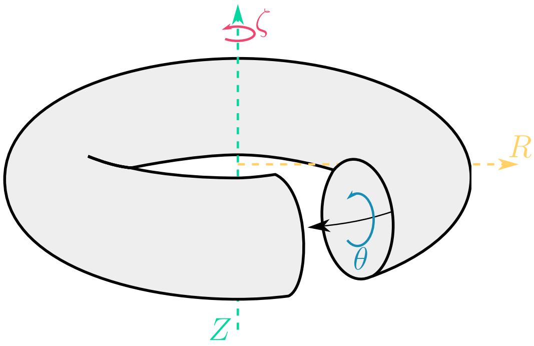

Figure 1.1: A schematic illustration of the topology of a torus. The axis of symmetry, known as the major axis, is shown by the green dashed line, and is in the $Z$ direction. The minor axis is denoted by the black arrow traced through the core of the torus; the poloidal direction is around this minor axis. The toroidal and poloidal angles are denoted by $\zeta$ and $\theta$, respectively. The major radius, denoted by $R$, is the perpendicular distance from the major axis.

(e.g. via transformer action or the injection of radio-frequency (RF) waves into the plasma) or generated intrinsically (e.g. via the toroidal bootstrap current which is driven in the presence of an inhomogeneous magnetic field and pressure gradients [8]).

Mathematically, the equilibrium magnetic field $\boldsymbol{B}$ can be expressed in multiple ways. The first of these is the Clebsch representation [9]:

$$\boldsymbol{B} = \nabla\tilde{\alpha} \times \nabla\tilde{\psi}, \tag{1.1}$$

where $\tilde{\alpha}$ labels a field line and $\tilde{\psi}$ is the poloidal magnetic flux. Tildes are used to distinguish these coordinates from other quantities, such as the ballooning parameter $\alpha_{\text{MHD}}$, that have a well-established notation in the literature. The other representation we will use explicitly separates the toroidal and poloidal components of the magnetic field:

$$\boldsymbol{B} = \underbrace{I\nabla\zeta}_{\text{toroidal}} + \underbrace{\nabla\zeta \times \nabla\tilde{\psi}}_{\text{poloidal}}, \tag{1.2}$$

where $I$ is the poloidal current function[2]. By combining these two representations of $\boldsymbol{B}$, we can derive an expression for $\tilde{\alpha}$:

$$\tilde{\alpha} = \zeta - \int_0^\theta \mathrm{d}\theta' \tilde{q}(\tilde{\psi}, \theta'), \tag{1.3}$$

---

[2] The poloidal current function is named as such because it represents the poloidal current that sources the toroidal magnetic field.

where $\tilde{q} \equiv \boldsymbol{B} \cdot \nabla\zeta / \boldsymbol{B} \cdot \nabla\theta$ is the *local* safety factor, which is a function of poloidal angle. The *global* safety factor is defined as

$$q \equiv \frac{1}{2\pi} \int_0^{2\pi} \tilde{q}(\tilde{\psi}, \theta) \mathrm{d}\theta, \tag{1.4}$$

although we will henceforth refer to it simply as the safety factor for brevity. The safety factor is a measure of the relative strength of the toroidal and poloidal components of the magnetic field – when it is an irrational number, a field line traces out an infinite path without ever intersecting itself. The resulting 2D surface traced out by this path is known as a flux surface, since the poloidal magnetic flux is constant on it. The core of the tokamak, where magnetic field lines do not intersect the device walls at any point, can be described as a nested set of closed flux surfaces.

In equilibrium, the magnetic and thermal forces that exist in magnetized plasma are balanced. One way of determining a self-consistent equilibrium is to model the plasma as a conducting fluid – this is known as magnetohydrodynamics (MHD). Assuming the plasma has zero resistivity and exists in steady state, the equation that describes force-balance reduces to

$$\boldsymbol{j} \times \boldsymbol{B} = \nabla p, \tag{1.5}$$

where $\boldsymbol{j}$ and $p$ are the equilibrium current density and pressure, respectively. Noting that $\boldsymbol{B} \cdot \nabla p = 0$, we see that the pressure is constant on magnetic flux surfaces. This is a natural consequence of particles' ability to move rapidly parallel to the magnetic field to eliminate inhomogeneities in equilibrium parameters such as temperature and density. By combining Ampère's law, Equation 1.2 and Equation 1.5 in cylindrical $\{R, \zeta, Z\}$ coordinates, one can derive the Grad-Shafranov equation:

$$\Delta^* \psi = -4\pi R^2 \frac{dp}{d\psi} - I \frac{dI}{d\psi}, \tag{1.6}$$

where

$$\Delta^* \equiv \frac{\partial^2}{\partial R^2} - \frac{1}{R} \frac{\partial}{\partial R} + \frac{\partial^2}{\partial Z^2}, \tag{1.7}$$

and $R$ and $Z$ are defined in Figure 1.1 [10, 11]. This is a nonlinear, elliptical partial differential equation (PDE) that can generally only be solved numerically.

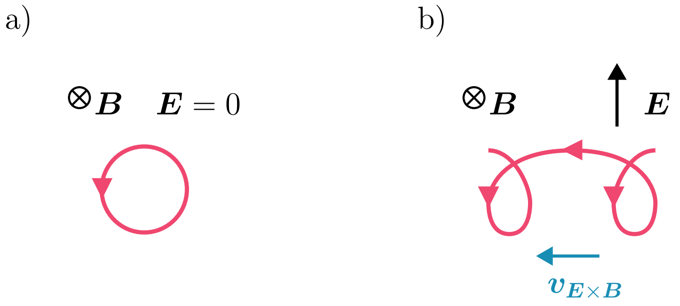

Figure 1.2: An illustration of the $\boldsymbol{E} \times \boldsymbol{B}$ drift. In a), an ion orbits in the plane perpendicular to a magnetic field $\boldsymbol{B}$ that points into the page. In b), a constant electric field $\boldsymbol{E}$ is applied. This applies to the ion an acceleration parallel to $\boldsymbol{E}$. This acceleration increases the ion's orbit radius as it travels parallel to $\boldsymbol{E}$, and vice versa. As a result, there is a net motion of the particle perpendicular to both $\boldsymbol{E}$ and $\boldsymbol{B}$.

### 1.2.2 Transport in tokamaks

At the edge of a tokamak, field lines intersect the physical walls of the device at designated strike points which can be actively cooled to further resist the thermal damage from plasma that impinges upon them [12]. Nevertheless, there are material limits to the durability of these strike points, so the plasma at the edge of the device should be sufficiently cool and diffuse to not damage them. This requires that gradients of temperature and density exist from the core of the plasma, where conditions must be fusion-relevant, to the cool, diffuse edge region. To maximise the volume of fusing plasma, we require a steep pressure gradient close to the edge of the plasma. However, particles confined to one flux surface can collide with those confined to nearby (i.e. within a few Larmor radii) flux surfaces, leading to collisional transport of heat. This collisional transport limits the maximum temperature gradient that can be sustained for a given heat loss rate.

However, collisional transport contributes relatively little towards the overall transport, which typically is driven primarily by turbulence. To understand the origin of turbulence in tokamaks, we must first introduce the concept of magnetic drifts. When a charged particle moves in constant electric and magnetic fields $\boldsymbol{E}$ and $\boldsymbol{B}$ that are perpendicular to one another, it undergoes a net drift perpendicular to both fields. This process is illustrated in Figure 1.2. This magnetic drift is known as the $\boldsymbol{E} \times \boldsymbol{B}$

drift, since the drift velocity is

$$\boldsymbol{v}_{E\times B} = \frac{c}{B^2}\boldsymbol{E}\times\boldsymbol{B}, \tag{1.8}$$

where the speed of light in a vacuum $c$ enters as we work in Gaussian units. For similar reasons, magnetic drifts also occur in the presence of non-constant magnetic fields. Most notable are the $\nabla B$ and curvature drifts, whose drift velocities for a particle species labelled by $s$ are given by

$$\boldsymbol{v}_{\nabla B} = \frac{m_s c|\boldsymbol{v}_\perp|^2}{2Z_s eB}\frac{\boldsymbol{B}\times\nabla B}{B^2} \quad \text{and} \quad \boldsymbol{v}_{\boldsymbol{\kappa}} = \frac{m_s c v_\parallel^2}{Z_s eB}\frac{\boldsymbol{B}\times\boldsymbol{\kappa}}{B}, \tag{1.9}$$

respectively. In the above expressions, $m_s$ is the mass of the species, $\boldsymbol{v}_\perp$ and $v_\parallel$ are the perpendicular and parallel components of the particle velocity, $Z_s e$ is the charge of the species and $\boldsymbol{\kappa} \equiv \boldsymbol{b}\cdot\nabla\boldsymbol{b}$, where $\boldsymbol{b} \equiv \boldsymbol{B}/B$. Note that the $\nabla B$ and curvature drifts scale with the particle energy, so particles drift faster on average in hotter plasmas than they do in colder plasma. In a tokamak, the equilibrium magnetic field scales as $B \sim 1/R$, so $\nabla B$ and curvature drifts are ubiquitous. In combination with gradients in equilibrium parameters such as temperature, magnetic drifts can drive microscale[3] instabilities in tokamak plasmas. One of the most important microinstabilities is the toroidal ion-temperature-gradient (ITG) instability [13, 14]. A simplified illustration of the feedback loop that underpins this instability is presented in Figure 1.3.

The microinstabilities present in tokamak plasmas drive turbulence which is understood to be the dominant contributor to the radial transport of heat and particles in tokamaks [15–17]. As one might expect for ITG-driven turbulence, increased ion temperature gradients typically lead to increased turbulent radial transport. This means that for steady-state operation at a higher temperature gradient, increased heating power must be provided. This is problematic because the transport is usually ‘stiff’, meaning that above a threshold temperature gradient, the transport increases rapidly with increasing temperature gradient. This is illustrated in Figure 1.4. As a result, a significant increase in auxiliary heating power leads to a relatively small increase in

---

[3] The scales can range from a few ion gyro-radii to a few electron-gyro-radii, depending on the relevant instability.

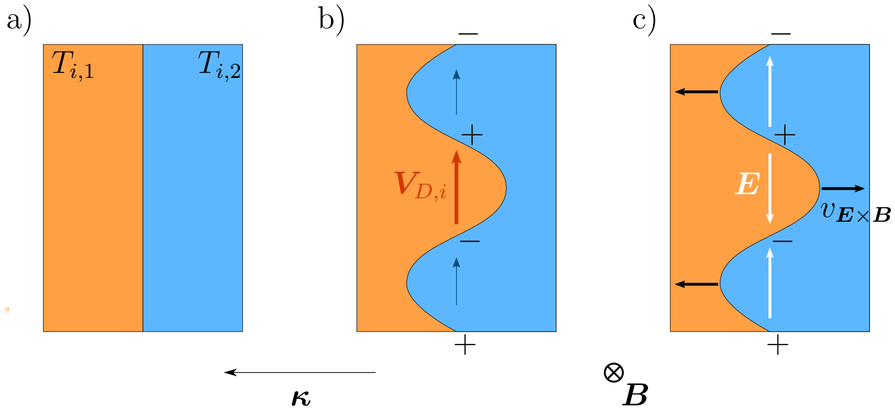

Figure 1.3: A simplified illustration for the mechanism of the toroidal ITG instability at the outboard midplane of a tokamak. In a), a boundary is defined between two regions of plasma with different ion temperatures $T_{i,1}$ and $T_{i,2}$ such that $T_{i,1} > T_{i,2}$. The equilibrium magnetic field $\boldsymbol{B}$ is into the page. In b), the boundary is perturbed. Due to the $\nabla B$ and curvature drifts, ions drift upwards at an average speed $\boldsymbol{V}_{D,i}$ that scales with the equilibrium temperature, creating alternating regions of increased and decreased ion density at the boundaries between hot and cold regions. These are indicated by $+$ and $-$, respectively. In c), the resulting electric field $\boldsymbol{E}$ leads to an $\boldsymbol{E} \times \boldsymbol{B}$ drift that amplifies the initial perturbation. If the curvature is reversed relative to the temperature gradient, as is the case on the inboard side of the tokamak, the perturbation is stabilized. The inboard side is therefore described as the good-curvature region.

fusion power. This stiffness limits energy production, which relies on the fusion power being orders of magnitude larger than the auxiliary heating power. This usually constrains temperature length scales $L_T \equiv \left(\mathrm{d}(\log T)/\mathrm{d}r\right)^{-1}$ to be larger than a few times smaller than the minor radius of the last (outermost) closed flux surface (LCFS). Here $T$ is the temperature and $r$, which is often used as a flux-surface label, is the half-diameter of a given flux surface at the outboard midplane. As a result, only a fraction of the plasma volume typically has conditions suitable for fusion. A significant amount of research effort is spent trying to alleviate this problem of stiff transport, either by shifting the stiffness threshold $L_T$ or by reducing the stiffness.

## 1.3 Gyrokinetic modelling

Understanding the microinstabilities that drive turbulence can help us mitigate their influence. One framework for studying microstabilty and microturbulence is

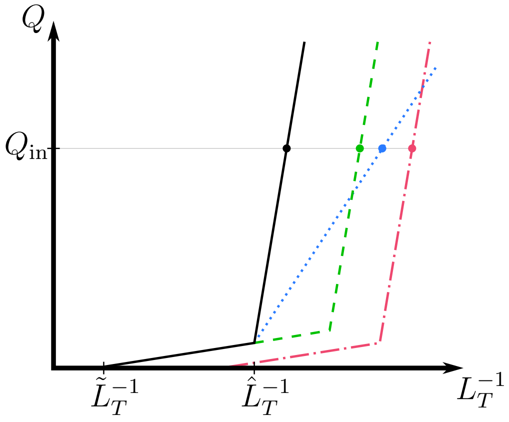

Figure 1.4: A schematic illustration of the radial heat flux $Q$ as a function of inverse temperature scale length $L_T^{-1}$. In steady state, the heat flux is equal to the input power flux $Q_{\text{in}}$. As $L_T^{-1}$ increases beyond the linear instability threshold $\tilde{L}_T^{-1}$, the linear instability begins to drive turbulence. Above a threshold $\hat{L}_T^{-1}$, the radial transport becomes 'stiff', increasing rapidly with $L_T^{-1}$. A large increase in the input heat flux $Q_{\text{in}}$ is then required to increase $L_T^{-1}$ by a small amount. Transport can be reduced in three ways (or a combination of the three), illustrated by the three coloured lines. By changing equilibrium parameters that govern the underlying instabilities, either the transport could become less stiff (shown by the dotted blue line), the threshold for stiffness could shift (shown by the dashed green line), or the threshold for linear instability could shift (shown by the dash-dotted red line). In the intermediate regime where $\tilde{L}_T^{-1} < L_T^{-1} < \hat{L}_T^{-1}$, the turbulence is thought to be damped by zonal flows, which are primarily-poloidal flows that act to break up turbulent structures by shearing them [18–20].

$\delta f$-gyrokinetics, which describes the evolution of microscale, rapidly fluctuating electromagnetic fields and distribution functions. Numerical codes, such as the local $\delta f$ gyrokinetic code `GS2` used throughout this work, can be used to study the evolution of the fluctuating quantities [1, 2]. At small perturbation amplitude the nonlinear terms are negligible (and can be dropped) and local equilibrium parameters including the driving gradients can be varied. This allows us to more easily study the underlying linear microinstabilities that drive the turbulence. Alternatively, simulations can be performed with the nonlinear terms included to make predictions or comparisons against transport levels measured in experiments. This gives us the freedom to isolate physical effects that can be controlled in experiments to improve performance and advise the design of new confinement devices.

### 1.3.1 The $\delta f$-gyrokinetic framework

$\delta f$ gyrokinetics is an expansion of general kinetic theory that can be used to describe the interaction between plasma and electromagnetic fields at spatial scales as small as the Larmor radius and temporal scales much slower than the Larmor frequency. The full 6-dimensional Fokker-Planck equation is

$$\frac{\partial \tilde{f}_s}{\partial t} + \boldsymbol{v} \cdot \nabla \tilde{f}_s + \frac{Z_s e}{m_s}\left(\tilde{\boldsymbol{E}} + \frac{\boldsymbol{v}}{c} \times \tilde{\boldsymbol{B}}\right) \cdot \frac{\partial \tilde{f}_s}{\partial \boldsymbol{v}} = C[\tilde{f}_s] + S_s \tag{1.10}$$

where $\tilde{f}_s$ is the distribution function that describes the 6-d phase-space density of a particle species labelled by $s$, $t$ is the time, $\boldsymbol{v}$ is the velocity, $Z_s$ is the species charge number, $e$ is the elementary unit of charge, $m_s$ is the species mass, $\tilde{\boldsymbol{E}}$ is the total electric field, $\tilde{\boldsymbol{B}}$ is the total magnetic field, $C$ is the collision operator and $S_s$ is a source term that accounts for other physical processes such as external heating. In combination with Maxwell's equations, this forms a closed set of equations that can be solved simultaneously. However, it is not computationally tractable to solve these equations whilst resolving both microscopic and macroscopic behaviour in all 6 dimensions. $\delta f$-gyrokinetics ameliorates this problem by taking advantage of the spatial and temporal scale separations that exist in magnetized plasmas.

To do this, it is assumed that the distribution functions and electromagnetic fields can each be split into a mean and fluctuating piece [21]. For example, the distribution function is expressed as

$$\tilde{f}_s = f_s + \delta f_s, \tag{1.11}$$

and there are similar expressions for $\tilde{\boldsymbol{B}}$ and $\tilde{\boldsymbol{E}}$. The mean quantities vary spatially on macroscopic scales, such as the minor radius of the LCFS $a$, and temporally on the scale of the energy confinement time $\tau_E$. The fluctuating quantities have an anisotropy that reflects how strongly-magnetized particles can stream rapidly along field lines but travel slowly perpendicular to them due to the Lorentz force. As such, fluctuating quantities vary spatially on scales of the Larmor radius $\rho_s$ perpendicular to the magnetic field but macroscopic scales parallel to it. In a Fourier representation of the fluctuating quantities, this could be expressed mathematically using the parallel and perpendicular wavenumbers via $k_\parallel \ll |\boldsymbol{k}_\perp|$. The turbulent fluctuations are assumed to evolve on a timescale $\omega^{-1}$, which is intermediate to the short Larmor rotation timescale $\Omega_s^{-1} \ll \omega^{-1}$ and the long mean evolution time $\tau_E \gg \omega^{-1}$. The disparity between the Larmor and macroscopic spatial scales allows for the definition a small parameter $\rho^* \equiv \rho_s/a$ that is used as a formal expansion parameter to order quantities as follows:

$$\rho^* \equiv \frac{\rho_s}{a} \sim \frac{\delta f_s}{f_s} \sim \frac{|\delta \boldsymbol{E}|}{|\boldsymbol{E}|} \sim \frac{|\delta \boldsymbol{B}|}{|\boldsymbol{B}|} \sim \frac{k_\parallel}{|\boldsymbol{k}_\perp|} \sim \frac{\omega}{\Omega_s}. \tag{1.12}$$

These orderings are a natural consequence of scale separation in magnetized plasmas. The spatial scale of turbulent structures can only result in changes to macroscopic quantities on similar spatial scales. These spatially-small changes naturally restrict the fluctuating quantities to be similarly small relative to the macroscopic profiles. By rigorously expanding Equation 1.10 in orders of $\rho^*$ and averaging over the rapid gyromotion, the mean piece of the distribution function is found to be a Maxwellian $f_{0,s}$, and the fluctuating distribution function can be split into adiabatic and non-adiabatic parts according to:

$$\delta f_s = h_s - \underbrace{\frac{Z_s e}{T_s}\left(\delta\phi - \frac{\boldsymbol{u}}{c}\cdot\delta\boldsymbol{A}\right) f_s}_{\text{adiabatic response}}, \tag{1.13}$$

where $\delta\phi$ is the fluctuating electrostatic potential, $\delta\boldsymbol{A}$ is the fluctuating magnetic vector potential, and $\boldsymbol{u}$ is the toroidal mean flow. With the exception of $h_s$, which is evaluated at the guiding-centre position $\boldsymbol{R}_s \equiv \boldsymbol{r} - \Omega_s^{-1}\boldsymbol{b}\times\boldsymbol{w}_\perp$, the fields are evaluated at the particle position $\boldsymbol{r}$. We use $\boldsymbol{w} \equiv \boldsymbol{v} - \boldsymbol{u}$ to denote the peculiar velocity, and $\boldsymbol{w}_\perp$ is the component of $\boldsymbol{w}$ perpendicular to the equilibrium magnetic field. The non-adiabatic piece of the fluctuating distribution function $h_s$ evolves according to the gyrokinetic equation [21]:

$$\begin{aligned} &\frac{dh_s}{dt} + \left(w_\parallel \boldsymbol{b} + \boldsymbol{V}_{D,s} + \langle \boldsymbol{V}_\chi \rangle_{\boldsymbol{R}_s}\right)\cdot\nabla h_s - \langle C[h_s]\rangle_{\boldsymbol{R}_s} = \\ &\qquad \frac{Z_s e f_{0,s}}{T_s}\frac{d\langle\chi\rangle_{\boldsymbol{R}_s}}{dt} - \left\{\frac{\partial f_{0,s}}{\partial\tilde{\psi}} + \frac{m_s f_{0,s}}{T_s}\left[\frac{I w_\parallel}{B} + \omega_\psi R^2\right]\frac{\partial\omega_\psi}{\partial\tilde{\psi}}\right\}\langle \boldsymbol{V}_\chi\rangle_{\boldsymbol{R}_s}\cdot\nabla\tilde{\psi}. \end{aligned} \tag{1.14}$$

Here, $d/dt \equiv \partial/\partial t + \boldsymbol{u}\cdot\nabla$ is a convective derivative and the component of peculiar velocity parallel to the equilibrium magnetic field is denoted by $w_\parallel$. The toroidal angular velocity $\omega_\psi$ can be related to $\boldsymbol{u}$ by $\boldsymbol{u} = \omega_\psi R^2 \nabla\zeta$. The first term on the right hand side of Equation 1.14 represents the evolution of the gyrokinetic potential

$$\chi \equiv \delta\phi - \frac{\boldsymbol{v}}{c} \cdot \delta\boldsymbol{A}, \tag{1.15}$$

whereas the other terms in $\partial f_{0,s}/\partial\tilde{\psi}$ and $\partial\omega_\psi/\partial\tilde{\psi}$ can drive turbulence via the temperature and density gradients, and the toroidal velocity gradient, respectively. The equilibrium magnetic drifts, such as the curvature, $\nabla B$, centrifugal, Coriolis and mean first-order $\boldsymbol{E} \times \boldsymbol{B}$ drifts, are contained within $\boldsymbol{V}_{D,s}$, while $\boldsymbol{V}_\chi \equiv cB^{-1}\boldsymbol{b} \times \nabla\chi$ contains the fluctuating $\boldsymbol{E} \times \boldsymbol{B}$ drift, the motion along fluctuating magnetic field lines, and the fluctuating $\nabla B$ drift [21]. Finally, $\langle \ldots \rangle_{\boldsymbol{R}_s}$ represents a gyroaverage at fixed guiding centre. Like with the Fokker-Planck equation, Maxwell's equations can be ordered in a similar way to close the system of equations. They are expressed via the quasineutrality equation and Ampère's law, given below in order:

$$\sum_s \frac{Z_s^2 e^2 n_s}{T_s} \left( \delta\phi - \frac{\boldsymbol{u}}{c} \cdot \delta\boldsymbol{A} \right) = \sum_s Z_s e \int \mathrm{d}^3\boldsymbol{w} \langle h_s \rangle_{\boldsymbol{r}}; \tag{1.16}$$

$$\nabla \times \delta\boldsymbol{B} = \frac{4\pi}{c} \sum_s Z_s e \int \mathrm{d}^3\boldsymbol{w} \langle \boldsymbol{w} h_s \rangle_{\boldsymbol{r}}. \tag{1.17}$$

The species density is denoted by $n_s$ and the gyroaverages in these expressions are performed at fixed particle position $\boldsymbol{r}$ rather than $\boldsymbol{R}_s$.

### 1.3.2 Local gyrokinetic simulations with `GS2`

Although $\delta f$ gyrokinetics already reduces computational expense via scale separation and a reduction in dimensionality, simulating the entire core of a tokamak is still computationally expensive. To reduce this expense, some codes such as `GS2` use a 'local' approach, restricting the simulation domain to a narrow, extended filament that follows a magnetic field line as it wraps around a flux surface. This simulation domain is known as a flux tube, and twists along its axis to take into account magnetic shear [22]. A schematic illustration of this is shown in Figure 1.5, which is adapted from [23]. The perpendicular extent of the flux tube should be larger than the turbulence correlation length. This allows the use of periodic boundary conditions perpendicular to the magnetic field because the turbulence on one side of the domain can then be

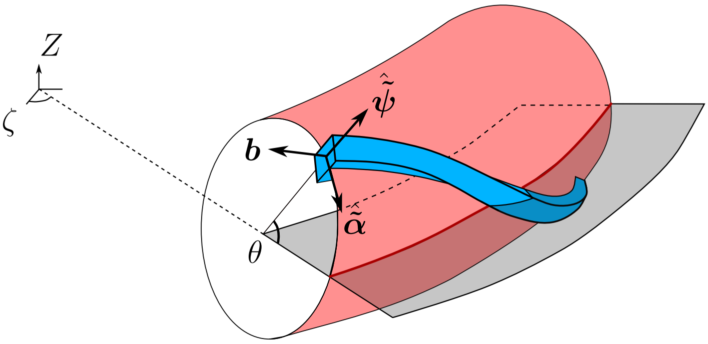

Figure 1.5: A schematic illustration of part of a flux tube (blue) on a flux surface (red). The grey shaded region defines the $\theta = 0$ plane.

assumed to be statistically identical to that on the opposite side. It is assumed that these *statistically* identical regions can be set to be *exactly* identical. In practice, the turbulence correlation length is typically of the order $\rho_i$, so the flux tube is a few ion gyro-radii wide. Equilibrium parameters that depend only on $\tilde{\psi}$, such as $T_s$ and $L_{T_s}^{-1}$, can then be treated as locally-constant throughout the simulation domain. The use of periodic boundary conditions in the plane perpendicular to the magnetic field permits the perpendicular components of the fluctuating fields to be represented spectrally by Fourier components. Recalling the Clebsch representation of the magnetic field in Equation 1.1, a natural pair of perpendicular coordinates are $\tilde{\psi}$ and $\tilde{\alpha}$, which label a flux surface and field line, respectively. This leaves us to choose a coordinate that determines the distance along a given field line – we choose the poloidal angle $\theta$. A fluctuating quantity $D$ can therefore be written as

$$D(t, \tilde{\psi}, \tilde{\alpha}, \theta) = \sum_{k_{\tilde{\psi}}} \sum_{k_{\tilde{\alpha}}} \hat{D}_{k_{\tilde{\psi}}, k_{\tilde{\alpha}}}(t, \theta) \mathrm{e}^{ik_{\tilde{\psi}}(\tilde{\psi}-\tilde{\psi}_0)} \mathrm{e}^{ik_{\tilde{\alpha}}(\tilde{\alpha}-\tilde{\alpha}_0)}, \tag{1.18}$$

where a subscript zero here indicates the value at the centre of the flux tube. The parallel domain extends along a field line for a complete poloidal turn. Such a length is typically known as the connection length and is approximately $2\pi q R_0$.

Rather than a periodic boundary condition in the parallel direction, `GS2` uses the ‘twist-and-shift’ boundary condition [22], which enforces that fluctuations perpendicular to a magnetic field line are periodic in $\theta$ whilst holding $\tilde{\psi}$ and $\zeta$ fixed, rather than

$\tilde{\psi}$ and $\tilde{\alpha}$:

$$D\big(t,\tilde{\psi},\tilde{\alpha}(\tilde{\psi},\theta+2\pi,\zeta),\theta+2\pi\big) = D\big(t,\tilde{\psi},\tilde{\alpha}(\tilde{\psi},\theta,\zeta),\theta\big) \tag{1.19}$$

This boundary condition couples the Fourier coefficient at one end of a flux tube to the Fourier coefficient of a mode with the same $k_{\tilde{\alpha}}$ but a different $k_{\tilde{\psi}}$ at the opposite end of its parallel domain. This is a consequence of magnetic shear, which results in the modes with different $k_{\tilde{\psi}}$ having the same radial wavenumber at opposing ends of the flux tube. By coupling many such $2\pi$ segments together according to Equation 1.19, one can construct a 'ballooning chain'. We distinguish ballooning chains by labelling each one with the poloidal angle $\theta_0$ between $-\pi$ and $\pi$ at which the chain has no radial structure – i.e. $\boldsymbol{k}_\perp \cdot \nabla\tilde{\psi} = 0$, where $\boldsymbol{k}_\perp \equiv k_{\tilde{\psi}}\nabla\tilde{\psi} + k_{\tilde{\alpha}}\nabla\tilde{\alpha}$ is the mode's perpendicular wavevector. This is known as the ballooning angle, and the linear growth-rate of a ballooning chain is $2\pi$-periodic in $\theta_0$. If we neglect nonlinear terms, then each ballooning chain evolves independently of the others.

We can now rewrite Equation 1.14 in the flux-tube representation used by `GS2` for Fourier coefficients $\hat{D}$, but dropping the $\hat{}$s and wavenumber labels for brevity:

$$\frac{\partial h_s}{\partial t} + \big[v_\parallel \boldsymbol{b}\cdot\nabla + i\boldsymbol{k}_\perp\cdot\boldsymbol{V}_{D,s}\big]h_s = \frac{Z_s e f_{0,s}}{T_s}\frac{\partial\langle\chi\rangle_{\boldsymbol{R}_s}}{\partial t} - \langle\boldsymbol{V}_\chi\rangle_{\boldsymbol{R}_s}\cdot\nabla\tilde{\psi}\,\frac{\partial f_{0,s}}{\partial\tilde{\psi}}. \tag{1.20}$$

To draw attention to the basic linear physics, we have omitted the nonlinear term $\langle\boldsymbol{V}_\chi\rangle_{\boldsymbol{R}_s}\cdot\nabla h_s$, and ignored collisions. We also set $\boldsymbol{u}=0$ and neglected flow shear, i.e. $\frac{\partial\omega_\psi}{\partial\tilde{\psi}} = 0$. For details of the implementation including flow shear in `GS2`, see [24][4]. The spectral representation perpendicular to the magnetic field allows us to easily evaluate the gyroaverage so that

$$\langle\chi\rangle_{\boldsymbol{R}_s} = J_0(\alpha_s)\bigg(\delta\phi - \frac{v_\parallel}{c}\delta A_\parallel\bigg) + \frac{J_1(\alpha_s)}{\alpha_s}\frac{m_s|\boldsymbol{v}_\perp|^2}{Z_s e}\frac{\delta B_\parallel}{B}, \tag{1.21}$$

where $J_n(\dots)$ are the $n$th order Bessel functions of the first kind, $\alpha_s \equiv |\boldsymbol{k}_\perp||\boldsymbol{v}_\perp|/\Omega_s$ and $\boldsymbol{v}_\perp$ is the perpendicular component of the velocity. These Bessel functions are the mathematical manifestation of the gyroaverage, which allows us to cast the $\boldsymbol{v}_\perp\cdot\delta\boldsymbol{A}_\perp$ contribution in terms of the single scalar field $\delta B_\parallel$. To close the system of equations,

---

[4] Notably, `GS2`'s treatment of flow shear does *not* include the centrifugal drift or the centrifugal drive term (the second term multiplying $\frac{\partial\omega_\psi}{\partial\tilde{\psi}}$ in Equation 1.14)

we require expressions for the three scalar fields $\delta\phi$, $\delta A_{\|}$ and $\delta B_{\|}$. For $\delta\phi$, we rewrite Equation 1.16 as follows:

$$0 = \sum_s Z_s e \int d^3\boldsymbol{v}\left(h_s J_0(\alpha_s) - \frac{Z_s e\delta\phi}{T_s} f_{0,s}\right); \tag{1.22}$$

For the magnetic scalar fields, we can use Ampère's law. The expression for the parallel magnetic potential can be derived by expanding the left hand side of Equation 1.17 using $\delta\boldsymbol{B} = \nabla \times \delta\boldsymbol{A}$, and taking the scalar product of both sides with $\boldsymbol{b}$:

$$|\boldsymbol{k}_\perp|^2 \delta A_{\|} = \frac{4\pi}{c} \sum_s Z_s e \int d^3\boldsymbol{v}\, v_{\|} h_s J_0(\alpha_s); \tag{1.23}$$

The expression for $\delta B_{\|}$ can be derived in a similar way by taking the curl of Equation 1.17, followed by the scalar product of both sides with $\boldsymbol{b}$:

$$|\boldsymbol{k}_\perp| \delta B_{\|} = -\frac{4\pi}{c} \sum_s Z_s e \int \mathrm{d}^3\boldsymbol{v} |\boldsymbol{v}_\perp| h_s J_1(\alpha_s), \tag{1.24}$$

### 1.3.3 Normalizations

Before continuing, we note that the flux-tube coordinates $\tilde{\psi}$ and $\tilde{\alpha}$ are recast in `GS2` as $x$ and $y$:

$$x \equiv \frac{q_0}{r_0 B_0}(\tilde{\psi} - \tilde{\psi}_0); \tag{1.25}$$

$$y \equiv \frac{\tilde{\psi}_0'}{B_0}(\tilde{\alpha} - \tilde{\alpha}_0), \tag{1.26}$$

where $B_0$ is the reference magnetic field, chosen here to be the toroidal magnetic field on the magnetic axis where $r = 0$. The perpendicular wavevector is then defined in terms of these coordinates such that $\boldsymbol{k}_\perp = k_x \nabla x + k_y \nabla y$. The wavenumbers $k_x$ and $k_y$ can be related to $k_{\tilde{\psi}}$ and $k_{\tilde{\alpha}}$ by using the above expressions for $x$ and $y$. All variables are subsequently normalized by appropriate quantities such that they are dimensionless. Perpendicular turbulent length scales are normalized by the main-ion thermal gyro-radius, while equilibrium length scales are normalized by $a$. All time-scales are normalized by $a/v_{\mathrm{th,ref}}$, where $v_{\mathrm{th,ref}}$ is the thermal velocity of the main ion species. Densities are normalized to the electron density at the magnetic axis, temperatures are normalized to the ion temperature at the magnetic axis, masses are normalized by the main-ion species mass and magnetic fields are normalized by $B_0$. Fluxes are normalized by the gyro-Bohm quantities, which can be derived via a random walk argument and are defined in Appendix B. Throughout the remainder of this Thesis, we will not include the various normalization factors, unless explicitly stated (i.e. $k_y\rho_i \to k_y$). For reference, a complete list of the normalizations used is given in Appendix B. If a quantity is not defined in this Appendix then it is already dimensionless in its given form.

## 1.4 Stabilization Mechanisms

Not every tokamak plasma is made equal. There are a multitude of parameters that determine transport levels; these include the flux-surface shape, field-line pitch angles and much more. In this way, we can think of there being some $N$-dimensional parameter space, where each dimension corresponds to a different parameter. Any given equilibrium corresponds to a single point in this parameter space. The explorable parameter space can be constrained to some extent by ensuring that it is self-consistent, for example, via the Grad-Shafranov equation [10, 11]. One goal of much microstability analysis is to find an equilibrium in this parameter space that minimizes the turbulent transport for fixed driving gradients of temperature and density. This is not a trivial task, as the dimensionality $N$ of the parameter space is very large. Instead of using brute-force to solve this problem by simulating an extraordinary number of equilibria, we often explore how physically-motivated stabilization mechanisms may be affected by changing each of these parameters. Throughout this Thesis we will explore the influence of three particular stabilization mechanisms: magnetic shear, equilibrium flow shear and electromagnetic effects. We proceed to explain how these mechanisms affect stability.

### 1.4.1 Magnetic shear

In a tokamak, the safety factor varies as a function of flux-surface label. This radial variation is characterized by the magnetic shear:

$$\hat{s}(r) \equiv \frac{r}{q(r)}\frac{dq(r)}{dr}. \tag{1.27}$$

We can also define a *local* magnetic shear using the derivative of the local safety factor:

$$\tilde{s}(r,\theta) \equiv \frac{r}{\tilde{q}(r,\theta)} \frac{d\tilde{q}(r,\theta)}{dr}, \tag{1.28}$$

where we have explicitly indicated the extra $\theta$-dependence of the local quantities. We note that since both $r$ and $\tilde{\psi}$ label flux surfaces, we can rewrite functions of $\tilde{\psi}$ as functions of $r$, and vice versa. As coherent structures (such as those generated as a result of the microinstabilities present in tokamak plasmas) travel along the field line, they are tied to the magnetic field lines due to Larmor motion of their constituent particles. This means that, for a given distance travelled along the field line, different radial sections (which are tied to different field lines with different pitch angles) move by different amounts in the poloidal (or toroidal) plane. As a result, the structures are sheared to finer scales as they move along the field line. To see this, starting from Equation 1.3 we expand the perpendicular wavenumber by expressing $\nabla\tilde{\alpha}$ in toroidal $\{\tilde{\psi}, \theta, \zeta\}$ coordinates:

$$\nabla\tilde{\alpha} = \nabla\zeta - \tilde{q}\nabla\theta - \nabla\tilde{\psi} \int_0^\theta \mathrm{d}\theta' \frac{\partial \tilde{q}(\tilde{\psi},\theta')}{\partial\tilde{\psi}}. \tag{1.29}$$

The radial component of perpendicular wavenumber gains a contribution as it moves along the field line, of the form:

$$\boldsymbol{k}_\perp \cdot \nabla\tilde{\psi} = |\nabla\tilde{\psi}|^2 \left( k_{\tilde{\psi}} - k_{\tilde{\alpha}} \left[ \tilde{q} \frac{\nabla\tilde{\psi}\cdot\nabla\theta}{|\nabla\tilde{\psi}|} + \int_0^\theta \mathrm{d}\theta' \frac{\partial\tilde{q}(\tilde{\psi},\theta')}{\partial\tilde{\psi}} \right] \right). \tag{1.30}$$

This expression above indicates that the radial component of $\boldsymbol{k}_\perp$ changes along the field line due to the poloidally-integrated effect of the local magnetic shear. Irrespective of the sign of the magnetic shear, $|\boldsymbol{k}_\perp|$ tends to increase along a field line. This leads to increased stabilization along the field line due to finite-Larmor-radius (FLR) effects, which can be seen from the appearance of $|\boldsymbol{k}_\perp|$ in the argument of the various Bessel functions which appear in Equations 1.21 to 1.24. These Bessel functions, which are the mathematical manifestation of the gyroaverage, have an envelope that decreases as their argument increases. In this regard, increasing the modulus of the magnetic shear is beneficial for reducing transport. For the remainder of this Thesis, we refer to this as the FLR-damping effect.

A second stabilizing effect of magnetic shear is particularly relevant for ballooning-type instabilities whose virulence depends on the spatial alignment of fluctuations with the magnetic drifts that drive them [25, 26]. As shown in Figure 1.3, curvature driven modes such as ITG rely on magnetic drifts to couple the equilibrium gradients to temperature perturbations. The term in Equation 1.20 that does this is $\boldsymbol{k}_\perp \cdot \boldsymbol{V}_{D,s} h_s$. This means that the magnetic drift tends to couple to the fluctuations more strongly when they are spatially oriented such that their perpendicular wavevector aligns with the drift direction. In a conventional tokamak, the magnetic drifts are predominantly vertical – this is a result of the magnetic field being primarily toroidal, and the magnetic curvature and $\nabla B$ vectors pointing mainly along $\nabla R$. We focus first on modes that grow at the outboard midplane, where the magnetic drifts are tangential to the flux surface, i.e. $\boldsymbol{V}_{D,s} \cdot \nabla\tilde{\psi} = 0$. Any component of $\boldsymbol{k}_\perp$ that is not parallel to $\boldsymbol{V}_{D,s}$ will not contribute to the drive term, but can still result in FLR damping. The most strongly-driven mode for a given $k_{\tilde{\alpha}}$ is the therefore the one with $k_{\tilde{\psi}} = 0$. Further along the field line at a different poloidal location, the mode's wavenumber can gain a $\nabla\tilde{\psi}$ component, depending on the magnetic shear. At this different poloidal location, the magnetic drifts will typically have a $\nabla\tilde{\psi}$ component. Depending on the sign and magnitude of the magnetic shear, fluctuations can gain a $\nabla\tilde{\psi}$ component that either strengthens or weakens the drive term. As illustrated and explained in Figure 1.6, negative (or very large) $\tilde{s}$ tends to weaken the drive, whereas moderate ($\sim 1$) positive $\tilde{s}$ strengthens it [25]. We refer to this as the drive-damping effect of magnetic shear for the remainder of this Thesis.

### 1.4.2 Equilibrium flow shear

Part of the heating (and fuelling) in tokamak plasmas is often provided by neutral beam injection (NBI), whereby a net-neutral stream of plasma is accelerated to high energies before being forced to recombine and directed into the tokamak plasma [27]. As this energetic beam interacts with the core plasma, it exerts a torque on the plasma, giving it a toroidal component of angular velocity [28]. The torque is applied across a specific region in the plasma rather than uniformly across its volume, generating gradients in the mean toroidal flow. The radial gradient can be decomposed into two parts – parallel

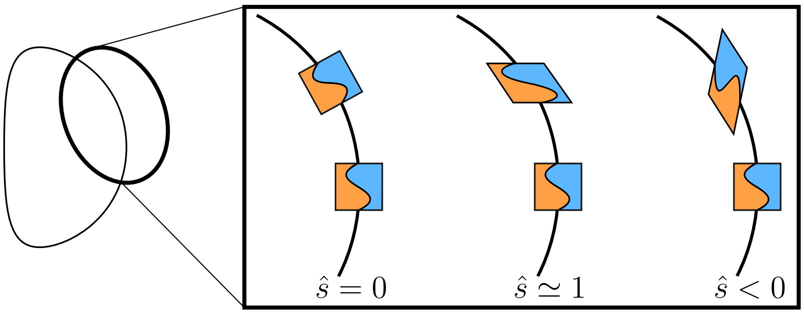

Figure 1.6: The drive-damping effect of magnetic shear on a ballooning-type instability, represented by a perturbation in the surface separating two regions of different temperature – blue is colder than orange. An instability is driven strongly at the outboard midplane where $\boldsymbol{V}_{D,s} \cdot \boldsymbol{k}_\perp$ is maximal. The perturbations are advected along the field lines to a different poloidal (and toroidal) position. With moderate positive magnetic shear, the outboard side lags behind the inboard side poloidally, so the perturbation retains some major-radial extent and remains strongly driven. For negative magnetic shear, the inboard side lags and the perturbation gains more vertical extent, and thus couples more weakly to the predominantly vertical magnetic drifts.

and perpendicular to the magnetic field. The gradient in the parallel component of the velocity gradient (PVG) tends to destabilize microinstabilities present in tokamak plasmas [29–31]. The radial gradient in the component of the velocity perpendicular to the magnetic field, often known as the background $\boldsymbol{E} \times \boldsymbol{B}$ shear, is defined as:

$$\gamma_{E\times B} \equiv -\frac{r}{q}\frac{d\omega_\psi}{dr}. \tag{1.31}$$

The presence of significant $\boldsymbol{E} \times \boldsymbol{B}$ shear typically leads to a reduction in radial transport both experimentally and numerically [18, 32–35]. Drift-wave microinstabilities such as ITG are linearly stabilized by perpendicular flow shear [36, 30]. This can be understood in a similar context to the FLR- and drive-damping effects described in the previous Section. The sheared flow perpendicular to the field line applies a time-dependent shearing effect on fluctuations. In `GS2` coordinates, this means that the radial wavenumber acquires a time-dependence, such that

$$k_x^* = k_x + k_y \gamma_{E\times B} t, \tag{1.32}$$

where the asterisk denotes a time-dependent quantity. Correspondingly, the ballooning angle, defined in `GS2` coordinates as

$$\theta_0 \equiv \frac{k_x}{\hat{s} k_y}, \tag{1.33}$$

gains a similar time dependence:

$$\theta_0^* \equiv \frac{k_x^*}{\hat{s} k_y} = \theta_0 + \frac{\gamma_{E\times B} t}{\hat{s}}. \tag{1.34}$$

Keep in mind that a mode's growth rate is $2\pi$-periodic in $\theta_0$ (and $\theta_0^*$). Typically, modes with $\theta_0 = 0$ are more strongly driven than those with finite $\theta_0$ due to the FLR-damping effects discussed in the previous Section. As a result, fluctuating quantities evolve in an oscillatory fashion, with a period $T_f$ known as the Floquet period:

$$T_f = \left| \frac{2\pi \hat{s}}{\gamma_{E\times B}} \right|. \tag{1.35}$$

When determining growth rates of linear instabilities in the presence of $\boldsymbol{E} \times \boldsymbol{B}$ shear, two types of growth rates can be measured. One option is to track the maximum amplitude of the potential along a field line in time over many Floquet periods. The growth rate is then the time average of this maximum potential over several Floquet oscillations to get a time-averaged growth rate. We note that this leads to discontinuous behaviour in the growth rate when comparing values at a single $\theta_0$ without flow shear to those with infinitesimally small flow-shear. This is because Floquet oscillations allow the mode to sample all of the $\theta_0$ values over a single Floquet period $T_f$ so the time average, as long as it is taken over at least a full Floquet oscillation, will be affected by the increased stability of the modes at finite $\theta_0$. The other choice is to pick maximum instantaneous growth rate during the course of several Floquet oscillations. In contrast to the average growth-rate, this measurement will tend to exceed the linear growth rate without flow shear. This is because the linear growth rates at a given $\theta_0$ tend to increase with the inclusion of PVG.

### 1.4.3 Electromagnetic effects

In high-performance plasmas, the thermal pressure should be sufficiently high for nuclear fusion to take place. In tokamak plasmas, the ratio of the thermal and magnetic pressures is known as the plasma $\beta$ parameter. $\beta$ is an important quantity in the context of microstability as it defines the importance of microscale field-line bending and compression effects. To see this, we note that instabilities such as ITG can generate flows perpendicular to the equilibrium magnetic field. If the magnetic field is 'frozen-in' to the plasma, these flows will deform the magnetic field [37]. The length scale associated with flux-freezing is the electron skin depth $d_e \equiv c/\omega_{p,e}$, where $c$ is the speed of light in a vacuum and $\omega_{p,e}$ is the electron plasma frequency. For the magnetic field to be frozen-in, the electron skin depth must be smaller than the typical length scale of the instability. For the ion-scale instabilities that tend to be the main contributors to the turbulent drive, the relevant length scale is the ion Larmor radius $\rho_i$. The ratio $d_e/\rho_i$ scales like $1/\sqrt{\beta}$, so for magnetic field lines to be deformed by ion-scale instabilities $\sqrt{\beta}$ must begin to approach $\rho_e/\rho_i$, where $\rho_e$ is the electron Larmor radius. Once the field lines are allowed to respond to these instability-driven flows, effects associated with the field-line compression and bending can become manifest.

The stability of large-scale MHD modes is known to have a $\beta$ threshold that depends on the plasma parameters [38]. The microinstabilities that exist in tokamak plasmas are also affected by electromagnetic (EM) effects. It has been shown numerically and analytically that the ITG instability is linearly stabilized by the inclusion of perpendicular magnetic fluctuations in both sheared slab and toroidal geometries at finite $\beta$ [39–45]. Nonlinear simulations have also demonstrated that EM effects reduce the radial heat transport more than would be expected due to the EM reduction in linear drive [44, 46, 45]. This nonlinear enhancement in confinement is attributed to an increased coupling to zonal flows when EM effects are included [47]. The physical mechanism for the stabilization of ITG is not generally discussed in the literature in detail. However, it is clear that field-line-bending fluctuations, rather than compressional ones, provide the stabilizing influence. One can therefore form a simple explanation for the stabilization mechanism whereby the magnetic tension generated in deformed field lines acts to damp the flows that deform them. As well as stabilizing ITG, EM effects are required to destabilize other modes such as kinetic ballooning modes (KBMs) via a coupling with shear- and compressional Alfvén waves [48–50, 44]. The KBM is a ballooning-type instability that is a kinetic analogue of the MHD ballooning instability typically thought to provide a $\beta$ limit. There are different types of KBM that rely on the coupling of shear or compressional Alfvén waves to the usual ITG instability [51–53]. The critical $\beta$ for the onset of KBM instability is often less than the ideal MHD limiting $\beta$ [49, 50]. The KBM linear stability $\beta$-dependence is typically non-monotonic because $\beta$ appears in the underlying equations in a variety of ways. There is the intrinsic effect described in the previous paragraph that influences how strongly magnetic fields respond to the flows, but also an equilibrium effect due to the appearance of the radial derivative of $\beta$ in the Grad-Shafranov equation. This equilibrium effect typically acts to provide stability via local magnetic shear as $\beta$ is increased, as will be discussed in Chapter 2 in more detail. Linear growth rates for KBMs typically increase with $\beta$ at first, before being partially stabilized by the equilibrium effect in a phenomenon known as second stability [54–57].

## 1.5 Goals/Outline

In this Thesis, we will explore the microstability (and the resulting microturbulence) of high-performance tokamak core plasmas which contain steep gradients in temperature and pressure. We now give a brief summary of the contents and key contributions of each chapter. In Chapter 2, we compare the effects of plasma flux-surface shaping on microstability between a low- and high-$\beta$ equilibrium. We explain how the flux surface affects microstability via its effect on local magnetic shear. We find the novel result that increased elongation can further destabilize the linear ITG instability, and use nonlinear simulations to show the same trend in the turbulent transport. We explain this effect as a competition between opposing effects of the drive- and FLR-damping discussed in Section 1.4.1. The novel effect with elongation is still present when fully-electromagnetic fluctuations are considered, and has the potential to degrade the region of second stability which, if accessible in experiments, may have profound implications for stability in high-performance tokamaks. In Chapter 3, we focus on the study of a JET discharge that exhibits a strong ITB in the ion temperature. We match multiple transport channels to experimental levels using nonlinear simulations to determine that local $\delta f$ gyrokinetics can describe the formation of this ITB. In doing so, we establish that electromagnetic effects and negative magnetic shear are crucial for providing stabilization at the radial part of the barrier with the most extreme value of $L_T^{-1}$. Shear in the toroidal equilibrium flow was not a key stabilization mechanism at this radial location. In studying the linear stability of several experimentally relevant equilibria, we show that slab ITG competes with, and modifies, the toroidal ITG usually present at ion gyro-radius scales. We also study the radial location outside the foot of the barrier and are able to match experimental fluxes there. We observed that purely-perpendicular flow shear has the potential to decrease linear stability and increase transport, and discuss briefly how this may arise, via transient effects. In Chapter 4, we provide the main conclusions of this work.

# Chapter 2

# Effect of flux-surface shaping on turbulent transport

*The contents of this Chapter is based on Reference [58].*

In Section 1.2.2, we explained how one of the performance-limiting factors on tokamak experiments is the significant turbulence-dominated radial transport of heat, momentum and particles from the core plasma out to the edge. It is well-known that this turbulent transport can be affected by changing the shape of the poloidal cross section of the axisymmetric flux-surfaces traced out by the confining magnetic field. This has been validated both experimentally and via numerical simulations [59–66]. The flux-surface shape is often characterized by parameters such as elongation $\kappa$ and triangularity $\delta$. It can be specified at the edge of the plasma by tuning currents carried by external electromagnetic coils, but changes moving radially inwards to satisfy the Grad-Shafranov equation. In particular, the elongation penetrates deep into the plasma, while triangularity does not [67]. For flux-surfaces with symmetry about the midplane, known as up-down symmetry, we can define these shaping parameters with $\kappa(r) \equiv Z(r, \theta_{\max})/r$ and $\delta(r) \equiv [R_0(r) - R(r, \theta_{\max})]/r$, where $R(r, \theta)$ is the plasma major radius, $\theta$ is the poloidal angle, $Z(r, \theta)$ is the vertical distance above the midplane, $r \equiv [R(r, 0) - R(r, \pi)]/2$ is the plasma half-diameter at the flux-surface midplane, $R_0(r) \equiv [R(r, 0) + R(r, \pi)]/2$ is the major radius of the flux-surface center and $\theta_{\max}$ is the poloidal angle of the maximum $Z$. A labelled example flux-surface shape is shown in Figure 2.1. Plasma shaping is known to affect the stability of the large-scale MHD modes mentioned in Section 1.2. Specifically, increased elongation and triangularity

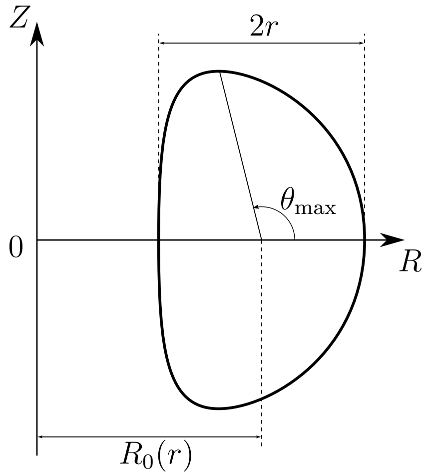

Figure 2.1: A typical flux-surface shape, with $r$, $R_0$ and $\theta_{\max}$ labelled. We define the midplane as the horizontal plane that intersects the widest point of the flux-surface; $\theta = 0$ coincides with the midplane on the outboard side.

increase the threshold "Troyon" plasma $\beta$ above which dangerous (e.g. external kink-ballooning) MHD instabilities are triggered: $\beta_{Troyon} = \beta_N I_p/(aB_0)$, where $\beta$ is the ratio of thermal to magnetic pressure, $\beta_N \simeq 2\%$ is an empirically calculated scaling factor, $a$ is the minor radius of the last (outermost) closed flux surface (LCFS) and $B_0$ is the reference magnetic field, defined as the on-axis toroidal field [68]. The Troyon beta limit increases linearly with plasma current $I_p$ which, for fixed safety factor $q$, is increased by elongation and triangularity. Shaping can however have other important consequences, particularly for vertical displacement events (VDEs) which are associated with disruptions. Whilst increased elongation can ameliorate the aforementioned MHD instabilities, more severe controls for VDEs are then required. This necessitates the careful investigation of shaping effects from both MHD/disruption and transport perspectives.

The impact of shaping on transport due to microinstabilities has been less-thoroughly studied, and those studies that have been performed have focused only on a relatively small region of the vast multi-dimensional shaping parameter space. Despite this, increased elongation is generally thought to be stabilizing [59–62], whereas triangularity can have varying effects. Both the TCV and DIII-D experiments have reported that negative triangularity yields improved performance, allowing performance comparable to discharges that feature an ETB, but without an ETB [63–65]. Reference [60] reports that the effect of triangularity depends on the elongation. At low to moderate $\kappa$, increased triangularity was destabilizing, whilst at high $\kappa$, increased triangularity was stabilizing. There are various hypotheses for these observed effects on the turbulence. Some suggest that the flux-surface shaping affects the density of flux-surfaces as a function of $\theta$, thereby locally (in $\theta$) modifying the driving gradients [63]. Others believe that the effects of shaping on microstability can be explained by its effect on the local magnetic shear $\tilde{s}$.

As discussed in Section 1.4.1, local magnetic shear has an impact on stability via drive-damping and FLR-damping effects, via its influence on $\boldsymbol{k}_\perp$. To connect quantities like $\tilde{s}$ (and thus $\boldsymbol{k}_\perp$) to the flux-surface shape, one can specify analytical expressions for $R(r,\theta)$ and $Z(r,\theta)$. A typical parametrization which often well-approximates experimental flux-surface shapes, and the one used by `GS2`, is the Miller parametrization [69] which uses nine parameters to specify the poloidal cross section. The flux-surface cross-section is parametrized as follows:

$$R(r,\theta) = R_0(r) + r\cos\left[\theta + (\arcsin\delta(r))\sin\theta\right]; \tag{2.1}$$

$$Z(r,\theta) = \kappa(r) r \sin\theta. \tag{2.2}$$

The flux-surface shape can be parametrized by the inverse aspect ratio $\epsilon \equiv r/R_0$, the elongation and the triangularity. In order to calculate the poloidal magnetic field, we must also specify the safety factor as well as the radial gradients of $R_0$, elongation and triangularity. Finally, to ensure that the Grad-Shafranov equation is locally satisfied, we must specify $\hat{s}$ and $\beta' \equiv \beta(\log p)'$ [69]. Note that while one can change any of the nine Miller parameters at will to explore its effect on microstability, the equilibrium is not guaranteed to represent a realistic equilibrium that globally satisfies the Grad-Shafranov equation throughout the plasma. In a real experiment, it is not typically feasible to change just one parameter in isolation. In Appendix A.1, we present a detailed exposition on how to obtain expressions for $\tilde{s}$ and $|\boldsymbol{k}_\perp|^2$ using a Miller parametrization. In Appendix A.2, we guide the reader through the calculation of $\tilde{s}$ and $|\boldsymbol{k}_\perp|$ with the inclusion of $\kappa$ in the limit of small inverse aspect ratio.

In the remainder of this Chapter, we present qualitative differences in microstability between low- and high-performance tokamak plasmas when shaping effects are considered. In Section 2.1 we will introduce two equilibria whose primary difference is in the value of plasma $\beta$. Using these equilibria, we present a simple benchmark of `GS2` and `GKV`, which are two local, flux-tube $\delta f$ gyrokinetic codes [1, 70, 71]. We then extend these simulations to include additional effects of kinetic electrons and magnetic fluctuations, commenting on the spectra of instabilities present. In Section 2.2, we present electrostatic linear and nonlinear scans in elongation and triangularity, uncovering a novel result that at low triangularity, elongation can be destabilizing in the presence of steep pressure gradients. We explore this phenomenon further in Section 2.3, where we present linear simulation results including the effects of magnetic fluctuations. We comment on how the different instabilities present in electromagnetic simulations respond to changes in shaping parameters and show that in steep-pressure-gradient regions with access to KBM-second-stability, increased elongation can severely degrade stability. Finally, Section 2.4 summarizes the work presented in this Chapter.

## 2.1 Equilibria and microstability properties

For the remainder of this Chapter, we focus on results of local flux-tube gyrokinetic simulations. We study in detail two particular equilibria previously studied in Reference [72] that are relevant to the JT-60SA tokamak which is currently being commissioned in Japan. The equilibria are not calculated from experiment but modelled; more details on their origin can be found in Reference [72]. The primary difference between them is in their value of plasma beta, so they will be referred to as low (1.5%[1]) and high (3.7%) $\beta$ – this is the plasma $\beta$ on the magnetic axis. The equilibrium data were supplied in the standard GEQDSK format, but flux-surface shapes were approximated from this data using the Miller parametrization [73]. We focus on three flux-surfaces, labelled using $\rho$, the square root of the toroidal magnetic flux normalized to its value at the LCFS. The extracted flux-surface shapes and equilibrium parameters are given in

---

[1] We note that $\beta = 1.5\%$ is not an insignificant value, and one should expect fully-electromagnetic simulations to give qualitatively different results for both equilibria. We use 'low' to emphasize that $\beta$ is small *relative* to the high-$\beta$ case.

Figure 2.2 and Table 2.1. As mentioned, the key difference between the two equilibria

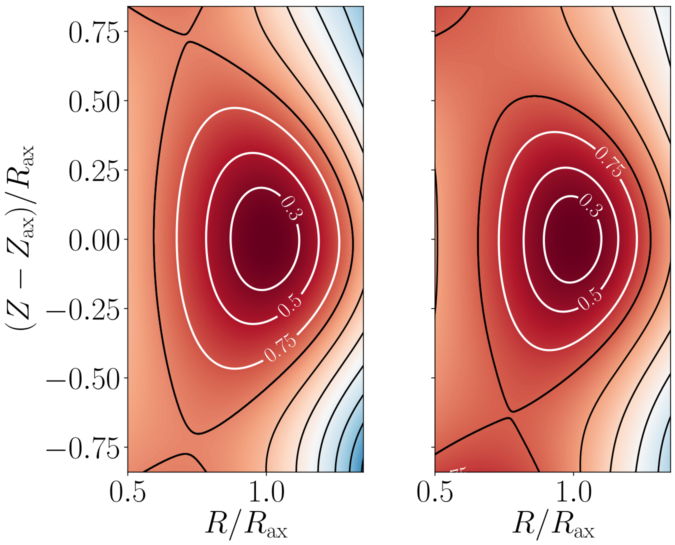

Figure 2.2: Surfaces of constant magnetic flux for the a) low- and b) high-$\beta$ equilibria. White contours, labelled by their values of $\rho$, denote surfaces used in the simulations.

is in the value of $\beta$. This difference in $\beta$ is expected to affect microstability not only in the ways discussed in Section 1.4.3, but also via its effect on $\alpha_{\text{MHD}} \equiv -\beta(\log p)'q^2R_0$, which affects the local magnetic shear as demonstrated in Equation A.23. The flux-surface shaping in the high-$\beta$ equilibrium is more extreme at the edge of the plasma, but converges towards the low-$\beta$ shape as $\rho$ decreases. This reflects the fact that shaping, aside from elongation, does not penetrate deep into the core [67]. Both $\hat{s}$ and the driving gradients are slightly larger in the high-$\beta$ case. As this work is an extension to the work of Nakata et al. in Reference [72], which uses a local flux-tube gyrokinetic code `GKV`, we first present a benchmark of `GS2` and `GKV` with these two equilibria. The benchmark was performed with only electrostatic fluctuations ($\delta A_\parallel = \delta B_\parallel = 0$) and adiabatic electrons with a single ion species ($h_e = 0$). Collisions were not included in any simulations in this Chapter. In Figure 2.3 we show growth-rate and real-frequency spectra for this benchmark. The two codes use different normalizations as detailed in Appendix B.1, so the results from `GS2` were re-normalized for direct comparison with `GKV`.

Table 2.1: Equilibrium parameters for the two equilibria. $R_0'$ is the radial derivative of the Shafranov shift, $\alpha_{\mathrm{MHD}} \equiv -\beta(\log p)' q^2 R_0$, and $T_e = T_i$ for both equilibria.

| | Low-$\beta$ | | | High-$\beta$ | | |
|---|---|---|---|---|---|---|
| $\rho$ | 0.3 | 0.5 | 0.75 | 0.3 | 0.5 | 0.75 |
| $\epsilon$ | 0.10 | 0.17 | 0.25 | 0.12 | 0.21 | 0.30 |
| $q$ | 1.85 | 2.02 | 2.66 | 1.37 | 1.55 | 2.23 |
| $\hat{s}$ | 0.09 | 0.34 | 1.44 | 0.12 | 0.48 | 1.96 |
| $\alpha_{\mathrm{MHD}}$ | 0.48 | 0.83 | 1.19 | 0.62 | 1.13 | 1.66 |
| $-R_0'$ | 0.07 | 0.11 | 0.17 | 0.08 | 0.14 | 0.21 |
| $\kappa$ | 1.50 | 1.52 | 1.58 | 1.49 | 1.52 | 1.61 |
| $\kappa'$ | 0.04 | 0.10 | 0.33 | 0.05 | 0.14 | 0.47 |
| $\delta$ | 0.08 | 0.14 | 0.23 | 0.10 | 0.17 | 0.29 |
| $\delta'$ | 0.26 | 0.29 | 0.48 | 0.31 | 0.36 | 0.66 |
| $(\log T_s)'$ | 2.33 | 2.42 | 2.72 | 2.69 | 2.84 | 3.33 |
| $(\log n_s)'$ | 0.78 | 0.81 | 0.91 | 0.90 | 0.95 | 1.11 |
| $\beta$ (%) | 0.69 | 0.41 | 0.22 | 1.74 | 1.05 | 0.56 |

At all scales simulated, the toroidal ITG is the dominant instability. The benchmark shows good agreement between the two codes in both the growth-rate and real-frequency spectra. The small mismatch in growth rates and real frequencies between `GS2` and `GKV` was not eliminated with increasing resolution or by using the numerical equilibrium as a direct input. However, we note that a similar discrepancy was previously observed in a benchmark between the two codes; this was understood to be due to algorithmic differences between the two codes that affect the numerical dissipation [74]. We extended the study of these equilibria to include additional effects. Linear growth-rate and real-frequency spectra comparing the extensions to the original `GS2` results are shown in Figure 2.4. The addition of electrons as a kinetic species (i.e. $h_e \neq 0$) approximately doubles growth rates at all $k_y$ and $\rho$. For both equilibria, the $\rho = 0.3$ and 0.5 radii show that the dominant mode changes for $k_y \gtrsim 1.2$. In general, a change in dominant mode is indicated by a discontinuous change in the real-frequency spectrum. The mode structure parallel to the field line often shows clear differences

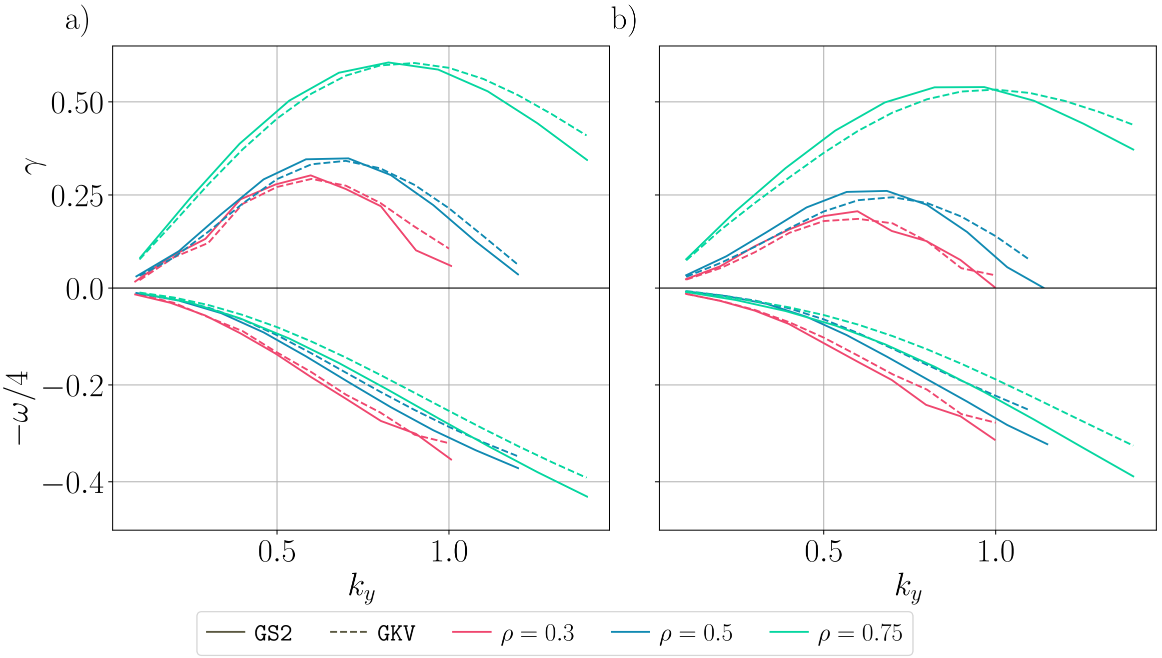

Figure 2.3: Benchmark results showing normalized real-frequency $\omega$ and growth-rate $\gamma$ spectra at three different radial positions for the a) low-$\beta$ and b) high-$\beta$ equilibria. The `GS2` variables have been renormalized to their `GKV` equivalents according to Appendix B.1.

if there are different driving mechanisms for the underlying instabilities either side of the transition. In this case, the trapped-electron-mode (TEM) instability becomes dominant above the threshold $k_y$; one indication of this is the shift to a negative real frequency, which indicates a drift in the electron diamagnetic direction. In addition to kinetic electrons, both magnetic field components $\delta A_\parallel$ and $\delta B_\parallel$ were then included – these are expected to be particularly important for the high-$\beta$ equilibrium. The introduction of both fluctuating magnetic field components $\delta A_\parallel$ and $\delta B_\parallel$ destabilizes KBMs for both equilibria at all radii. In simulations, we used the same value of local plasma $\beta$ (1.5% for the low-$\beta$ equilibrium and 3.7% for the high-$\beta$ one) on each radial surface for a given equilibrium, which does not reflect the true behaviour in tokamaks with peaked pressure profiles where inner flux surfaces should have a higher associated $\beta$ than the outer ones. Nevertheless, we have noted more representative local $\beta$ values in Table 2.1. As discussed in Section 1.4.3, we expect the addition of magnetic fluctuations, in particular the $\delta A_\parallel$ field-line bending, to stabilize the ITG instability. This can be observed more readily in the low-$\beta$ equilibrium, since the KBM and TEM are not the dominant

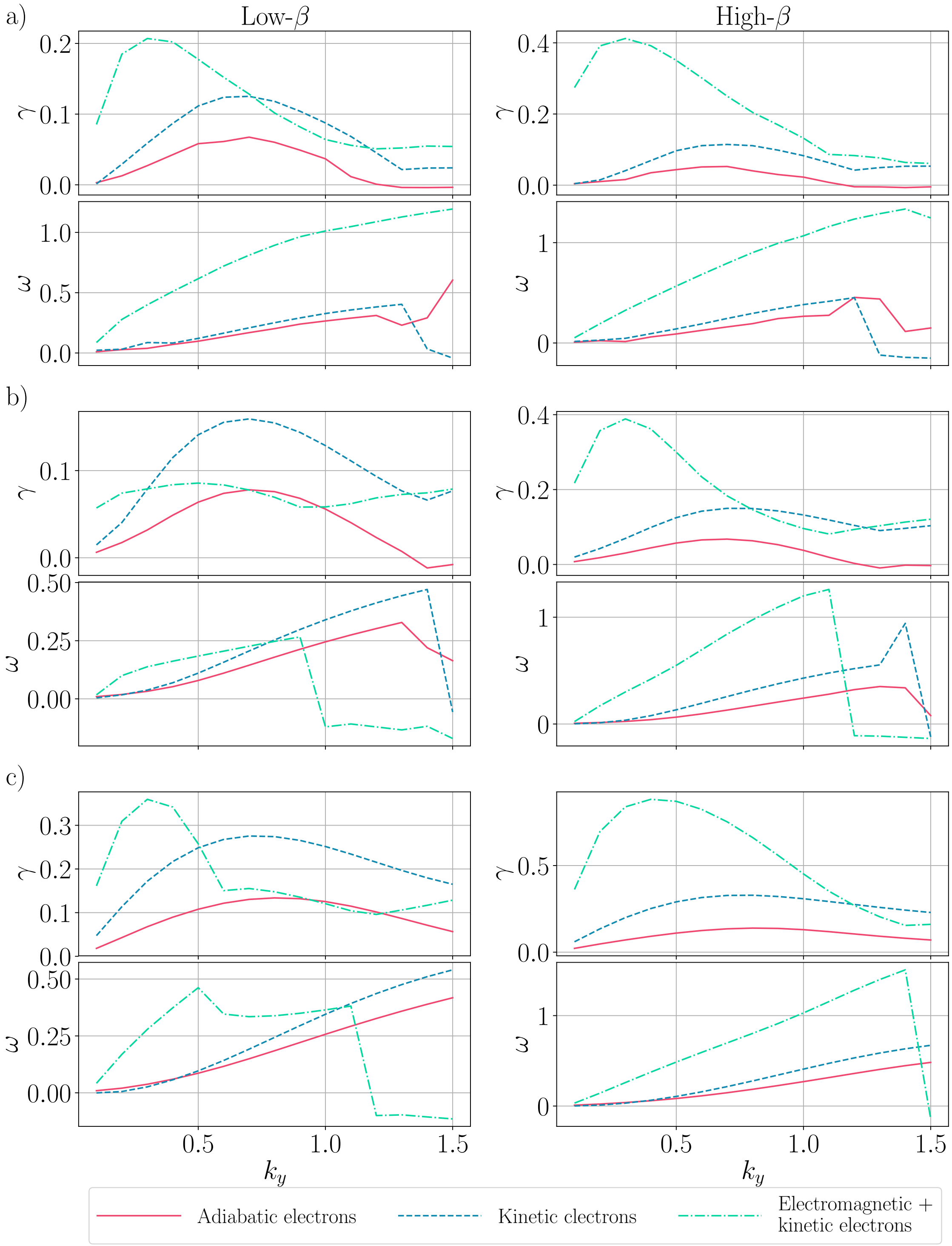

Figure 2.4: Linear growth-rate and real-frequency spectra for the two equilibria, showing the effects of adding kinetic electrons and electromagnetic perturbations. This was performed at all three radii of a) $\rho = 0.3$, b) $\rho = 0.5$ and c) $\rho = 0.75$.

mode at all $k_y$. The real frequency $\omega$ of the KBM is observed to be higher than for ITG by a factor of approximately $1/\sqrt{\beta}$. This increase in frequency is indicative of the dynamics being driven by Alfvén-speed dynamics, which occur on a timescale $\sqrt{\beta}$ shorter than thermal dynamics. This sensitivity of $\omega$ to $k_y$ is a feature that we use throughout the Thesis as a signature of the KBM. Studies were also performed with *only* $\delta A_{\|}$ *or* $\delta B_{\|}$ fluctuations. The electrostatic spectra were insensitive to the addition of $\delta B_{\|}$ compressive magnetic fluctuations – no KBM was destabilized and the ITG was not stabilized. With only $\delta A_{\|}$ field-line bending fluctuations, ITG stabilization was observed and a KBM appeared at low $k_y$ but with a growth rate approximately 50% smaller than with both fluctuating magnetic components. The inclusion of kinetic electrons and magnetic fluctuations has important consequences for linear stability in both equilibria. In the next two Sections we study the effects of flux-surface shaping including kinetic electrons with and without magnetic fluctuations, respectively.

## 2.2 Electrostatic shaping studies

In this Section, we study the effect of flux-surface shaping on electrostatic microstability in the two equilibria. In particular, we focus on the effects of elongation and triangularity on the microstability of the $\rho = 0.5$ surface. As such, the equilibrium parameters for the following simulations are from either of the columns with $\rho = 0.5$ in Table 2.1. In our electrostatic studies of the two equilibria (with $\beta = 1.5\%$ and 3.7%), we neglect magnetic perturbations and fix $\beta'$ to maintain the same magnetic geometry[2]. Since these are electrostatic studies, calling the two equilibria low-$\beta$ and high-$\beta$ is misleading. We instead choose to label them as low-$(\log p)'$ and high-$(\log p)'$, respectively[3].

---

[2] In `GS2`, $\beta$ and $\beta'$ can be set independently of one another.

[3] The rationale behind this choice of labelling is that by ignoring electromagnetic terms, we have artificially set $\beta \sim 0$. By fixing $\beta' \equiv \beta(\log p)'$, we argue that we are increasing $(\log p)'$ by different amounts to compensate for the artificial reduction in $\beta$. The distinction between the two equilibria then becomes one of $(\log p)'$ rather than $\beta$.

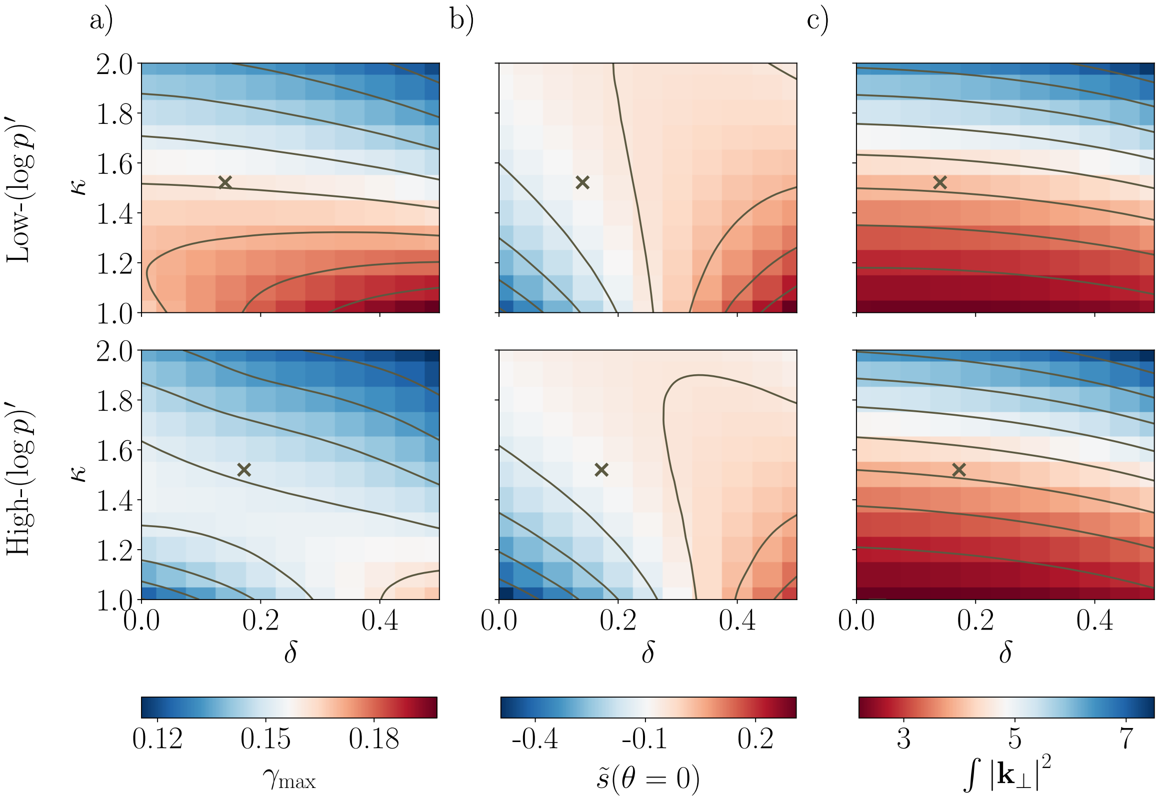

Figure 2.5: Scans in triangularity and elongation for two equilibria, showing a) maximum growth rates, b) local magnetic shear at the outboard midplane, c) integral of $|\boldsymbol{k}_\perp|^2$ over $-\pi/2 \leq \theta \leq \pi/2$. The black crosses indicate the nominal shapes. We note that the differences in local shear and $\int |\boldsymbol{k}_\perp|^2$ between the two equilibria are small. This is because whilst the low-$(\log p)'$ equilibrium has a normalized pressure gradient almost three times smaller than the high-$(\log p)'$ one, the increased $q$ and $R_0$ result in a comparatively similar value of $\alpha_{\text{MHD}}$, which governs the overall effect of pressure gradient on the geometrical coefficients. The colours have been chosen such that blue indicates increased stability.

### 2.2.1 Linear studies

We performed scans in elongation and triangularity with the nonlinear term in `GS2` disabled. All simulations were performed for ballooning chains with $\theta_0 = 0$, with $k_y$ ranging up to $k_y = 2$ and $|\theta - \theta_0| \leq 7\pi$. In Figure 2.5a), we show maximum[4] growth rates as a function of $\delta$ and $\kappa$. We did not expect scanning simultaneously in $\kappa'$ and $\delta'$ to be necessary, as wherever they appear in analytical expressions for $\boldsymbol{k}_\perp$ or $\tilde{s}$, they are accompanied by an extra factor of $\epsilon \simeq 0.2$ compared with $\kappa$ and

---

[4] This is the growth rate of the fastest-growing eigenfunction out of all the different-$\{k_x, k_y\}$ modes simulated. It is used throughout this Section as an indicator of stability.

$\delta$. To confirm this, we also performed coarse scans simultaneously scaling $\kappa'$ and $\delta'$ with $\kappa$ and $\delta$ by fixing $\kappa'/\kappa$ and $\delta'/\delta$. This had no effect on the qualitative trends observed in Figure 2.5a). The maximum growth rates changed by less than 10% for the majority of the $\{\delta, \kappa\}$ space, but reached $\sim 25\%$ at $\delta = 0.5$ and $\kappa = 1$. For the sake of simplicity, we did not simultaneously scale $\delta'$ and $\kappa'$ in any further simulations. The growth-rate spectra for all $\{\delta, \kappa\}$ peak in the ITG-dominated region. The high-$(\log p)'$ equilibrium has a lower maximum growth rate at every $\{\delta, \kappa\}$ compared with the low-$(\log p)'$ case. For the low-$(\log p)'$ equilibrium, increasing the elongation has an almost universal stabilizing effect. The only exception is at low $\delta$, where small increases in $\kappa$ are slightly destabilizing. The same behaviour is much more noticeable in the high-$(\log p)'$ equilibrium, where the maximum growth rate (for $\delta = 0$) occurs at $\kappa \simeq 1.4$. This destabilizing effect of elongation has not previously been reported in the literature. As triangularity increases, the elongation becomes monotonically stabilizing for both equilibria. The threshold $\delta$ at which increased elongation becomes stabilizing is around 0.1 and 0.3 for the low- and high-$(\log p)'$ equilibria, respectively. In both equilibria, the triangularity is destabilizing at low elongation and stabilizing at high elongation. The threshold $\kappa$ at which increased triangularity becomes stabilizing is around 1.4 for both equilibria. In both equilibria, maximal shaping minimizes the linear ITG instability. In the high-$(\log p)'$ equilibrium, the unshaped (i.e. circular flux-surface) equilibrium has a maximum growth-rate almost as small as with the maximal shaping. To see whether a circular flux surface can minimize the maximum growth rate, we artificially increased $|(\log p)'|$ by 50% for the high-$(\log p)'$ case. In this case, the $\{\delta, \kappa\} = \{0, 1\}$ toroidal ITG is almost completely stabilized, with a maximum growth rate of around 0.01 compared to around 0.08 for $\{\delta, \kappa\} = \{0.5, 2\}$ We note that for the high-$(\log p)'$ equilibrium scans with $\kappa'/\kappa$ and $\delta'/\delta$ fixed, the circular flux-surface shape has the smallest maximum growth rate.

To explain the trends seen in the growth rates, we define two metrics to try to capture the effects of drive and FLR damping which were introduced in Section 1.4.1. For drive damping, we use the local magnetic shear at the outboard midplane where $\theta = 0$ and ballooning modes such as ITG are driven most strongly. For FLR damping, we take the integral of $|\boldsymbol{k}_\perp|^2$ over the bad-curvature side of the tokamak where $-\frac{\pi}{2} < \theta < \frac{\pi}{2}$. A more negative value of $\tilde{s}(\theta = 0)$ will have a stabilizing effect, and we expect a larger value of $\int_{-\pi/2}^{\pi/2} |\boldsymbol{k}_\perp|^2$ to have a stabilizing effect. In Figures 2.5b) and c) we show these two parameters as a function of the shaping parameters. These were calculated numerically by following the procedure described in Appendix A.1. To demonstrate that the behaviour of these quantities can qualitatively predict the trends shown in maximum growth rates, we study the dependence of each one to one shaping parameter whilst the other is fixed at an extremal value. For $\kappa \simeq 1$, the outboard magnetic shear is rapidly made less negative by increasing triangularity. In contrast, the integrated wavenumber is quite insensitive to changes in triangularity, and so cannot compete with the change in the local shear. The expected net effect is therefore a strong destabilization, as is borne out in the growth rates. At $\kappa \simeq 2$, the outboard magnetic shear is quite insensitive to changes in triangularity, so the increasing integrated $|\boldsymbol{k}_\perp|^2$ gives a net stabilization as $\delta$ increases. At $\delta \simeq 0.5$, increased elongation boosts both drive damping and FLR stabilization, reducing the growth rate of ITG. Both effects work in tandem to provide the strong stabilizing effect of elongation at large $\delta$. We finally turn our attention to the novel destabilization with increased elongation observed at $\delta \simeq 0$. At this value of triangularity, increased elongation makes both the outboard magnetic shear *and* the integrated wavenumber more positive. These two effects can therefore compete to provide a non-monotonic behaviour in the growth rate. The position of the local maximum in the maximum growth rate depends on the sensitivity of both parameters to changes in $\kappa$.

Since one of the most notable difference between these two equilibria is the normalized pressure gradient, it should come as no surprise that the sensitivity of outboard magnetic shear to elongation changes with $(\log p)'$. To show this, we present in Figure 2.6 a scan in $\alpha_{\mathrm{MHD}}$ with $\kappa$ for the nominal values of the high-$(\log p)'$ equilibrium. In this $\{\alpha_{\mathrm{MHD}}, \kappa\}$ scan, increased elongation is stabilizing up to $\alpha_{\mathrm{MHD}} \simeq 1$, beyond which point it becomes destabilizing. The metrics for drive- and FLR-damping effects are included and are able to account for the qualitative behaviour observed. At small $\alpha_{\mathrm{MHD}}$,

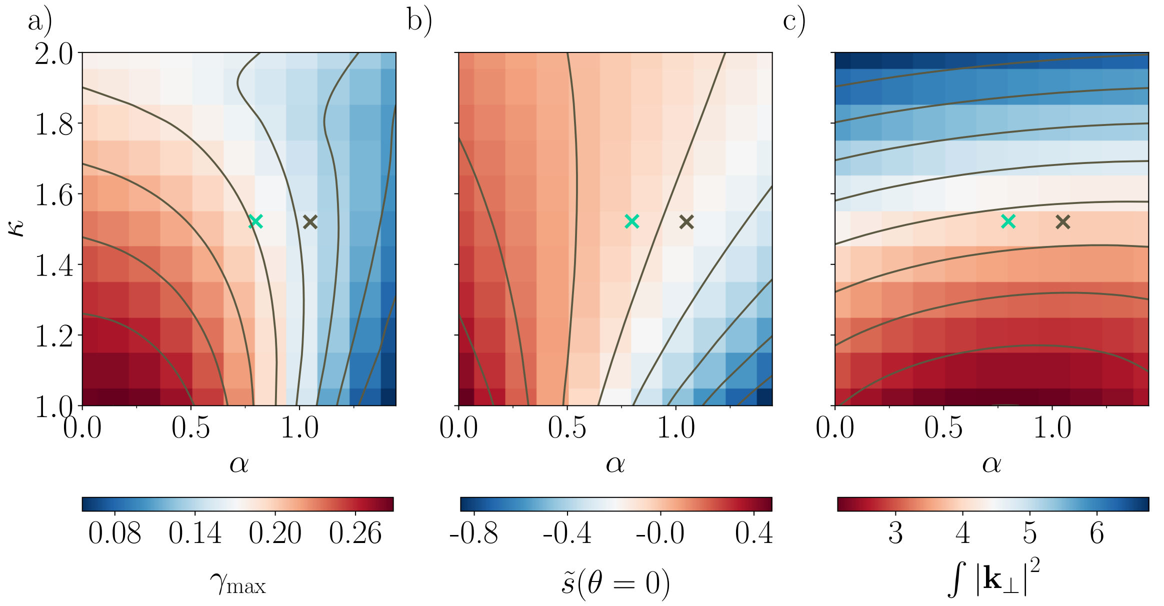

Figure 2.6: Electrostatic scans in $\alpha_{\mathrm{MHD}}$ and elongation for the high-$(\log p)'$ equilibrium at nominal triangularity ($\delta = 0.17$), showing a) linear growth rates maximised over $k_y$, b) local magnetic shear at the outboard midplane, c) integral of $|\boldsymbol{k}_\perp|^2$ over the bad curvature region. The green and black crosses indicate the nominal parameters for the low- and high-$\beta$ equilibria, respectively. The scan in $\alpha_{\mathrm{MHD}}$ was performed at fixed $q$ and $R_0$, so it corresponds to a scan in $(\log p)'$. The nominal $\{\alpha_{\mathrm{MHD}}, \kappa\}$ value for the low-$(\log p)'$ equilibrium is also shown by a green cross; a similar scan with the low-$(\log p)'$ equilibrium parameters gives qualitatively similar results.

both the outboard magnetic shear and the integrated wavenumber act to increase stability. As $\alpha_{\mathrm{MHD}}$ increases, the dependence of outboard magnetic shear on elongation reverses, so that above $\alpha_{\mathrm{MHD}} \simeq 0.5$, the local magnetic shear counteracts the FLR-stabilization afforded by increased elongation. At around $\alpha_{\mathrm{MHD}} \simeq 1$, we argue that the outboard magnetic shear becomes sensitive enough to changes in local magnetic shear that it out-competes the FLR stabilization, reversing the trend shown in the linear growth rates. With this in mind, we can understand why the low-$(\log p)'$ equilibrium, which has a slightly lower value of $\alpha_{\mathrm{MHD}}$, does not exhibit the non-monotonic stability trend with elongation as strongly as the high-$(\log p)'$ equilibrium. In Appendix A.2, we use a simplified analytical model that includes only the effect of $\kappa$ and $\alpha_{\mathrm{MHD}}$ to give expressions for $\tilde{s}$ and $|\boldsymbol{k}_\perp|$ that reflect the behaviour shown in the full equilibrium. We note that quasilinear heat-flux estimates were also calculated; however these predicted the low-$(\log p)'$ equilibrium to have a lower radial heat flux than the high-$(\log p)'$ case, which was not borne out in the nonlinear simulations presented in the next Section.

### 2.2.2 Electrostatic, nonlinear shaping scans

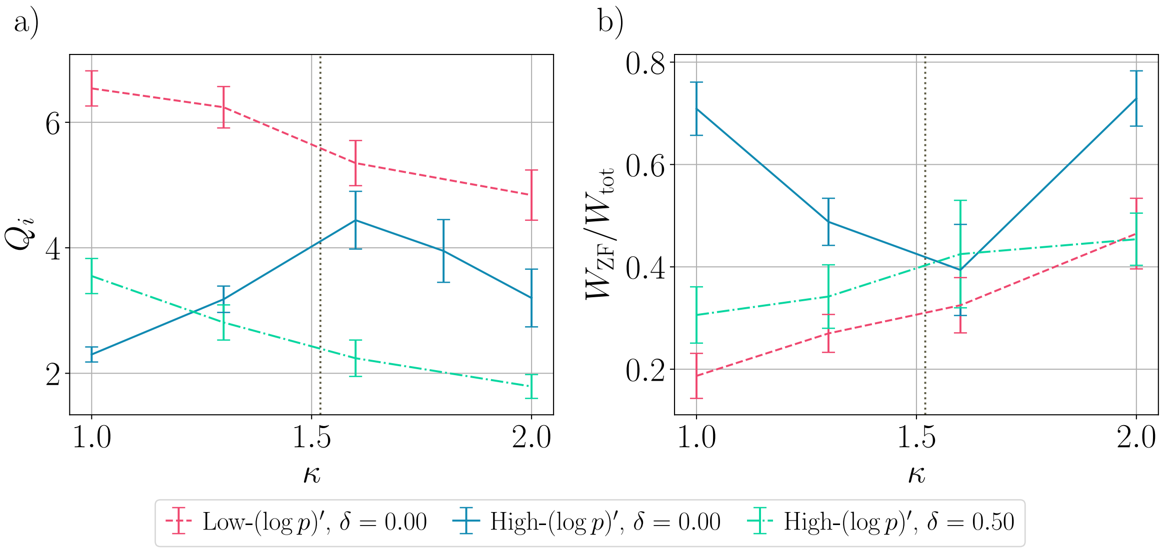

Figure 2.7: a) Ion heat flux and b) fraction of zonal energy as a function of elongation for each equilibrium. The dotted line indicates the nominal elongation.

Linear simulation results can give an indication of the trends expected to be observed in transport levels. In the following simulations in this Section, we include the nonlinear term in `GS2` to show transport levels as a function of triangularity and elongation. In all of the following simulations $\delta\phi$ was initialized with low-level $(10^{-3})$ noise in all of its three coordinates. The resolutions of the simulations are given in Table 2.2. These resolutions were guided by a thorough sensitivity study, which found that $\Delta k_y = 0.048$ was sufficiently small to resolve the turbulence, and that the shortest ballooning chains in the simulation should consist of no fewer than four $2\pi$ segments – this necessitated a large number of $k_x$ values. Unlike the linear simulations, we did not perform a full 2D scan as that would have been too computationally expensive. Instead we focus on testing how robust the novel destabilizing effect of elongation is when nonlinear effects are included. We performed scans in elongation in three cases; ion heat fluxes are presented in Figure 2.7. Electron heat fluxes are not shown but are

Table 2.2: Resolution parameters for nonlinear simulations in the three $\kappa$ scans.

| Item | Value | Description |
|---|---|---|
| `ntheta` | 32 | Parallel grid points per $2\pi$ domain |
| `negrid` | 16 | Number of energy grid points |
| $2 \cdot$ `ngauss` | 10 | Number of passing pitch angles per sign of $v_{\|}$ |
| `vcut` | 3 | Ratio of $v$ to $v_{\mathrm{th},s}$ above which $h_s = 0$ is forced |
| $\Delta k_y$ | 0.048 | Grid spacing in $k_y$ |
| $k_{y,\mathrm{max}}$ | 1 | Maximum $k_y$ |
| $2\pi\hat{s}\Delta k_y/\Delta k_x$ | 4 | Sets $k_x$ grid spacing |
| $N_{k_x}$ | 256 | Number of $k_x$ values |

qualitatively similar to the ion fluxes. For both the low-$(\log p)'$, $\delta = 0$ and high-$(\log p)'$, $\delta = 0.5$ cases, the ion heat flux is a monotonically decreasing function of elongation. For the high-$(\log p)'$, $\delta = 0$ case, increased elongation increases the ion heat flux up to $\kappa \simeq 1.6$. By further increasing elongation above this value, the ion heat flux becomes a decreasing function of $\kappa$. The qualitative trends in radial fluxes of heat are therefore the same as is observed in the maximum linear growth rates. Assuming that the linear interpolation between $\kappa = 1.3$ and 1.6 is correct, the exact value of $\kappa$ that maximises the heat flux is not the same as that which maximizes the linear growth rate. These results suggest that, for a $\beta \simeq 0$ equilibrium with a steep pressure gradient, the turbulent transport might be minimized by using circular flux-surfaces as opposed to non-triangular highly-elongated flux-surfaces. However, for a low or moderate pressure gradient, increased elongation is expected to reduce the radial turbulent transport.

As well as the ion heat fluxes, we show in Figure 2.7 the fraction of energy in the zonal flow. To calculate this, we take the ratio of the following proxies for the zonal and total energy contributions ($W_{\mathrm{ZF}}$ and $W_{\mathrm{tot}}$, respectively) [75]:

$$W_{\mathrm{ZF}} \propto \left\langle \sum_{k_x} \left(1 - \Gamma_{k_x,k_y=0}(\theta)\right) \left|\delta\phi_{k_x,k_y=0}(\theta)\right|^2 \right\rangle_\theta ;$$

$$W_{\mathrm{tot}} \propto \left\langle \sum_{k_x,k_y} \left(1 - \Gamma_{k_x,k_y}(\theta)\right) \left|\delta\phi_{k_x,k_y}(\theta)\right|^2 \right\rangle_\theta ,$$

where $\Gamma_{k_x,k_y}(\theta) \equiv I_0(b)\mathrm{e}^{-b}$ where $I_0(b)$ is the zeroth-order modified Bessel function of the first kind acting on $b \equiv k_y^2/2$ and $\langle \dots \rangle_\theta$ indicates an average over poloidal angle. For the low-$(\log p)'$ equilibrium at $\delta = 0$ and the high-$(\log p)'$ at $\delta = 0.5$ the zonal energy fraction increases monotonically with elongation, reflecting the decreased transport. Similarly, for the high-$(\log p)'$, $\delta = 0$ simulation the minimum zonal energy fraction coincides with the maximum heat flux. These results suggest that the effect of elongation on turbulent transport is closely linked to its effect on the relative strength of the zonal flow.

## 2.3 Electromagnetic shaping studies

We now turn our attention to studies of the effect of shaping with magnetic fluctuations included. We will therefore once again refer to the equilibria as low and high $\beta$. We previously showed in Figure 2.4 that the inclusion of electromagnetic fluctuations has a significant effect on the linear growth-rate spectra, destabilizing the KBM and stabilizing ITG. We performed a scan in $\delta$ and $\kappa$ while including both $\delta A_\parallel$ and $\delta B_\parallel$ fluctuations; maximum growth rates are shown in Figure 2.8a) and b) for the low- and high-$\beta$ equilibria, respectively. The metrics for measuring the $\{\delta, \kappa\}$-response of drive and FLR damping are unchanged from Figure 2.5. In the high-$\beta$ equilibrium, a KBM is excited for all $\{\delta, \kappa\}$ and the maximum growth rates are everywhere higher than the electrostatic case. Increased flux-surface shaping has a uniformly stabilizing effect, except at $\kappa = 1$ where the maximum growth rate is insensitive to $\delta$. In the low-$\beta$ equilibrium, the KBM is the dominant mode for the region of $\{\delta, \kappa\}$ space bounded by the green line in Figure 2.8a). Within the KBM-dominated region, the shaping is uniformly stabilizing, except at $\kappa = 1$ where we see the same behaviour as the high-$\beta$ case. Increasing $\kappa$ at low-triangularity does not destabilize the KBM in either equilibrium. In the ITG-dominated region outside of the green bounds, we generally see that increased triangularity has a weak destabilizing effect at all values of $\kappa$, and increased elongation can be either destabilizing or stabilizing. In both the ITG- and KBM-dominated regions the observed trends are qualitatively different to

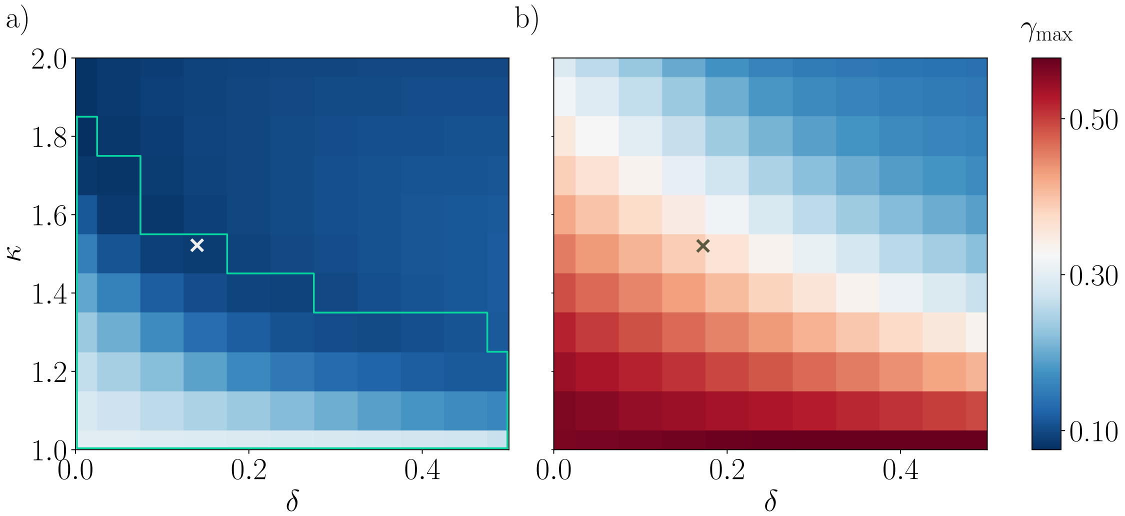

Figure 2.8: Electromagnetic scans in triangularity and elongation for the a) low-$\beta$ and b) high-$\beta$ equilibria, showing maximum growth rates. For the low-$\beta$ case, KBMs dominate in the region enclosed by the green line, whilst ITG is otherwise dominant. All dominant modes in the high-$\beta$ equilibrium are KBMs. The crosses indicate the nominal shape.

the electrostatic results, suggesting that flux-surface shaping affects electromagnetic instabilities in a way that is distinct from electrostatic ones.

To explain this difference, we note that there are extra coefficients of $|\boldsymbol{k}_\perp|^2$ and $|\boldsymbol{k}_\perp|$ in Equations 1.23 and 1.24 for the parallel and perpendicular current, respectively. We suggest that increasing $|\boldsymbol{k}_\perp|$ will therefore act to reduce the effects of these magnetic fluctuations. This is distinct from FLR stabilization, and originates from the curl of the magnetic field. We hereafter refer to the effect of increased shaping (and thus $|\boldsymbol{k}_\perp|$) on the magnetic fluctuations as the ‘magnetic-damping’ effect. This damping manifests itself in two distinct ways via its opposing effects on the KBM and ITG. In particular, increased magnetic damping should act to stabilize the KBM and destabilize the ITG. The magnetic-damping stabilization of the KBM is synergistic with the FLR damping, but opposes the FLR damping of ITG. Like FLR damping, we choose to use $\int|\boldsymbol{k}_\perp|^2$ as a metric for the strength of the magnetic-damping effect. In practise, we can therefore view the magnetic damping as adding extra weight to the FLR damping when considering electromagnetic instabilities, but reducing its weight for ITG.

We can now explain the observed phenomena in the context of these three effects of shaping. At $\delta = 0$, increasing elongation leads to a competition between the destabilizing effect of more-positive outboard magnetic shear and the stabilizing effects of larger averaged perpendicular wavenumber. For the electrostatic ITG instability, the outboard magnetic shear only needs to outcompete the FLR stabilization for increased elongation to have an overall destabilizing effect. However, for the KBM, the outboard shear competes against both FLR- and magnetic-damping effects. For both equilibria studied here, the outboard magnetic shear is not sensitive enough to elongation to provide a net destabilization of the KBM. A similar story presents itself for the effect on KBM-stability of increased triangularity at all values of $\kappa$. The more-positive outboard magnetic shear competes against both FLR and magnetic damping. Since FLR and magnetic stabilization effects are less sensitive to $\delta$ than $\kappa$, the outboard magnetic shear is able to balance the combination of $|\boldsymbol{k}_\perp|$ effects, but only at $\kappa = 1$. We argue that this results in the constant maximum growth rate there. Outside of the KBM regime, the FLR- and magnetic-damping mechanisms oppose each other. If both of the FLR and EM effects are of similar magnitude, we expect the overall shaping dependence of the ITG stability to approximately reflect that of the outboard magnetic shear. By studying Figure 2.5b), it can be seen that as the triangularity decreases from 0.5 *and* the elongation increases from 1 (i.e. diagonally up and to the left), the outboard magnetic shear tends to become less positive. We expect this to have a stabilizing effect on the ITG instability. By focusing only on the region of Figure 2.8a) that is outside the KBM regime (i.e. the upper-right-hand region, not enclosed by the green line), it is observed that the linear growth rates tend to decrease very slightly[5] as the triangularity decreases from 0.5 *and* the elongation increases from 1.3. This is in agreement with the expected effect of the outboard magnetic shear, lending credence to our argument.

---

[5] The maximum linear growth rate for $\{\delta, \kappa\} = \{0.5, 1.4\}$ is 0.12, whereas at $\{0.0, 2.0\}$, the maximum linear growth rate is 0.08.

One can question whether the local magnetic shear can ever be sensitive enough to changes in elongation that one can recover the destabilizing effect of increasing $\kappa$ for a KBM. Recall that in Figure 2.6 we showed that increased $\alpha_{\mathrm{MHD}}$ leads to increased sensitivity of the outboard magnetic shear to elongation. This suggests that a threshold for the KBM being destabilized by elongation may exist if $\alpha_{\mathrm{MHD}}$ is large enough. To show this, we performed a scan in $\beta$ at fixed $(\log p)'$ for the high-$\beta$ equilibrium. Two such scans were performed – one at the nominal value of $(\log p)'$ and one with a value 50% higher. The driving gradients were not simultaneously changed in the increased-$(\log p)'$ case. The maximum growth rates for the two scans are presented in Figure 2.9. Both scans share some features. At low $\beta$, increasing $\beta$ stabilizes the dominant ITG mode, before destabilizing a KBM. The threshold value of $\beta$ for the KBM to be destabilized increases with $\kappa$. As mentioned in Section 1.4.3, the KBM is partially stabilized at sufficiently high $\beta$ via second stability. This occurs in the high-$\alpha_{\mathrm{MHD}}$ region

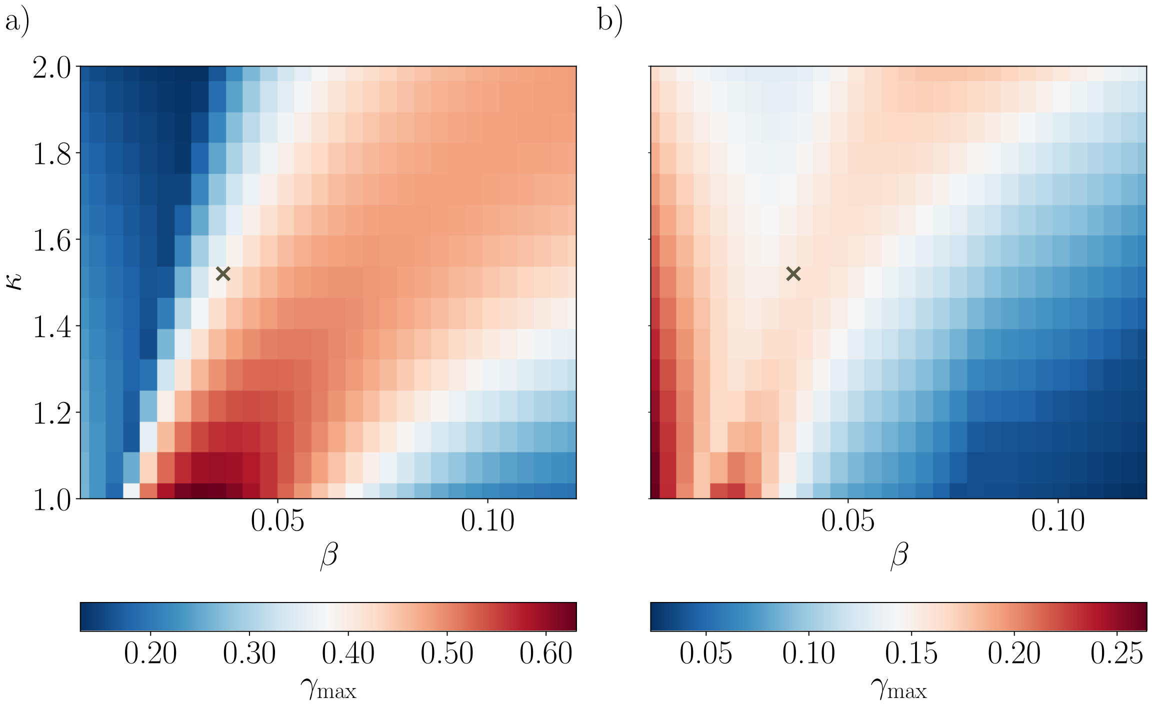

Figure 2.9: Electromagnetic scans in $\beta$ and elongation for the high-$\beta$ equilibrium, with $(\log p)'$ held fixed at a) nominal and b) 1.5 times nominal. The crosses indicate the nominal $\{\beta, \kappa\}$. Separate colour-bars are used to improve the contrast in the high-$(\log p)'$ case.

of $\hat{s} - \alpha_{\mathrm{MHD}}$ space where the MHD ideal ballooning mode is stable. The KBM persists (albeit with significantly reduced growth rates) into the region of second stability, as previously reported in [57], for sufficiently high $\beta \simeq 10\%$. This stabilization can be attributed to the increasing local-magnetic-shear stabilization due to larger $\alpha_{\mathrm{MHD}} \propto \beta$. As $\alpha_{\mathrm{MHD}}$ increases, the local magnetic shear becomes increasingly sensitive to changes to $\kappa$. Therefore, as elongation is increased in the region of second stability the local-shear stabilization is eroded rapidly enough that it outcompetes the FLR stabilization. As a result, increasing $\kappa$ moves the equilibrium out of the second-stability region, decreasing stability dramatically. As $\beta$ is increased, so does $\alpha_{\mathrm{MHD}}$, in turn reducing the outboard magnetic shear and providing a stabilizing effect. By increasing $(\log p)'$ by 50%, $\alpha_{\mathrm{MHD}}$ is 50% more sensitive to changes in $\beta$. As a result, the region of second stability is accessed at lower $\beta \lesssim 5\%$, and the degrading effect of $\kappa$ is correspondingly observed at lower $\beta$.

## 2.4 Conclusions

In this Chapter we presented a study of the effects of flux-surface shaping on two equilibria primarily distinguished by their value of plasma $\beta$. We prefaced this study by introducing the basic $\delta f$-gyrokinetic framework, as well as some of the key concepts of the local flux-tube approach used in gyrokinetic codes such as `GS2`. In doing so, we explained how shaping effects can enter the governing gyrokinetic-Maxwell system of equations, via the perpendicular wavenumber that appears when the equations are cast in spectral representation. The component of the perpendicular wavenumber in the field-line-label direction $\nabla\tilde{\alpha}$ was shown to include the local magnetic shear that is tied to drive damping, whilst the FLR damping is manifest as Bessel functions whose argument scales with $\boldsymbol{k}_{\perp}$. Following this, we introduced the two equilibria in detail before presenting a successful benchmark between the two local gyrokinetic codes `GS2` and `GKV` for electrostatic fluctuations and adiabatic electrons. We then presented the effects of including kinetic electrons and fluctuating magnetic fields in these two equilibria to show that the KBM is destabilized. With these preliminaries out of the way, we showed linear, electrostatic scans in the Miller parameters $\kappa$ and $\delta$ that govern the flux-surface shape. We found the novel result that, at small triangularity, elongation can increase the maximum linear growth rates of equilibria with steep pressure gradients. We explained, by defining metrics for the drive- and FLR-damping effects, all of the trends observed in the maximum growth rates. In particular, we noted that at small triangularity and large $\alpha_{\mathrm{MHD}}$, the local magnetic shear at the outboard midplane can be made more positive by increasing elongation. This destabilizing effect can compete with the FLR-stabilization afforded by increased $\boldsymbol{k}_\perp$ to give the non-monotonic maximum-growth-rate behaviour observed. We showed nonlinear simulation results of scans in elongation to show that increased elongation can result in increased transport levels. These electrostatic results correspond to $\beta \simeq 0$ electromagnetic simulations with very steep pressure gradients. As such, one may argue that they are unimportant for high-performance experiments where both $\beta$ *and* pressure gradients are typically expected to be high. Nevertheless, the concepts developed via these electrostatic simulations laid the foundation for studying the effects of flux-surface shaping in tandem with fully electromagnetic fluctuations.

We presented fully electromagnetic scans in triangularity and elongation for both equilibria. The inclusion of electromagnetic fluctuations leads to qualitatively different behaviour to the electrostatic case, as the KBM reacts differently to the shaping compared with the ITG instability. Namely, increased shaping has a stronger stabilizing influence on the KBMs. We explained all of the trends observed in the context of increased shaping damping the influence of the magnetic fluctuations. KBMs are more readily stabilized by increased shaping, and the ITG can be destabilized by more extreme shapes, due to the erosion of the EM stabilization. Nevertheless, we showed that for high performance plasmas with $\beta$ sufficient to access the region of KBM second-stability, the novel destabilizing effect of elongation can be reproduced. This has potentially significant ramifications for high-performance tokamaks expecting to utilize second-stability to gain improved performance at high $\beta$. Although nonlinear simulations were not performed with fully electromagnetic effects included, our linear results indicate that highly-elongated plasmas may significantly worsen the turbulent transport in such experiments. We note, however, some caveats. Whilst our conclusions hold for the presented shaping studies in which only elongation and triangularity were varied, they will not necessarily hold if other shaping parameters such as Shafranov shift and aspect ratio are varied. In real tokamak experiments, attempts to change the elongation and triangularity in isolation locally are extremely difficult, and generally result in changes to many other local equilibrium parameters. As a result, the findings of this Chapter may not readily be borne out in experiments. Additionally, there are implications of reduced shaping in terms of destabilizing dangerous MHD instabilities. The study of such MHD instabilities was beyond the scope of this work.

# Chapter 3

# Gyrokinetic studies of an internal transport barrier

Under certain circumstances, so-called transport barriers can form in tokamak plasmas. These are radially thin regions of the plasma where much-higher driving gradients can exist without extreme levels of transport, i.e. the heat conductivity of the plasma is significantly lower than usual. The confinement in tokamak plasmas that exhibit transport barriers is much improved [76, 77]. So long as the plasma is stable and can be sustained, this certainly improves the prospects of delivering fusion energy from a commercially-viable toroidal confinement device. The first transport barrier was observed in ASDEX at the edge of the plasma – similarly located transport barriers are known as edge transport barriers (ETBs) and are now routinely produced in experiments to improve confinement [7, 76].

Transport barriers can also be found in the core of the plasma – these are known as internal transport barriers (ITBs). ITBs have been observed in all of the major tokamaks across a variety of transport channels (i.e. ion and/or electron temperature and/or density) [77, 78]. For steady-state tokamak operation, the plasma current that generates the poloidal magnetic field should be driven via fully non-inductive methods. Moreover, *efficient* steady state operation is possible if the intrinsic current comprises a significant portion of the plasma current, reducing the need for external current drive. ITBs are considered important for efficient steady-state operation because the bootstrap current typically provides in excess of 50% of the plasma current, reaching as much as 80% in some JT-60U shots [79, 80]. The steep-gradient equilibria observed in transport barriers are not as well-studied as a typical tokamak equilibrium; as such there is no full understanding of an ITB formation mechanism. Nevertheless, there are several experimental observations that guide us towards some potentially important stabilization mechanisms. Typically, but not always, ITBs are observed coincidentally with regions of small or negative magnetic shear, once the input power is sufficiently high [81, 78, 82–87]. Since the magnetic shear appears to be a crucial ingredient in triggering ITB formation, the current drive is often tailored to create a non-monotonic $q$ profile that has a minimum at mid minor radius in the plasma [7]. ITB formation is also often correlated with steep gradients in the equilibrium plasma flow velocity perpendicular to the magnetic field [88–90]. As well as the above observations, ITBs are occasionally observed to form near low-order rational flux-surfaces [91, 92]. It is hypothesized that the MHD modes destabilized at these low-order rational surfaces can transiently increase the equilibrium flow shear which, in turn, stabilizes the microscopic instabilities driving turbulent transport [77]. We will not study such MHD activity in any detail in this work, but simply view it as a means of increasing the mean flow shear. Towards the top of an ITB, the plasma $\beta$ can become significant ($\beta \gtrsim 1\%$) – electromagnetic effects are expected to be have a significant on microstability in this case. Recent work has also predicted a completely distinct class of ITBs that is triggered by a resonant interaction between ion-driven turbulence and fast particles [93, 94]. This Thesis does not explore that class of ITBs, but we rather note in passing that there is likely no single mechanism for ITB formation.

In this Chapter, we continue our study of microstability in high-performance tokamak plasmas as we focus on a JET pulse that exhibited a strong internal transport barrier. In doing so, we will attempt to determine whether local $\delta f$ gyrokinetics contains the physics necessary to describe ITB formation. We begin in Section 3.1 by introducing the general features of the experiment, along with three different equilibria that are consistent with experimental measurements. We compare their key differences at two radial locations corresponding to the peak of the respective $L_{T_i}^{-1}$ profiles and

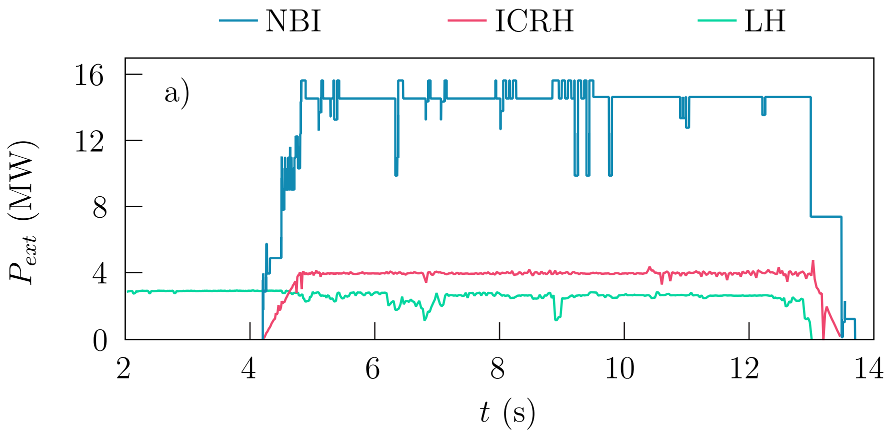

Figure 3.1: Time traces of the various sources of external heating power for JET pulse #53521.

outside the foot of the barrier. As discussed in Section 1.3.3, we present all quantities in a normalized form according to Appendix B. We focus first on the mid-barrier region in Section 3.2. Using both linear and nonlinear gyrokinetic simulations, we establish the key microscale instabilities that drive turbulence, and how the stability and transport responds to changes in key equilibrium parameters such as $\beta$, equilibrium flow shearing rate, and magnetic shear. In doing so, we determine the most important stabilization mechanisms in this mid-barrier location of the plasma. In Section 3.3, we present simulations of the outer region, which has more standard equilibrium parameters. Again, linear and nonlinear gyrokinetic simulations are used to study the stability and transport levels. We end in Section 3.4 by summarizing our findings.

## 3.1 Experiment and equilibria

We study JET pulse #53521, which ran in 2001 with an optimized magnetic shear profile [95]. Notably, this pulse was one of the longest duration optimised Shear JET discharges, running for 27 confinement times [96]. In Figure 3.1, we show the time traces of various sources of heating power as given in [97]. The ITB, typically characterized by a jump in the neutron rate, lasts from 5 to 13 seconds, coinciding with the addition of significant external heating. The plasma was heated by a variety of sources: 2.6-2.9 MW of the heating power was supplied by lower hybrid (LH) waves, 14.9 MW via deuterium neutral beam injection (NBI) and 4 MW by ion-cyclotron-resonance heating

(ICRH) of a hydrogen minority species. The use of LH heating also provides a source of current drive and is considered to be important for tailoring the $q$-profile to give small or negative magnetic shear in both JET and other devices [98, 99]. The main ion species was deuterium. This experiment was performed before the ITER-like wall was installed in JET. The most significant impurity source, and indeed the only one taken into account in this study, is carbon from the device wall. A strong ITB was observed in the ion temperature profile around 5 seconds into the pulse.

Experimental measurements were available for several key equilibrium parameters. Charge exchange measurements were used to calculate the ion temperature and toroidal rotation profiles, whilst the electron temperature was measured primarily via electron cyclotron emission. The electron density profile was measured using LIDAR. Visible bremsstrahlung radiation measurements were used to infer $Z_{\text{eff}} \equiv n_e^{-1} \sum_i n_i Z_i^2$, with the summation over each ion species $i$. However, these were not considered to be reliable as $Z_{\text{eff}}$ was reported as large ($\sim 4$) and constant across the entire radial profile. Some equilibrium information was not directly available from the experimental measurements, such as the plasma geometry, safety-factor and transport profiles. To generate these profiles in a self-consistent way (and therefore infer the missing equilibrium profiles), we used the JETTO transport code [100]. This solves a set of transport equations given sources of particles, momentum and heat, together with the Grad-Shafranov equation, in general toroidal geometry. These transport equations generally take the form

$$\frac{1}{V'} \frac{\partial}{\partial t}\bigg|_{\tilde{\psi}} V' \langle A \rangle_{\tilde{\psi}} + \frac{1}{V'} \frac{\partial}{\partial \tilde{\psi}} V' \langle a_A \rangle_{\tilde{\psi}} = \langle S_A \rangle_{\tilde{\psi}}, \tag{3.1}$$

where $\tilde{\psi}$ is the flux-surface label first defined in Chapter 1, $V$ is the volume enclosed by a flux surface, a derivative with respect to $\tilde{\psi}$ is denoted by a $'$, $\langle \ldots \rangle_{\tilde{\psi}}$ indicates a flux-surface average, and $A$ denotes a macroscopic quantity such as density, angular momentum or temperature [21]. The corresponding radial flux is denoted by $a_A$, and $S_A$ indicates the external source.

JETTO was run in interpretive mode for the ion temperature, electron density and temperature, and toroidal angular velocity – this means that these profiles were provided and used to calculate other profiles such as safety factor or fluxes. The plasma boundary was computed using EFIT [101]. Since JETTO was run in interpretive mode, its main purpose was to provide self-consistent magnetic geometry and heat, particle and momentum fluxes. To enable JETTO to calculate the fluxes, we supplied it with the various relevant sources, as well as fitting profiles at multiple times during the pulse. In practice, to calculate each flux, we assembled the relevant outputs of JETTO according to Equation 3.1 and rearranged for $\langle a_A \rangle_{\tilde{\psi}}$. The particle fluxes were sourced by NBI, ionization and recombination. The momentum flux was sourced by the torque on the plasma, e.g. from NBI, and also contains a contribution from the particle flux due to the bulk rotation of the plasma. The calculated heat flux took into account sources of heat from NBI, RF heating, LH heating, radiative losses such as Bremsstrahlung, and ion-electron energy exchange. We supplied various models for the source terms. For NBI, the PENCIL code was used [102]; this was set up according to the experimental logs that described how each NBI module was configured experimentally. Similarly, for the LH and ICRH sources, we used FRTC and PION codes, respectively [103, 104]. There are assumptions inherent in these codes that lead to sources of uncertainty beyond those of the raw experimental data itself. For example, the PENCIL code assumes that $Z_{\text{eff}}$ is constant across the radial profile and that $T_i(\tilde{\psi}) = T_e(\tilde{\psi})T_i(0)/T_e(0)$. In particular the assumption that the ion and electron temperatures can be associated by a constant is rather crude, and introduces further uncertainties into the predicted profiles. Nevertheless, we have not assigned specific quantitative uncertainties to any outputs of JETTO.

The profiles were fitted by using a combination of spline (in Profile Maker [105]) and manual (i.e. by eye with simple functions) fitting. All simulations were performed 8 seconds into the pulse because a strong ITB was present at that time. The simulation profiles were interpolated between the two nearest times for which experimental data was provided. There are significant error estimates on the experimental profiles which allows for a broad range of profiles to be fitted to the different data. To illustrate this,

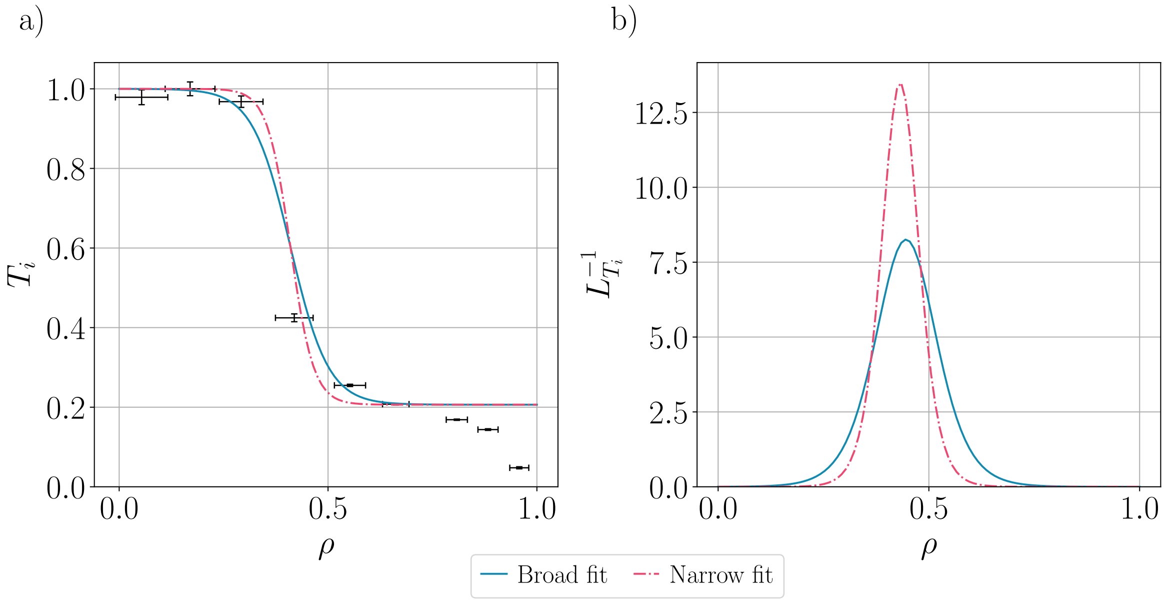

Figure 3.2: Two different fits to the experimental data in the mid-barrier region, using offset tanh functions of varying widths. The radial coordinate $\rho$ is the square root of the toroidal magnetic flux, normalized to its value at the last closed flux surface. No attempt was made to fit the data beyond the point at $\rho > 0.7$ – we merely aim to show how the sparsity of measurements and their significant error bars allow us to fit such a broad variety of ion temperatures in the mid-barrier region.

we show in Figure 3.2 the ion temperature data along with two fits in the mid-barrier region 8.12 seconds into the pulse. As is shown, it is eminently possible to fit a wide range of profiles to the ion temperature profile. The two simple fits shown are close to the bounding cases for a simple tanh fit, but more complex fits can achieve more extreme values of $L_{T_i}^{-1}$ if desired.

Since there is such significant uncertainty in the experimental profiles, some of the key parameters such as $\hat{s}$, $L_{T_i}^{-1}$, $\gamma_{E\times B}$ and $\beta$ can vary significantly depending on exactly how one chooses to fit the data. In this Thesis, we study three reasonable fits to the equilibrium at the chosen time, to study microstability and microturbulence over a range of equilibria that are broadly consistent with the available measurements. We label these equilibria as A, B and C; the next subsections provide details on the rationale behind the three different fits, whilst Figure 3.3 shows some of the key profiles for each equilibrium.

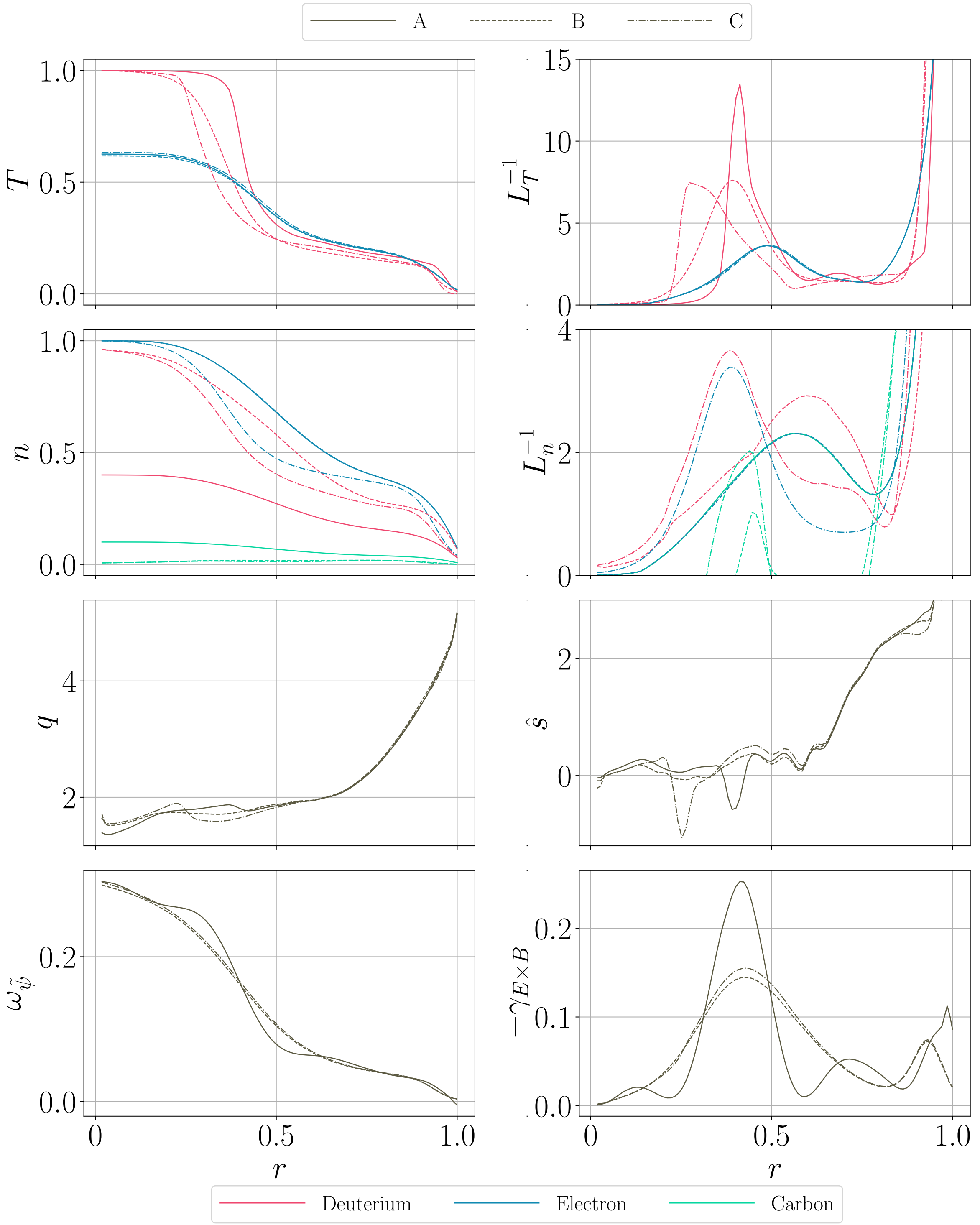

Figure 3.3: Profiles of the three different self-consistent equilibria studied in this Chapter.

### 3.1.1 Equilibrium A

To generate equilibrium A, we used spline fitting for the ion and electron temperatures, the electron density and the toroidal mean flow. The ion densities were determined by using $Z_{\text{eff}}$ calculated from visible bremsstrahlung radiation. This large and constant value of $Z_{\text{eff}}$ used for equilibrium A means that the deuterium density is 60% of the electron density at all radii. One key feature of equilibrium A is the tall and narrow peak in $L_{T_i}^{-1}$ that approximately corresponds with the also-narrow peak in the $\gamma_{E\times B}$ profile. Although the density profiles in equilibrium A vary relatively slowly with $r$, the total pressure gradient is sufficiently large to create a region of negative magnetic shear that coincides with the barrier[1].

### 3.1.2 Equilibrium B

In Equilibrium B, we relaxed the temperature and toroidal flow gradients as much as possible within experimental error, whilst keeping the barrier location approximately the same as for Equilibrium A. To achieve this, equilibrium B was fitted manually by using a combination of linear and tanh functions for the ion and electron temperatures, electron density and toroidal flow. In contrast to equilibrium A, charge exchange data was used to infer a $Z_{\text{eff}}$ profile by directly measuring the thermal hydrogenic ion density. As a result, the deuterium density was much closer to the electron density compared with equilibrium A. Notably, the shallow gradient of this fit to the ion temperature was less proficient at generating a bootstrap current, resulting in a magnetic shear profile that does not go significantly negative at any radius.

### 3.1.3 Equilibrium C

Equilibrium C was fitted with the aim of generating a region of strong negative magnetic shear along with a reduced peak $L_{T_i}^{-1}$. Similar to equilibrium B, we fitted manually the ion and electron temperatures, electron density and toroidal flow, using linear and tanh functions, and used charge-exchange data to infer the ion density. Similar to equilbrium A the $T_i$ profile was fitted to have a flat top, which has been observed in

---

[1] Note that the safety factor depends on the pressure profile due to the bootstrap current – steep pressure gradients result in a strong toroidal plasma current that locally adjusts $q$ and therefore $\hat{s}$.

other ITB pulses [106, 107]. This leads to a strongly asymmetric $L_{T_i}^{-1}$ profile and lends itself well to generating a strongly negative magnetic shear via the bootstrap current. Another consequence of this $T_i$ fit is that the minor radius at which $L_{T_i}^{-1}$ is maximal moves radially inwards from $r \simeq 0.4$ to $r \simeq 0.3$. This means that the peak in $L_{T_i}^{-1}$ is not coincident with the peak in $\gamma_{E\times B}$ and that the plasma $\beta$ at the peak $L_{T_i}^{-1}$ is well above that of equilibria B and C. The electron density profile for equilibrium C was fitted to enhance the peak in $L_{n_e}^{-1}$ and $L_{n_i}^{-1}$ profiles as much as possible within experimental error bars. As a result, the peak moves to lower $r$. Finally, the toroidal flow profile was fitted in a similar way to equilibrium B.

## 3.2 Mid-barrier simulations

In this Section we focus on microstability and turbulence in the mid-barrier, which we define as the radial position where the inverse temperature length scale is maximal. The physical parameters of the three equilibria at their respective mid-barrier positions are given in Table 3.1. We note that the profile of triangularity contained small (amplitude $\sim 0.01$) oscillations around $\delta \simeq 0.05$. This leads to large variations in $\delta'$, which is likely not representative of its true behaviour. We performed sensitivity scans which confirmed that the variation in $\delta'$ had no significant effect on linear stability. We first focus on the trends in linear stability observed with electrostatic and fully electromagnetic fluctuations. In doing so, we will identify a candidate equilibrium that can be studied in more detail, for example via the inclusion of equilibrium flow shear. These linear results will guide us towards a set of equilibrium parameters, with which we can match experimental flux levels, that are at the very least close to a self-consistent equilibrium.

### 3.2.1 Identifying a candidate equilibrium

Given the steep temperature gradients combined with low heat diffusivity inherent in a transport barrier, we expect that the challenge in matching experimental flux levels will come in getting the simulated fluxes small enough. We will use the linear growth rates as a proxy for nonlinear saturated flux levels to identify the candidate equilibrium

Table 3.1: Physical parameters for the three equilibria in the mid-barrier region. These values are normalized according to Appendix B. The contribution to $\beta$ of a species $s$ can be calculated by multiplying $\beta_{\mathrm{ref}}$, $T_s$ and $n_s$.

| Parameter | A | B | C |
|---|---|---|---|
| $r$ | 0.405 | 0.39 | 0.27 |
| $R$ | 3.21 | 3.272 | 3.29 |
| $\hat{s}$ | -0.431 | 0.226 | -0.68 |
| $q$ | 1.783 | 1.738 | 1.651 |
| $R_0'$ | -0.241 | -0.297 | -0.249 |
| $\kappa$ | 1.47 | 1.48 | 1.50 |
| $\kappa'$ | -0.24 | -0.35 | -0.43 |
| $\delta$ | 0.049 | 0.052 | 0.057 |
| $\delta'$ | 0.005 | 0.274 | -0.062 |
| $\beta_{ref}(\%)$ | 4.77 | 5.04 | 4.87 |
| $-\beta'$ | 0.317 | 0.294 | 0.362 |
| $\gamma_{E\times B}$ | 0.254 | 0.139 | 0.074 |
| $\omega_\psi$ | 0.155 | 0.168 | 0.238 |
| $T_i$ | 0.616 | 0.471 | 0.7898 |
| $L_{T_i}^{-1}$ | 13.46 | 7.597 | 7.327 |
| $T_e$ | 0.472 | 0.492 | 0.602 |
| $L_{T_e}^{-1}$ | 2.818 | 2.39 | 0.76 |
| $n_D$ | 0.323 | 0.727 | 0.806 |
| $L_{n_D}^{-1}$ | 1.659 | 1.743 | 1.999 |
| $n_e$ | 0.808 | 0.835 | 0.890 |
| $L_{n_e}^{-1}$ | 1.659 | 1.486 | 1.629 |
| $n_C$ | 0.081 | 0.018 | 0.014 |
| $L_{n_C}^{-1}$ | 1.659 | -0.242 | -1.893 |
| $\nu_D(\times 10^{-5})$ | 6.04 | 8.99 | 4.64 |
| $\nu_e(\times 10^{-3})$ | 5.41 | 5.07 | 4.19 |
| $\nu_C(\times 10^{-3})$ | 0.89 | 1.32 | 0.68 |

likely to exhibit the best confinement. To identify such a candidate from our three equilibria, we will study the linear stability with and without magnetic fluctuations and equilibrium flow shear. As with Chapter 2, all of the simulations in this Chapter are performed using the local gyrokinetic code `GS2`. Unless otherwise stated, all simulations in this Section use 32 grid points per $2\pi$ segment in poloidal angle (which parametrizes the distance *along* a field line).

#### 3.2.1.1 Electrostatic fluctuations

We initially present results of simulations that exclude magnetic fluctuations, i.e. $\delta A_{\|} = \delta B_{\|} = 0$. Growth-rate and real-freqency spectra at $\theta_0 = 0$ are presented in Figure 3.4, up to at most $k_y = 2$. At the scales simulated, all of the spectra are dominated by drift-wave instabilities in the ion diamagnetic direction, as identified by the positive real frequency at all unstable wavenumbers. The spectra all peak close to $k_y = 1$. We identify this as the toroidal ITG instability by noting the ballooning (peaked at $\theta - \theta_0 = 0$) nature of the eigenmodes. A typical mode structure is shown in Figure 3.6 for $k_y = 0.97$. At low $k_y$ (i.e. $k_y \lesssim 0.5$) the dominant mode for all equilibria is no longer the toroidal branch of ITG. Instead, a series of distinct modes dominates the low-$k_y$ spectrum, as indicated by a staircase of discontinuous jumps in the real-frequency spectrum of each equilibrium. We will temporarily refer to these modes as 'auxiliary' modes. The width of the auxiliary modes (in $k_y$) changes with the equilibrium. For equilibrium A and C, they are quite broad, whilst they are narrow and most clearly distinguishable in equilibrium B. For equilibria A and B, the impact of the auxiliary modes appears to be restricted to $k_y \lesssim 0.5$. For equilibrium C, however, they have a subtle impact on the growth-rate spectrum up to at least $k_y \simeq 1$: several peaks are just visible on top of the toroidal ITG continuum. These modifications to the growth rate are not distinguishable on the real-frequency spectrum. Equilibrium C is also the most stable at all scales simulated.

#### 3.2.1.2 Electromagnetic fluctuations

The values of electron[2] $\beta$ are 1.8%, 2.1% and 2.6% for equilibria A, B and C respectively. The same respective main-ion contributions to $\beta$ are 0.9%, 1.7% and 3.1%. At such values of $\beta$, magnetic fluctuations are expected to be important, either by

---

[2] Electron $\beta$ is relevant because the electrons typically carry the majority of the fluctuating current.

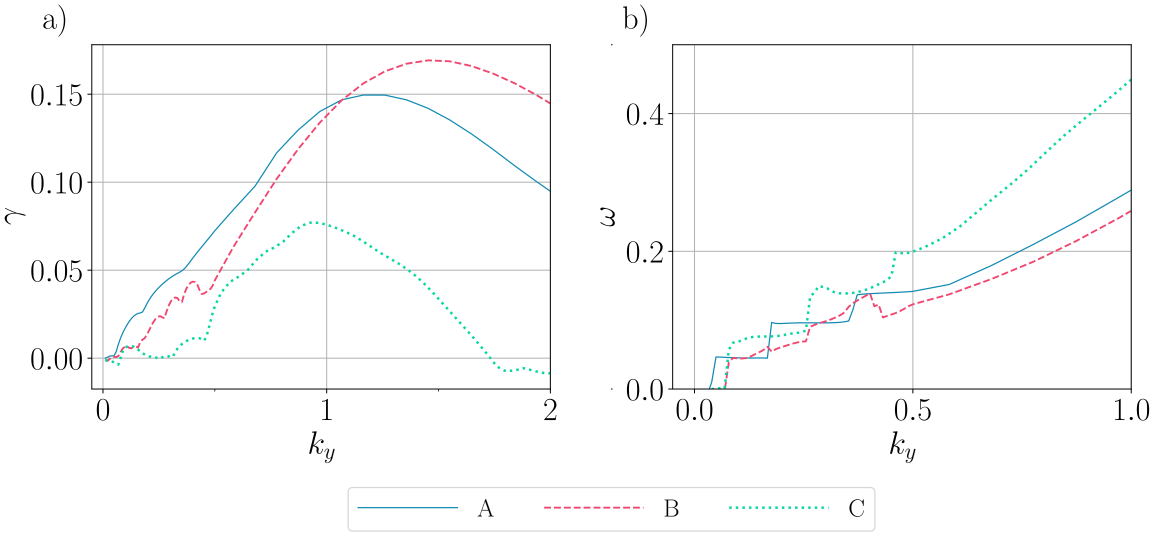

Figure 3.4: Electrostatic a) growth-rate and b) real-frequency spectra at $\theta_0 = 0$ for the three equilibria. The low-$k_y$ portions $k_y \lesssim 0.5$ of these ballooning-space simulations were run with $\Delta k_y = 0.01$ with highly-extended ballooning chains $|\theta| \leq 19\pi$ since the low-$k_y$ auxiliary modes extended far along the field lines. At higher $k_y$, the simulations were run with $\Delta k_y = 0.1$ and shorter ballooning chains with $|\theta| \lesssim 9\pi$.

stabilizing ITG or destabilizing kinetic ballooning modes (KBMs) as was observed in Chapter 2. Growth-rate and real-frequency spectra from simulations that included magnetic fluctuations $\delta A_\parallel$ and $\delta B_\parallel$ are shown in Figure 3.5. At $k_y \simeq 0.2$, a KBM is destabilized in all three equilibria. We identify the KBM via its structure along the field line (ballooning, peaked at the outboard midplane) and by the sensitivity of its real frequency to $k_y$ as discussed in Chapter 2. In all three equilibria, the toroidal ITG branch is more stable than in the electrostatic case, as expected. The toroidal ITG in equilibrium A is stabilized the least, with the maximum growth rate decreasing by 20%. Similarly, the maximum growth-rates in equilibria B and C are reduced by around 40% and 50%, respectively. As with the electrostatic simulations, these results continue to suggest that of the three equilibrium studied, C would minimize the radial transport. Therefore, in what follows, we will focus only on the stability of equilibrium C. We note that the auxiliary modes are still present. This can be seen via the humps on top of the usually-smooth toroidal-ITG branch. This suggests that the auxiliary modes are not as strongly stabilized by field-line bending and compression as the toroidal ITG. At

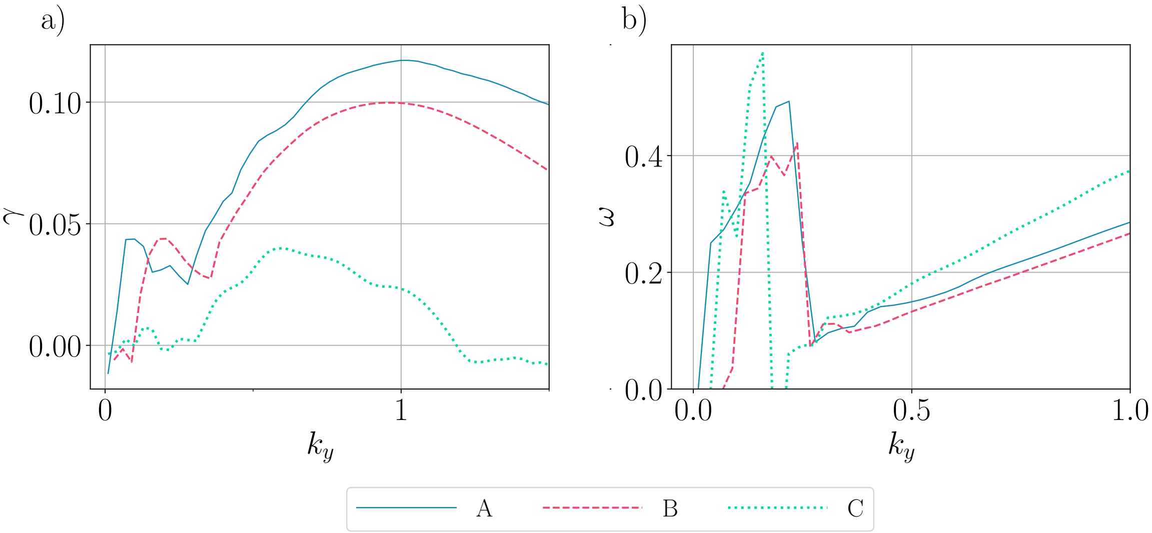

Figure 3.5: Fully electromagnetic (both $\delta B_{\|}$ and $\delta A_{\|}$) a) growth-rate and b) real-frequency spectra at $\theta_0 = 0$ for the three equilibria. The simulations were performed with $\Delta k_y = 0.03$ and a maximum $|\theta| \leq 19\pi$.

low-$k_y$, we hypothesize that the auxiliary modes are subdominant to the KBM, though an eigensolver has not been used to confirm this.

#### 3.2.1.3 Origin of the auxiliary modes

Before presenting further results on the effects of flow-shear and variations to magnetic shear, we discuss the origin of the low-$k_y$ auxiliary modes and how they modify the toroidal ITG spectrum. We begin by focusing on purely-electrostatic results. As can be seen from Figure 3.4, the auxiliary modes are most discernible in the electrostatic low-$k_y$ growth-rate and real-frequency spectra of equilibrium B. The eigenmode structure for these auxiliary modes is distinct from that of the toroidal-ITG. We show in Figure 3.6 a selection of four eigenfunctions at different values of $k_y$. The first three values of $k_y$ coincide with the local maxima of each 'band' of the auxiliary modes, whilst the fourth lies in the toroidal-ITG branch. The simulated $\theta$ domain extended up to $\theta - \theta_0 = \pm 19\pi$, but we show only a zoomed-in portion of it.

There are several key features of this Figure. At all values of $k_y$ shown, the eigenfunctions have a local maximum at $\theta - \theta_0 = 0$. Only for $k_y = 0.97$, which is representative of the dominant modes for $k_y \gtrsim 0.5$, is this also the global maximum. At the three

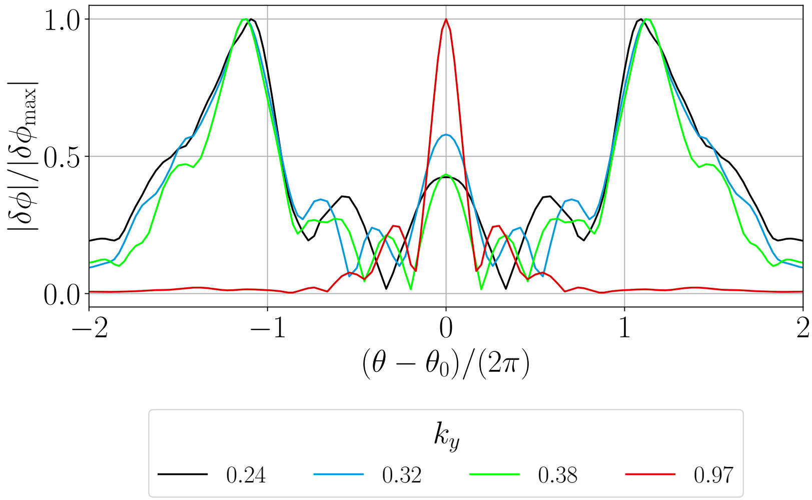

Figure 3.6: Mode structures along the field line for equilibrium B at four values of $k_y$ with $\theta_0 = 0$.

lowest values of $k_y$ shown, the global maximum of the eigenfunction is at $\theta - \theta_0 \simeq 2.3\pi$. For the low-$k_y$ modes, the eigenfunction has multiple local maxima in the intermediate region between $\theta - \theta_0 = 0$ and the global maximum[3]. These local maxima appear on both the good- and bad-curvature sides of the device, indicating that their drive mechanism is not necessarily dependent on curvature or $\nabla B$ drifts. As $k_y$ increases from 0.24 to 0.32 and then to 0.38, the number of local maxima in the intermediate region increases with each jump in $k_y$. Other than that, these low-$k_y$ eigenfunctions exhibit no qualitative differences to one another. This suggests that the different bands in the auxiliary mode spectrum are a consequence of the different modes in the intermediate region. As a result, we focus first on identifying the origin of these local maxima. In a loose sense, the increased number of local maxima with $k_y$ indicates an increased $k_\parallel$, even though simple periodic solutions cannot be used to describe modes living in a toroidal system with finite magnetic shear. With this in mind, we propose that these auxiliary modes could be slab-ITG modes that are able to compete with and modify the toroidal ITG that usually dominates ion scales. Unlike the toroidal branch, slab ITG requires finite $k_\parallel$ for instability, and does not depend upon the magnetic drifts to couple together the density and temperature fluctuations. Instead, it relies on parallel

---

[3] Local maxima are also visible for $|\theta - \theta_0| > 2.3\pi$ but these are less obvious so we do not focus on them.

ion dynamics to generate density fluctuations that drive $\boldsymbol{E} \times \boldsymbol{B}$ flows in a feedback loop [108]. An infinite parallel domain can support a continuous set of modes with infinitesimally small $k_\parallel$ spacing. One can plot a complex-frequency spectrum $\omega(|\boldsymbol{k}_\perp|, k_\parallel)$ for such a domain and trace out the contour that maximizes $\gamma$ at each $|\boldsymbol{k}_\perp|$. This will be a smooth line in the $\{|\boldsymbol{k}_\perp|, k_\parallel\}$ space, so the real frequency is a smooth function of the perpendicular wavenumber. Alternatively, in a domain with finite parallel extent, only a discrete set of parallel wavenumbers can be supported, so we would expect discontinuities in the real-frequency spectrum along the contour. In the simulations, the parallel domain extends far beyond the extent of the mode, so the discrete nature of the real-frequency spectrum is not a numerical artefact caused by low parallel resolution. This indicates that the parallel extent of the mode is constrained by a physical mechanism. We suggest that this mechanism is FLR damping brought about by magnetic shear. FLR damping can place an upper limit on the parallel domain length in which modes can exist, and allows for a scenario where discrete bands of slab-ITG modes can be observed in a toroidal system.

The above argument does not explain why the global maximum of the eigenfunction for low-$k_y$ modes exists at $\theta - \theta_0 \simeq 2.3\pi$. Well-versed readers may spot similarities between this study and recent work by Parisi et al., which presented microstability analysis of electron-temperature-gradient (ETG) modes in the pedestal [109]. In that work, Parisi found that the strong magnetic shear and short temperature length scales present in pedestal conditions lend themselves to driving dominantly the toroidal-ETG at $k_y\rho_e \ll 1$ and slab ETG at $k_y\rho_e \sim 1$. Given the inherent similarities between the pedestal and the ITB studied in this work, we are compelled to consider whether the dominant peak in the eigenfunction at low $k_y\rho_i$ is due to toroidal ITG. We first consider what is required for slab and toroidal ITG (or ETG) to be driven strongly. For strong slab-ITG drive, we require that the drive frequency $\omega_{*,\eta_i}$ and the parallel streaming frequency $k_\parallel v_{\mathrm{th},i}$ are of similar size, where

$$\omega_{*,i} \equiv \frac{k_y c T_i}{Z_i e B L_{n_i}}. \tag{3.2}$$

This requires that

$$\frac{k_y}{k_\parallel}\frac{\rho_i}{L_{T_i}} \sim 1. \tag{3.3}$$

When the ion temperature length scale is very short, i.e. $R_0 L_{T_i}^{-1} \gg 1$, slab ITG can remain strongly driven by increasing $k_\parallel$ accordingly. A similar condition can be calculated for toroidal ITG by balancing the drive frequency and magnetic drift frequency $\boldsymbol{V}_{D,i} \cdot \boldsymbol{k}_\perp$ to generate the following condition for strong drive:

$$\frac{R_0}{L_{T_i}} \sim \frac{|\boldsymbol{k}_\perp|}{k_y}. \tag{3.4}$$

For short ion temperature length scales, toroidal ITG may only be driven strongly when $|\boldsymbol{k}_\perp| \gg k_y$. By inspection of Equation A.28, it can be seen that this condition on $|\boldsymbol{k}_\perp|$ and $k_y$ can be satisfied if $\hat{s}(\theta - \theta_0) \sim R_0 L_{T_i}^{-1}$. The small magnetic shear ($\hat{s} = 0.23$) for equilibrium B in the simulation shown limits how readily this condition can be achieved[4]. The dominant peak in the eigenfunctions of three lowest-$k_y$ modes shown in Figure 3.6 corresponds to $|\hat{s}(\theta - \theta_0)| \simeq 1$, whilst $R_0 L_{T_i}^{-1} \simeq 25$. As such, the condition for *strong* drive is not met. Nevertheless, even weakly-driven toroidal ITG could be responsible for the dominant peak in the eigenfunction at low $k_y$. We have not performed any further studies to validate this.

To convince the reader that the auxiliary modes do indeed originate at least in part from slab ITG, we strip out much of the physics that should not be needed to drive the instability. We remove both the carbon impurity and electrons as kinetic species, turn off collisions, use circular flux surfaces, set $L_{n_i}^{-1} = 0$ and set $\hat{s} = 0$ (in practice we set $\hat{s} = 10^{-6}$ to avoid numerical divide-by-zero errors, but this value of $\hat{s}$ is small enough that periodic boundary conditions can be imposed along the magnetic field). The local magnetic shear is still allowed to vary, e.g. due to finite $\beta'$ and $R_0'$, but this is not incompatible with periodic parallel boundary conditions. The growth-rate and real-frequency spectra up to $k_y = 1$ are shown for this case in Figure 3.7 along with mode structures at several values of $k_y$. Despite stripping out much of the physics, we are still able to observe qualitatively similar behaviour to that seen in the full equilibrium

---

[4] For comparison, the equilibria studied by Parisi had $\hat{s} \simeq 3$ and $R_0 L_{T_e}^{-1} \simeq 130$.

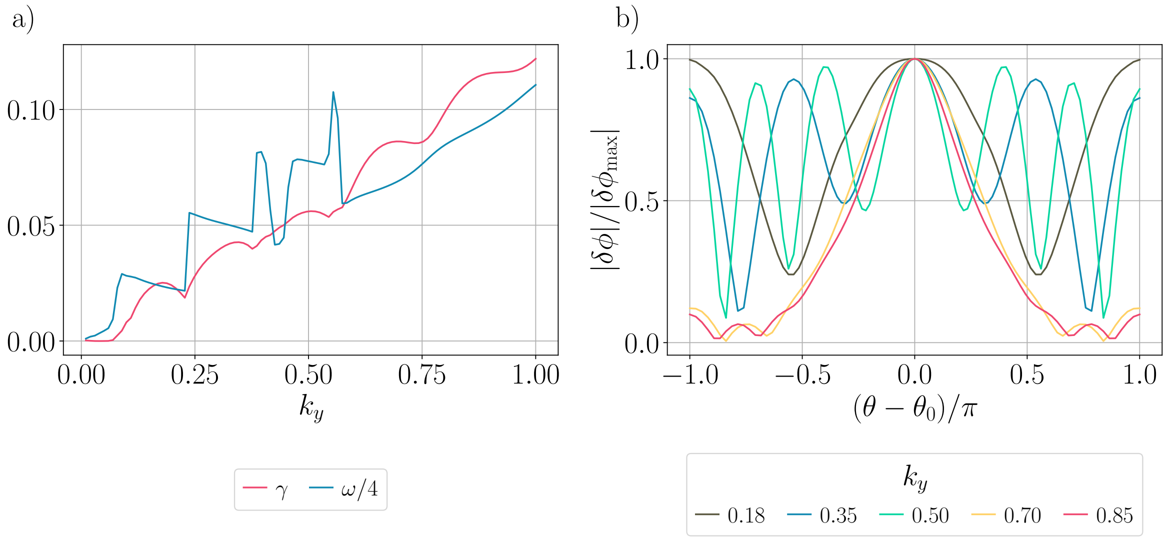

Figure 3.7: a) Electrostatic growth-rate and real-frequency spectra for a stripped-down version of equilibrium B with a single ion species, no collisions, circular geometry and no magnetic shear. The jumps in real-frequency at $0.4 < k_y < 0.6$ are not spurious – they reflect the fact that modes with very similar growth rates are competing with one another in this range of $k_y$. b) Mode structures along the field line for this stripped-down equilibrium at various values of $k_y$. The $k_y$-resolution is $\Delta k_y = 0.01$ and 64 points were used parallel to the field line.

– a staircase of auxiliary modes at lower $k_y$ followed what was assumed to be a toroidal-ITG branch at higher $k_y$. It is also clear from Figure 3.7 that the auxiliary modes can happily exist in the good-curvature region of the where $\pi/2 < |\theta| < \pi$ and $\omega_{D,i} < 0$. We believe that this is sufficient evidence to label the auxiliary modes as predominantly slab ITG, and the higher-$k_y$ modes as regular toroidal ITG. The different steps in the real-frequency spectrum correspond to slab modes with different parallel wavenumbers, though the eigenmodes are not purely sinusoidal as one might expect from slab ITG. This is due to the presence of magnetic drifts and *local* magnetic shear. The magnetic drifts modify the response in an order-unity way, whilst the local magnetic shear FLR damps the mode by modifying the perpendicular wavenumber. The transition from slab to toroidal ITG is evident in the eigenfunction, which becomes strongly peaked at the outboard midplane above $k_y \simeq 0.6$. Nevertheless, for $k_y \gtrsim 0.6$, the modulation in the growth rate (and also subtly in the real frequency) spectrum indicates that some remnant of the slab modes is present. Sure enough, we see that the tails of the eigenmodes contain oscillations whose wavelength decreases as $k_y$ increases.

The toroidal branch of ITG is typically the dominant mode observed for $k_y \lesssim 1$ in core simulations of tokamak plasmas. This raises the question of why we observe slab ITG in competition with the toroidal branch in these equilibria. One key feature of all three equilibria is that the inverse temperature length scale is several times shorter compared with non-ITB equilibria, for which $L_{T_i}^{-1} \simeq 1 - 3$ typically. The ratio of density to temperature length scales, $\eta_i$, can range anywhere from 3 to 10 depending on how we fit the ion temperature and density profiles. We can compare the dispersion relations for toroidal and slab ITG to see how they scale with the driving gradients of temperature and density well above marginal stability. Ignoring magnetic-fluctuation effects, the toroidal-ITG growth-rate well above marginal stability scales like $\gamma \sim (\omega_{*,i}\omega_{D,i}\eta_i)^{1/2} \propto (L_{T_i}^{-1})^{1/2}$ [14], where $\omega_{*,s} \equiv -k_y c T_s/(Z_s e B L_{n_s})$ and $\omega_{D,s} \equiv \boldsymbol{V}_{D,s} \cdot \boldsymbol{k}_\perp$. The slab-ITG growth rate scales like $L_{T_i}^{-1}$, as is shown in Appendix C.2. The toroidal branch tends to dominate at lower $L_{T_i}^{-1}$ due to order-unity differences in the coefficients. However, at sufficiently high $L_{T_i}^{-1}$, the slab branch is able to compete with the toroidal ITG due to the stronger scaling. In the steep-gradient region of a transport barrier where $L_{T_i}^{-1}$ can be $\sim 10$, it is therefore unsurprising that the slab modes are dominant at some scales [109].

Up until this point, we have only considered auxiliary modes in the context of electrostatic fluctuations – we now consider electromagnetic effects. We noted in the linear nominal simulations of all three equilibria that the inclusion of fully electromagnetic fluctuations makes the slab-ITG modifications to the toroidal-ITG branch more pronounced. As discussed in Section 1.4.3, it is well known that field-line bending can stabilize slab and toroidal ITG. We observe that slab ITG becomes more important than the toroidal branch when EM effects are included, which suggests that the slab branch is stabilized less effectively than the toroidal one. In Appendix C we derive a dispersion relation for a deuterium-electron plasma in unsheared slab geometry including FLR effects and $\delta A_\parallel$ fluctuations. We show in Figure 3.8 how the slab-ITG growth-rate and real-frequency spectra are affected in such a system for $k_\parallel = 0.5$. Our calculation suggests that the slab ITG is not significantly stabilized at higher $k_y$. In contrast, the toroidal branch of ITG is stabilized more strongly by similar increases in

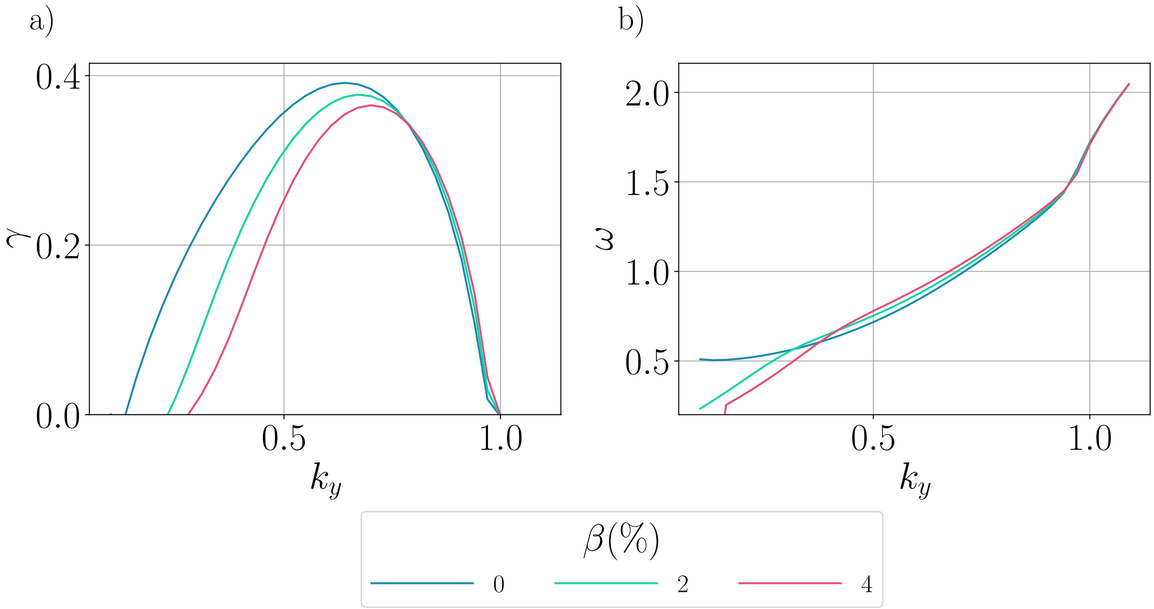

Figure 3.8: Numerical solutions for a) growth-rate and b) real-frequency spectra in unsheared slab geometry with fluctuating electric and parallel magnetic vector potential (including FLR effects). Results are shown for a deuterium-electron plasma with $T_i = T_e$, $n_e = n_i$, $L_{n_i}^{-1} = L_{n_e}^{-1} = 0$, $L_{T_i}^{-1} = 15$ $L_{T_e}^{-1} = 2$, $k_x = 0$ and $k_\| = 0.5$.

$\beta$. This is consistent with the increased prominence of the slab ITG modes once fully EM effects are included.

In the following Sections, we will explore the response of equilibrium C to both flow shear and variations in parameters such as $\hat{s}$ and $L_{T_i}^{-1}$. We expect the slab modes to respond differently to these effects compared with toroidal ITG and KBMs. As discussed, the slab-mode drive is not dependent on magnetic drifts, and the mode appears to be less sensitive to EM effects. As a result, we expect that the slab modes should primarily respond to magnetic shear via its effect on the FLR damping rather than drive or magnetic damping[5]. In the same way, the slab modes are expected to be less-strongly stabilized by perpendicular sheared flows compared with toroidal ITG. Nevertheless, the parallel component of equilibrium flow shear is still expected to have a destabilizing effect on the slab modes – this is discussed in Appendix C. The

---

[5] The concept of magnetic damping was introduced in Chapter 2.

combination of these two flow-shear effects suggests that the slab branch of ITG could be dominant over a wider range of scales when flow-shear effects are considered.

### 3.2.2 Equilibrium C – parameter scans

Based on the linear stability of the three equilibria studied in the previous Section, we concluded that equilibrium C is the most appropriate starting point for determining a self-consistent equilibrium that is also consistent with experimental profiles and fluxes. In this Section, we present sensitivity scans in a variety of parameters that are expected to be important for transport levels. In particular, we study the effect of varying $\gamma_{E\times B}$, $\hat{s}$, $L_{T_i}^{-1}$ and $\beta$.

#### 3.2.2.1 Equilibrium flow shear

Since $\gamma_{E\times B}$ is thought to be one of the main candidates for facilitating the formation of transport barriers, and since the flow-shear profile in the mid-barrier region can be peaked, we have studied the effect of flow-shear on the linear stability in some detail. Just like the temperature profiles, there is plenty of freedom to choose the flow-shear profile due to the significant error bars on the experimental data. We therefore performed scans in shearing rate $\gamma_{E\times B}$, independent of any other parameters, with the various components of flow-shear enabled. This means that we performed simulations including the effects of *both* perpendicular and parallel flow shear, as well as with just perpendicular *or* parallel flow shear. The latter simulations are not self-consistent, as the parallel and perpendicular components are fixed by the magnetic geometry. However, they are useful for studying separately the effects of the parallel and perpendicular shear.

We expect the gradient in the parallel component of the toroidal velocity (PVG) to generally increase linear growth rates, whilst we can infer the effect of perpendicular shear by studying the growth-rate spectra in both $k_y$ and $\theta_0$. Such growth-rate spectra with and without magnetic fluctuations for equilibrium C are shown in Figure 3.9. Only positive $\theta_0$ values are shown, but negative values give the same results. In both cases, we see finger-like structures extending in $\theta_0$ away from the toroidal-ITG stability

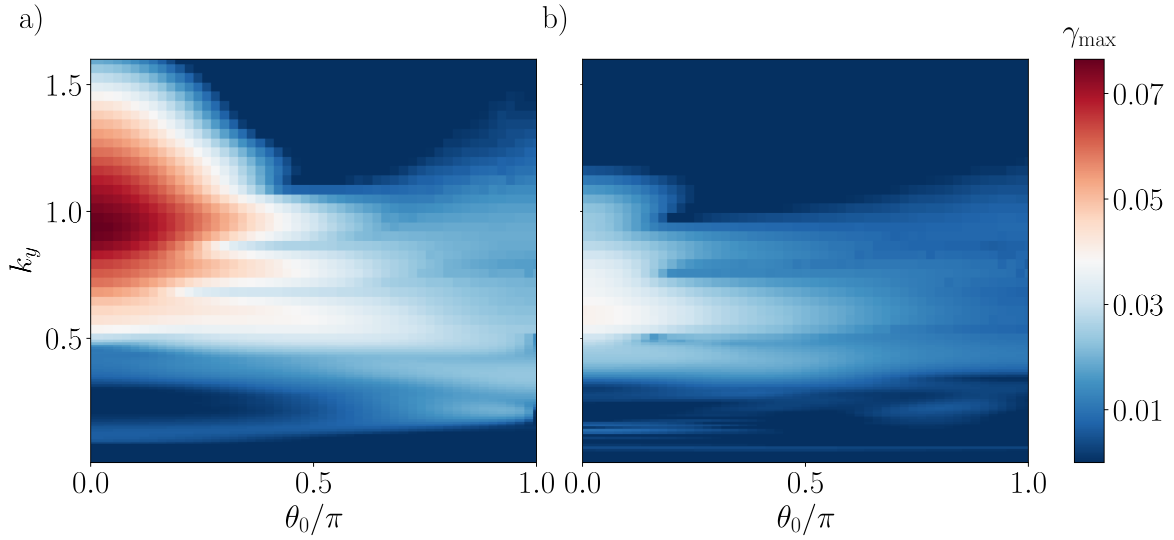

Figure 3.9: Growth-rate spectra for equilibrium C a) without and b) with magnetic fluctuations included. Only positive $\theta_0$ are shown, but negative $\theta_0$ values are identical by symmetry. Flow shear effects are not included. For $k_y \leq 0.5$, simulations were performed with $\Delta\theta_0 = 0.06$ and $\Delta k_y = 0.01$. For $k_y > 0.5$, simulations were performed with $\Delta\theta_0 = 0.06$ and $\Delta k_y = 0.03$.

boundary. These structures coincide with the slab-ITG modifications to the $\theta_0 = 0$ growth-rate spectra shown in Figures 3.4 and 3.5. As expected, the slab character of these modes is less-affected by changes to $|\boldsymbol{k}_\perp|$. We also see that the slab-ITG modes move to different $k_y$ as we scan in $\theta_0$, so the position and width of peaks in the Floquet-averaged growth-rate spectrum are expected to change with the addition of perpendicular flow shear. The inclusion of magnetic fluctuations makes the extended structures even more prominent by stabilizing the toroidal ITG branch.

With the $\{k_y, \theta_0\}$ spectra in mind, we proceed to present results from scans in $\gamma_{E\times B}$, varying which components of flow shear are enabled. We scanned $\gamma_{E\times B} \in \{0.04, 0.08, 0.12, 0.16\}$ to cover a spread of shearing rates that could all be plausible in the mid-barrier region. All simulations including perpendicular flow shear were performed with the continuous-in-time flow shear algorithm recently implemented in `GS2` [24]. These linear simulations were performed with 32 grid points per $2\pi$ in poloidal angle and 16 values of $\theta_0$ in the range $\pm\pi$. The number of $k_x$ grid points was chosen to ensure that fluctuation amplitudes were sufficiently small at the ends of each parallel

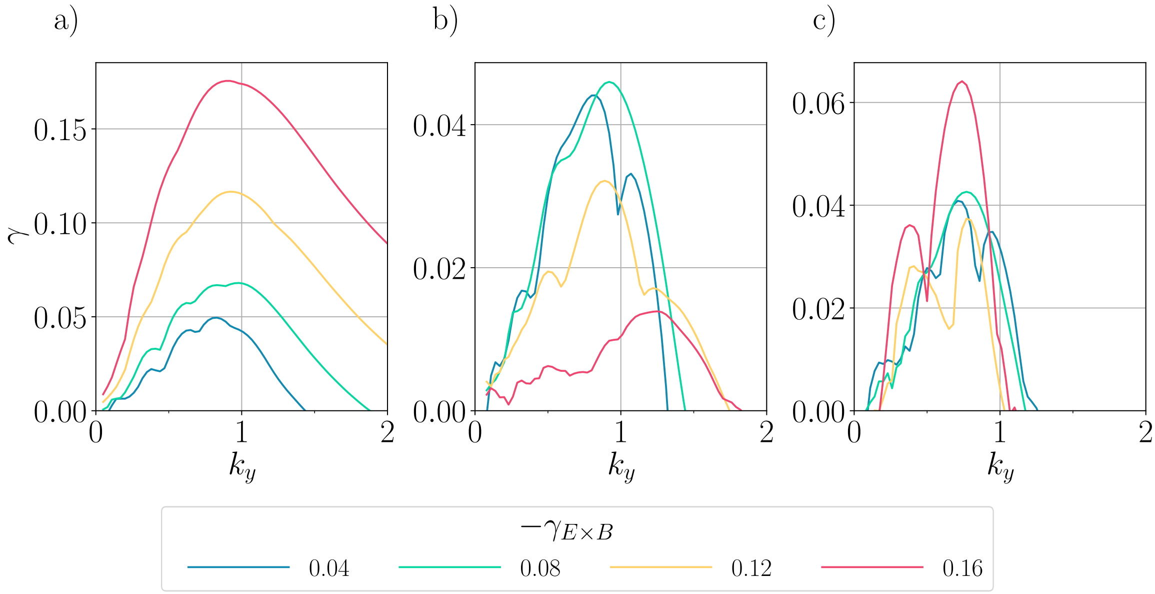

Figure 3.10: Linear growth-rate spectra for equilibrium C with a) only PVG, b) only perpendicular shear and c) both PVG and perpendicular shear. Only electrostatic fluctuations are included. Where perpendicular shear is included, the growth rate shown is the average over 15 Floquet periods. Growth rates with only PVG are averaged over $\theta_0$. The $k_y$ resolution is $\Delta k_y = 0.03$.

domain: approximately 70 and 270 values of $k_x$ were used for the largest and smallest values of $k_y$, respectively. Electrostatic scan results are presented in Figure 3.10.

By increasing the shearing rate with only the PVG included, the growth rates increase at almost all scales as expected. The exception is for an increase of shearing rate from zero to 0.04 where the stability increases at $k_y \gtrsim 1.3$, which is not understood. As $\gamma_{E\times B}$ is increased, the prominence of the bumps in the growth-rate spectrum that originate from slab-like modes decreases; by $\gamma_{E\times B} = 0.16$, the toroidal ITG is barely affected by the slab branch. This suggests that the toroidal ITG is destabilized more aggressively by the PVG than the slab-like modes at high shearing rates. When any purely-perpendicular flow shear is included, the Floquet-averaged growth rate at each $k_y$ is universally lower than with no flow shear at all. This can be seen by comparing the maximum growth rate at a given $k_y$ from Figure 3.9a) with the Floquet-averaged growth rates at each $k_y$ in Figure 3.10b). Continuing with the purely-perpendicular results, we find that the Floquet-averaged growth rates are fairly insensitive to changes in $\gamma_{E\times B}$

from 0.04 up to around 0.12. There is little qualitative difference between $\gamma_{E\times B}$ values of 0.04 and 0.08, although the growth rates do unexpectedly increase with increasing $\gamma_{E\times B}$ for $k_y \sim 1$. We will explore this observation further after presenting the electromagnetic results, as the behaviour is more exaggerated there. Once $\gamma_{E\times B}$ is raised well above the maximum linear growth rate in the unsheared case, we see stabilization up to $k_y \simeq 1.5$. This is consistent with the usual idea that the perpendicular shearing rate should exceed the linear growth rate of a given instability in the presence of no flow shear for there to be a significant stabilizing effect [110].

When both parallel and perpendicular flow-shear effects are included, we expect to see a competition between the two effects. Perhaps the most straightforward conclusion to be drawn from Figure 3.10c) is that at $\gamma_{E\times B} = 0.16$, the destabilizing effect of PVG outcompetes the perpendicular-shear stabilization for $k_y \lesssim 1$. At smaller shearing rates, the picture is less clear; the growth-rate spectra for $\gamma_{E\times B} \in \{0.04, 0.08, 0.12\}$ are similar and it is unclear which value of $\gamma_{E\times B}$ would minimize the turbulent transport. However, we expect that shearing rates larger than 0.12 would lead to increased transport due to strong PVG destabilization. We also note that while both PVG and perpendicular shear individually allow for unstable modes at $k_y \gtrsim 1.3$, the combination of the two does not – this is not understood.

We next present the effects of flow-shear when full electromagnetic effects ($\delta A_\parallel$ and $\delta B_\parallel$) are included. As before, we present in Figure 3.11 growth-rate spectra with and without the different flow-shear components. Focusing on the effect of PVG first, we note that as the strength of the PVG is increased, the linear growth rates tend to increase. A KBM is destabilized at around $k_y \simeq 0.2$. This is shown in more detail by Figure 3.12, which compares the linear growth-rate spectra for $\gamma_{E\times B} = 0$ and $\gamma_{E\times B} = 0.04$ with only PVG included. At $\theta_0 \simeq 0$, the toroidal-ITG branch is stabilized, leaving behind just the slab branch. At low-$k_y$ and finite $\theta_0$, a KBM is strongly destabilized. These two effects are indicative of an increased effect of $\delta A_\parallel$, suggesting a coupling mechanism between $\delta A_\parallel$ and PVG as previously reported in [111]. The slab bands that extend away from $\theta_0 = 0$ are more extended with the

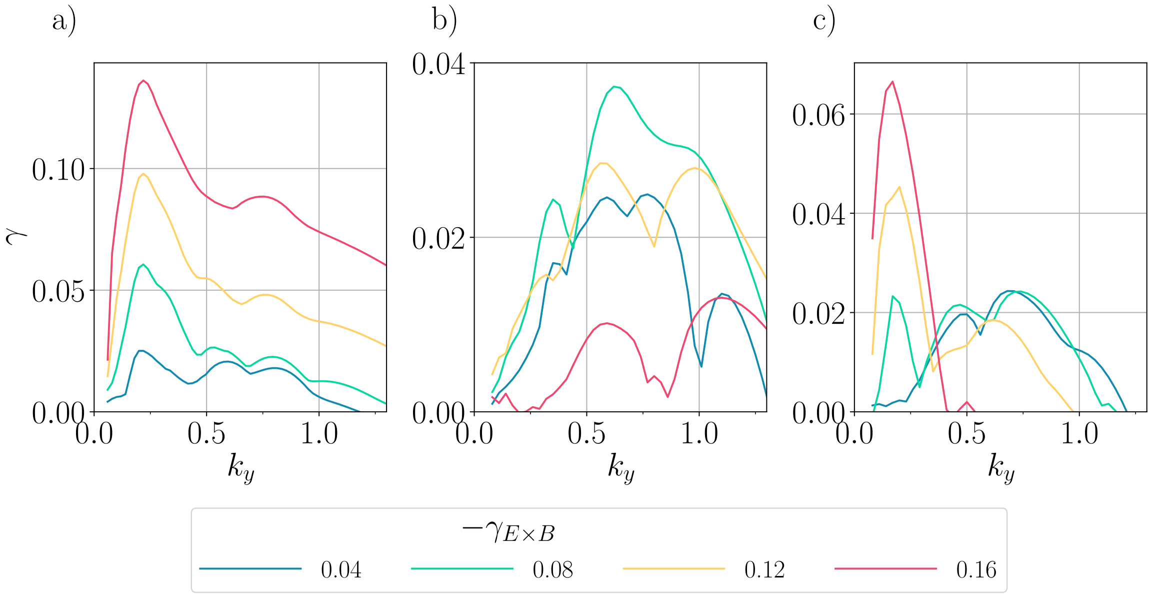

Figure 3.11: Linear growth-rate spectra for equilibrium C with a) only PVG, b) only perpendicular shear and c) both PVG and perpendicular shear. Fully electromagnetic fluctuations, with both $\delta A_{\|}$ and $\delta B_{\|}$ fluctuations, are included. Where perpendicular shear is included, the growth rate shown is the average over 15 Floquet periods. Growth rates with only PVG are averaged over $\theta_0$. The $k_y$ resolution is $\Delta k_y = 0.03$.

inclusion of parallel flow-shear effects, which was also observed for purely electrostatic fluctuations.

We next shift our attention to the results with purely-perpendicular flow shear. As with the electrostatic case, the inclusion of finite shear reduces the growth rates at all $k_y$. As the shearing rate is increased from 0.04 to 0.08, the Floquet-averaged growth rates at all $k_y$ increase unexpectedly. At higher shearing rates, the Floquet-averaged growth rates generally fall again, as expected. The unexpected increase in Floquet-averaged growth rates between $\gamma_{E\times B} = 0.04$ and 0.08 is more exaggerated than was observed in the electrostatic case. Furthermore, it cannot be explained by the presence of centrifugal drive terms in the gyrokinetic equation, because such terms are not included in `GS2`. In Appendix D we present a possible explanation for this apparently surprising transient effect from competing modes; this 'transient' effect could become perpetual for beating modes with almost-identical Floquet-averaged growth rates.

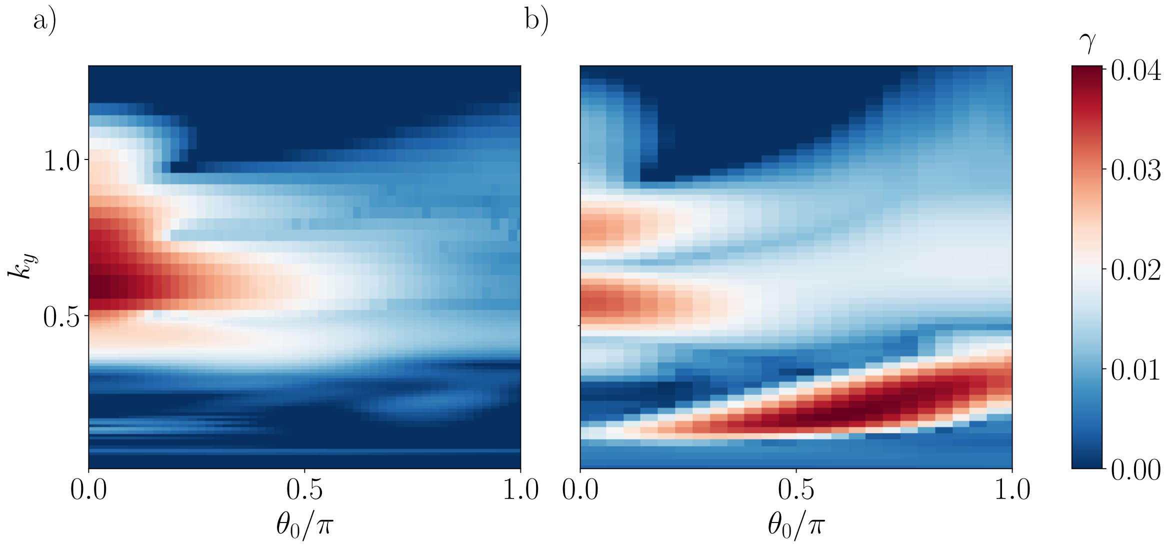

Figure 3.12: Linear growth-rate spectra for equilibrium C with a) no flow shear, b) only the parallel component of flow shear and $\gamma_{E\times B} = 0.04$. Both $\delta A_\parallel$ and $\delta B_\parallel$ fluctuations are included. The $\theta_0$ resolution for a) and b) are $\Delta\theta_0 = 0.06$ and $0.12$, respectively. The $k_y$ resolution for a) is $\Delta k_y = 0.01$ for $k_y \leq 0.5$ and $\Delta k_y = 0.04$ otherwise. For b), $\Delta k_y = 0.02$ everywhere.

We finally focus on the results when both parallel and perpendicular components of flow shear are combined. At low-$k_y$, the perpendicular shear is insufficient to suppress the KBM destabilized by PVG – this grows monotonically as a function of $\gamma_{E\times B}$. To avoid the KBM featuring heavily, we should stick to shearing rates of $\gamma_{E\times B} < 0.08$. In the modified toroidal-ITG branch, we see little difference between the two lowest values of $\gamma_{E\times B}$; beyond that the toroidal and slab branch are clearly stabilized by flow shear. It is difficult to say whether we would expect the transport to be reduced by any change in $\gamma_{E\times B}$ at all at this level of $\beta_D$. We note that the ratio of the parallel and perpendicular components of flow shear scales like $q/\epsilon$, which is approximately 20 in the mid-barrier region of equilibrium C. In contrast, the relative strength of the PVG drive in a spherical tokamak, for which $\epsilon \sim 1$, would be significantly reduced. [113].

#### 3.2.2.2 Magnetic shear

As discussed at the start of this Chapter, small or negative magnetic shear is thought to be important for ITB formation. In this Section, we study the response of equilibrium C to changes in magnetic shear. We performed linear scans around the nominal

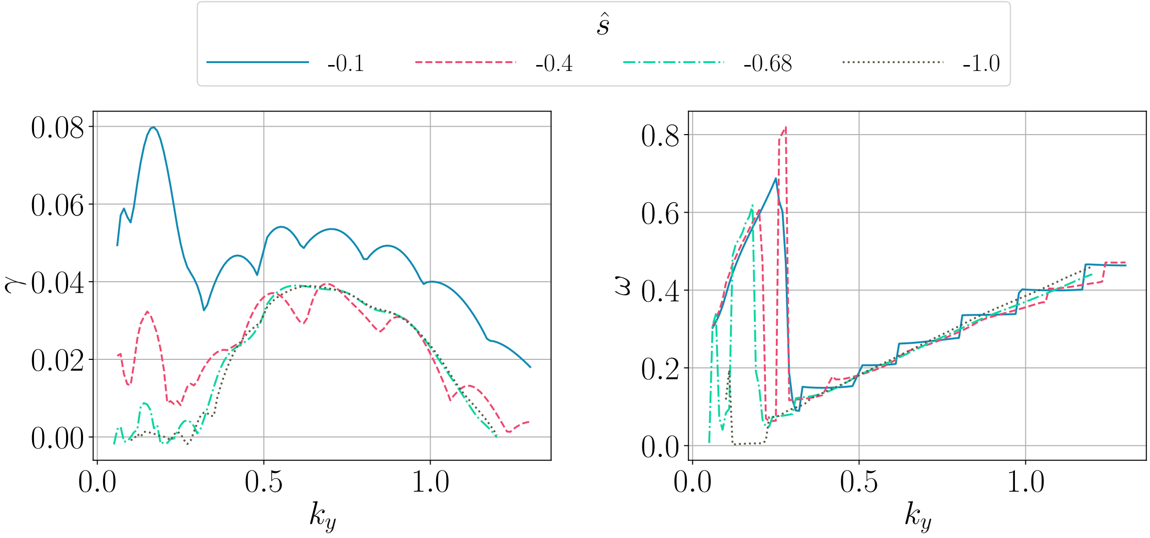

Figure 3.13: Growth-rate and real-frequency spectra for equilibrium C with various values of $\hat{s}$ at $\theta_0 = 0$. Both $\delta A_{\|}$ and $\delta B_{\|}$ fluctuations are included. The $k_y$ resolution is $\Delta k_y = 0.01$.

value of $\hat{s} = -0.68$. Growth-rate and real-frequency spectra are shown in Figure 3.13. An increase in $\hat{s}$ from its nominal value to $-0.4$ and to $-0.1$ increases the prominence of slab-ITG bands. We note that as $|\hat{s}|$ gets smaller, the modes become highly oscillatory in $\theta$, i.e. the $k_{\|}$ of the slab modes increases. The reason for this is not understood. As a result of this, the 32 $\theta$ grid points per $2\pi$ segment was insufficient to resolve well the modes, especially at higher $k_y \simeq 1$. We performed a sensitivity study that suggested that at least 128 $\theta$ grid points per $2\pi$ would be required to properly resolve the modes at $\hat{s} = 0.1$ up to $k_y \simeq 1$. As the parallel resolution was increased, the linear growth rates also increased. Nevertheless, the qualitative behaviour was unchanged with only 32 grid points. Aside from the destabilization of the slab/toroidal ITG modes, we observe that as $\hat{s}$ is increased from $-1$ to $-0.1$, a low-$k_y$ mode is destabilized. We label this mode a KBM as it disappears with the removal of $\delta A_{\|}$ fluctuations and its real frequency is much higher than that of the ITG branches. We note that the KBM mode structure is extended and broad, peaking far along the field line at multiple $\theta - \theta_0$ locations that lie in the bad-curvature region. Examples of the eigenmode structures are shown in Figure 3.14 for $\hat{s} = -0.1$. The splitting of the KBM at $k_y \simeq 0.1$ corresponds to the mode structure shifting to lower $|\theta - \theta_0|$. Increasing $-\hat{s}$ to 1.0 almost

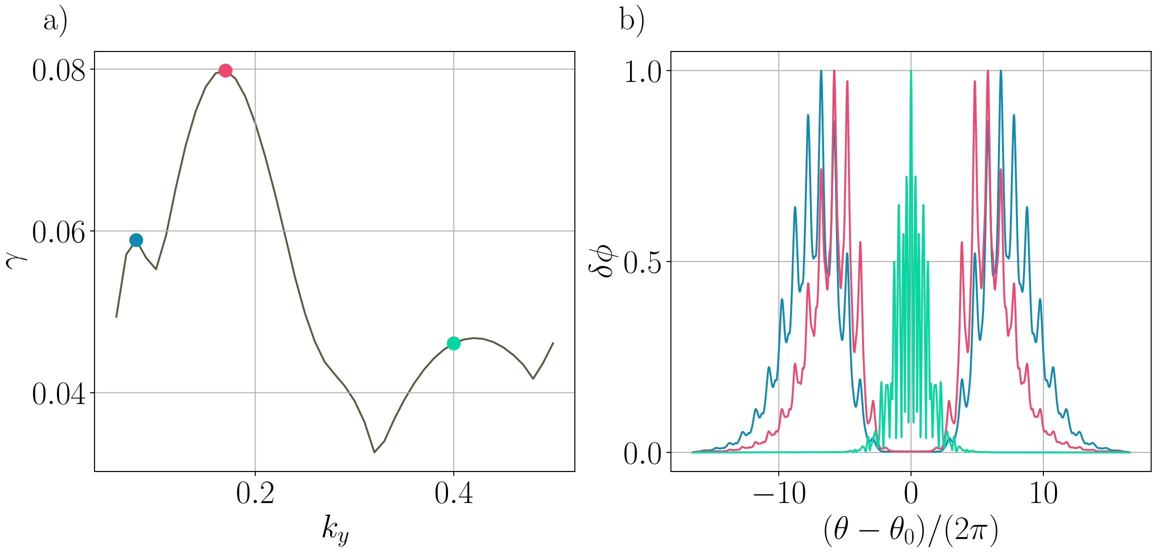

Figure 3.14: a) Growth-rate spectrum and b) eigenmode structures for equilibrium C with $\hat{s} = -0.1$. Both $\delta A_\parallel$ and $\delta B_\parallel$ fluctuations are included. The colours of markers on a) indicate the $k_y$ for the similarly coloured eigenmodes in b).

completely stabilizes the KBM, but has little effect on the slab and toroidal branches of ITG. The key conclusions that can be drawn are that increasingly negative magnetic shear primarily acts to suppress the KBM, whilst providing only modest stabilization of the toroidal and slab branches of ITG.

#### 3.2.2.3 Ion temperature

We study electromagnetic effects by scanning in ion temperature between 0.4 to 1.0, which corresponds to values of $\beta_D$ ranging from 1.57% to 3.93%. The value of $\beta' \equiv \beta(\log p)'$ was changed consistently with $T_i$ by keeping $(\log p)'$ fixed for each species and scaling the ion contributions to $\beta$ linearly with the ion temperature. All of the temperature and density length scales were kept fixed. $T_e$ was similarly kept fixed, so this also constitutes a scan in $T_i/T_e$. Increased $T_i/T_e$ is understood to have a stabilizing effect on the ITG instability [114]. The species collisionalities were not changed in this scan. Growth-rate spectra are shown in Figure 3.15. As $\beta$ increases, the $k_y \simeq 1$ toroidal ITG branch that extends to $\theta_0/\pi \simeq 0.25$ is stabilized, as expected. The slab ITG modes, distinguished by their extent in $\theta_0$, are stabilized less aggressively than the toroidal branch. At sufficiently high $T_i$, a KBM is destabilized at low $k_y$ across a broad

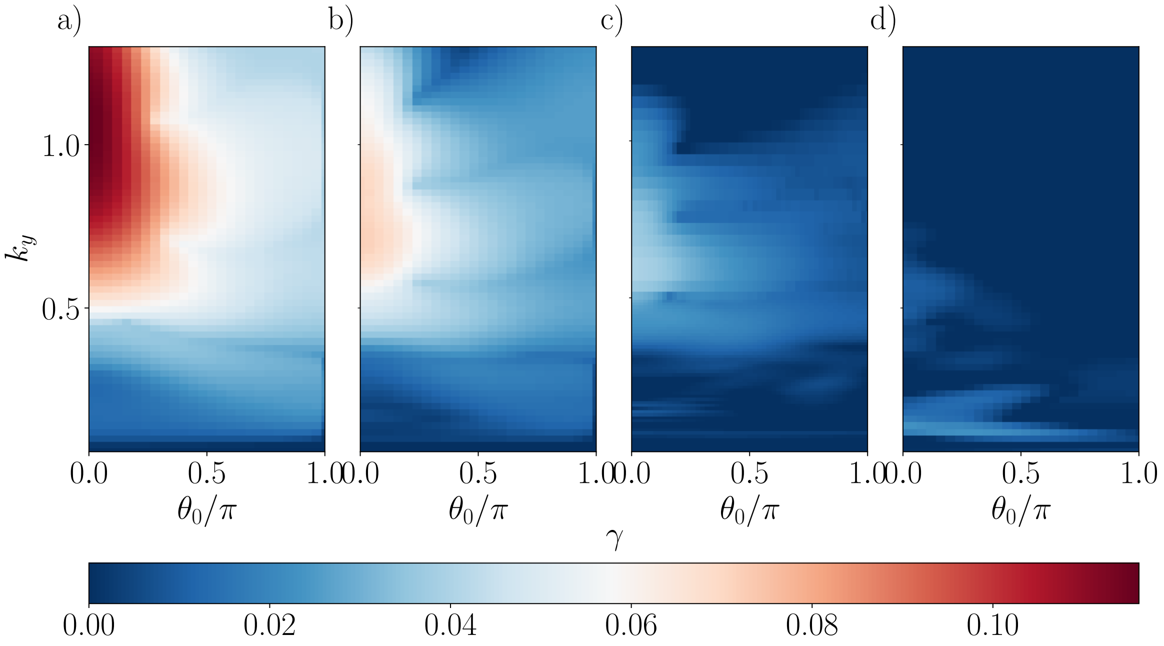

Figure 3.15: Growth-rate spectra for equilibrium C as the ion temperature is switched between a) 0.4, b) 0.6, c) 0.79 (nominal) and d) 1.0. Both $\delta A_\parallel$ and $\delta B_\parallel$ fluctuations are included. $\beta'$ is changed consistently with $T_i$. The $\theta_0$ resolution is $\Delta\theta_0 = 0.12$ and $\Delta k_y = 0.02$, except for the nominal case whose resolutions are as above.

range of $\theta_0$, peaking at finite $\theta - \theta_0$. Compared to a typical $\beta$ scan as shown in Figure 2.9a) in which the stabilization of the ITG is followed by aggressive destabilization of a KBM, the electromagnetic mode destabilized at $T_i = 1$ here is relatively weak. Further increases of $T_i$ to 1.2 and 1.4, not shown, only slightly destabilize the KBM. This may indicate access to the KBM second-stability region; this is aided by increased $-\beta'$, which was changed consistently with $T_i$.

#### 3.2.2.4 Ion temperature gradient

The $\alpha_{\mathrm{MHD}}$ parameter, which scales with the normalized pressure gradient, is known to stabilize microinstabilities via its effect on local magnetic shear. An attractive scenario for ITB formation is one in which an increase in driving gradients decreases the local magnetic shear through $\alpha_{\mathrm{MHD}}$, which in turn reduces the transport via stabilizing the driving instabilities. We study this by scanning in $L_{T_i}^{-1}$ for both ion species and changing $\beta'$ consistently. We do not take into account the effect of steeper temperature gradients on the global magnetic shear $\hat{s}$, e.g. via the bootstrap current. Growth-rate spectra

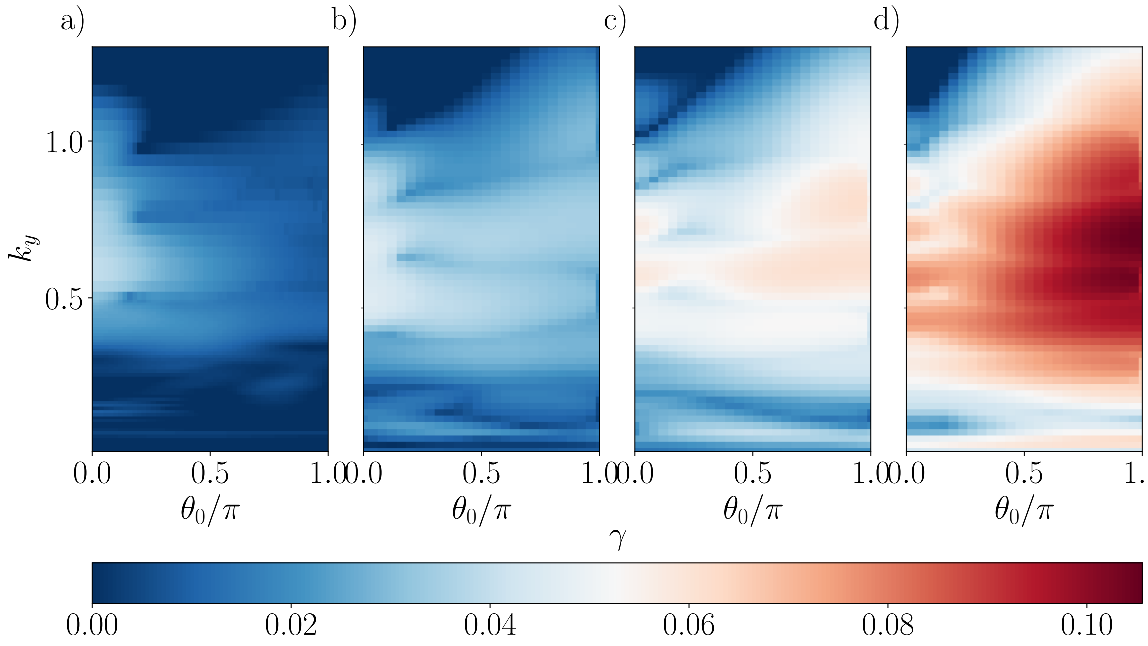

Figure 3.16: Growth-rate spectra for equilibrium C as $L_{T_i}^{-1}$ is switched between a) 7.3 (nominal), b) 9, c) 11 and d) 15. Both $\delta A_\parallel$ and $\delta B_\parallel$ fluctuations are included. $\beta'$ is changed consistently with $L_{T_i}^{-1}$. The $\theta_0$ resolution is $\Delta\theta_0 = 0.12$ and $\Delta k_y = 0.02$, except for the nominal case whose resolutions are as above.

are shown in Figure 3.16. As $L_{T_i}^{-1}$ is increased from 7.3 to 15, growth rates tend to increase at all scales. The slab branch of ITG is destabilized more aggressively than the toroidal branch. We note two plausible reasons for this. As discussed in Appendix C.2, the slab branch scales more aggressively with $L_{T_i}^{-1}$ compared with the toroidal branch. The toroidal branch is also more responsive to the stabilizing effects of magnetic shear, being affected by both drive and FLR damping. As $L_{T_i}^{-1}$ is increased, the slab branch becomes most unstable at $\theta_0 = \pm\pi$. This can be explained by the variation of the Bessel function as $\theta_0$ varies. At $\theta_0 = 0$, $J_0(\alpha_i)$ for this equilibrium is sharply peaked around $\theta - \theta_0 = 0$, which is favourable for the growth of ballooning-type modes that are driven strongly at the outboard midplane[6]. In contrast, slab-ITG modes can be driven anywhere along a field line as long as they are not FLR-damped by magnetic shear. For this equilibrium, the Bessel function at $\theta_0 = \pm\pi$ has a lower maximum value compared to at $\theta_0 = 0$, since $|\boldsymbol{k}_\perp|$ tends to increase with $|\theta_0|$. However, it is

---

[6] The Bessel function $J_0(\alpha_s)$ that appears in Equation 1.21 is a good indicator of the strength of FLR damping – a large Bessel function indicates less damping.

much broader in $\theta - \theta_0$. This property lends itself to stronger growth of the slab-ITG modes closer to $\theta_0 = \pm\pi$. As with the scan in $\hat{s}$, the slab modes at higher $k_y$ oscillate too rapidly along the field along to be captured well by just 32 parallel grid points per $2\pi$ in $\theta$. Nevertheless, the qualitative trends remain unchanged when the parallel resolution is increased by a factor of 4.

### 3.2.3 Nominal transport levels

In this section we present results of nonlinear simulations using `GS2`. The aim of this section is to convince the reader that local gyrokinetic simulations using self consistent equilibria that include the steep driving gradients observed in ITBs can simultaneously predict experimental fluxes in multiple transport channels. The experimental fluxes are given in Table 3.2. To this end, we will present simulations from the mid-barrier using equilibrium C, as it exhibited the maximum linear stability of the three equilibria studied. All of the nonlinear simulations used the same resolution parameters, which are shown in Table 3.3, unless stated otherwise. Exploratory simulations were performed to investigate the maximum required $k_y$ – for equilibrium C, there was little quantitative difference between $k_{y,\max} = 1$ and $k_{y,\max} = 2$, suggesting sufficient resolution in that regard. As with Chapter 2, we performed sensitivity scans to the number of $k_x$ values needed to converge for the nominal equilibrium C parameters. The inclusion of electromagnetic effects and collisions in these simulations increased the computational

Table 3.2: Experimental flux levels calculated using JETTO in the mid-barrier region for the three equilibria. The total momentum flux ($\Pi$) and species-$s$ heat ($Q_s$) and particle ($\Gamma_s$) fluxes are normalized to the gyro-Bohm values defined in Appendix B.

| Parameter | A | B | C |
|---|---|---|---|
| $Q_i(\times 10^{-2})$ | 3.47 | 3.34 | 3.28 |
| $Q_e(\times 10^{-2})$ | 1.93 | 1.36 | 1.29 |
| $\Pi(\times 10^{-2})$ | 7.47 | 6.80 | 6.35 |
| $\Gamma_i(\times 10^{-2})$ | 1.04 | 0.93 | 0.92 |
| $\Gamma_e(\times 10^{-2})$ | 1.02 | 0.93 | 0.91 |

Table 3.3: Resolution parameters for nonlinear simulations in the mid-barrier region.

| Item | Value | Description |
|---|---|---|
| `ntheta` | 32 | Parallel grid points per $2\pi$ domain |
| `negrid` | 16 | Number of energy grid points |
| $2 \cdot$ `ngauss` | 10 | Number of passing pitch angles per sign of $v_\parallel$ |
| `vcut` | 3 | Ratio of $v$ to $v_{\mathrm{th},s}$ above which $h_s = 0$ is forced |
| $\Delta k_y$ | 0.048 | Grid spacing in $k_y$ |
| $k_{y,\max}$ | 1.0 | Maximum $k_y$ |
| $2\pi\hat{s}\Delta k_y/\Delta k_x$ | 4 | Sets $k_x$ grid spacing |
| $N_{k_x}$ | 256 | Number of $k_x$ values |

cost significantly, so care was taken to adequately resolve the physics whilst remaining within the allocated computational budget.

We first present electrostatic results with and without flow shear; time traces of the various flux channels are shown in Figure 3.17. These simulations were initialized with low-level ($\phi \sim 10^{-3}$) noise. Regardless of whether flow shear is included, the heat fluxes predicted from simulation are far higher than experiment. In particular the ion heat fluxes are around 40 times larger than experiment. The addition of flow shear has little effect on the heat and particle transport levels. This is consistent with the linear-growth-rate trends observed in Figure 3.10. The momentum flux is also well above the experimental level.

With the failure of electrostatic simulations to match experimental fluxes, we turn our attention to electromagnetic simulations. The linear studies suggested that magnetic fluctuations provide significant stabilization, and nonlinear simulations have previously been observed to have enhanced stability with the inclusion of EM effects [47]. Nonlinear electromagnetic simulations are known to be challenging for a variety of reasons. One of these is that the time step can become prohibitively small with the inclusion of the $v_\parallel \delta A_\parallel / c$ term that appears in the gyrokinetic potential and represents streaming along perturbed field lines. To explain this, we note that the nonlinear term

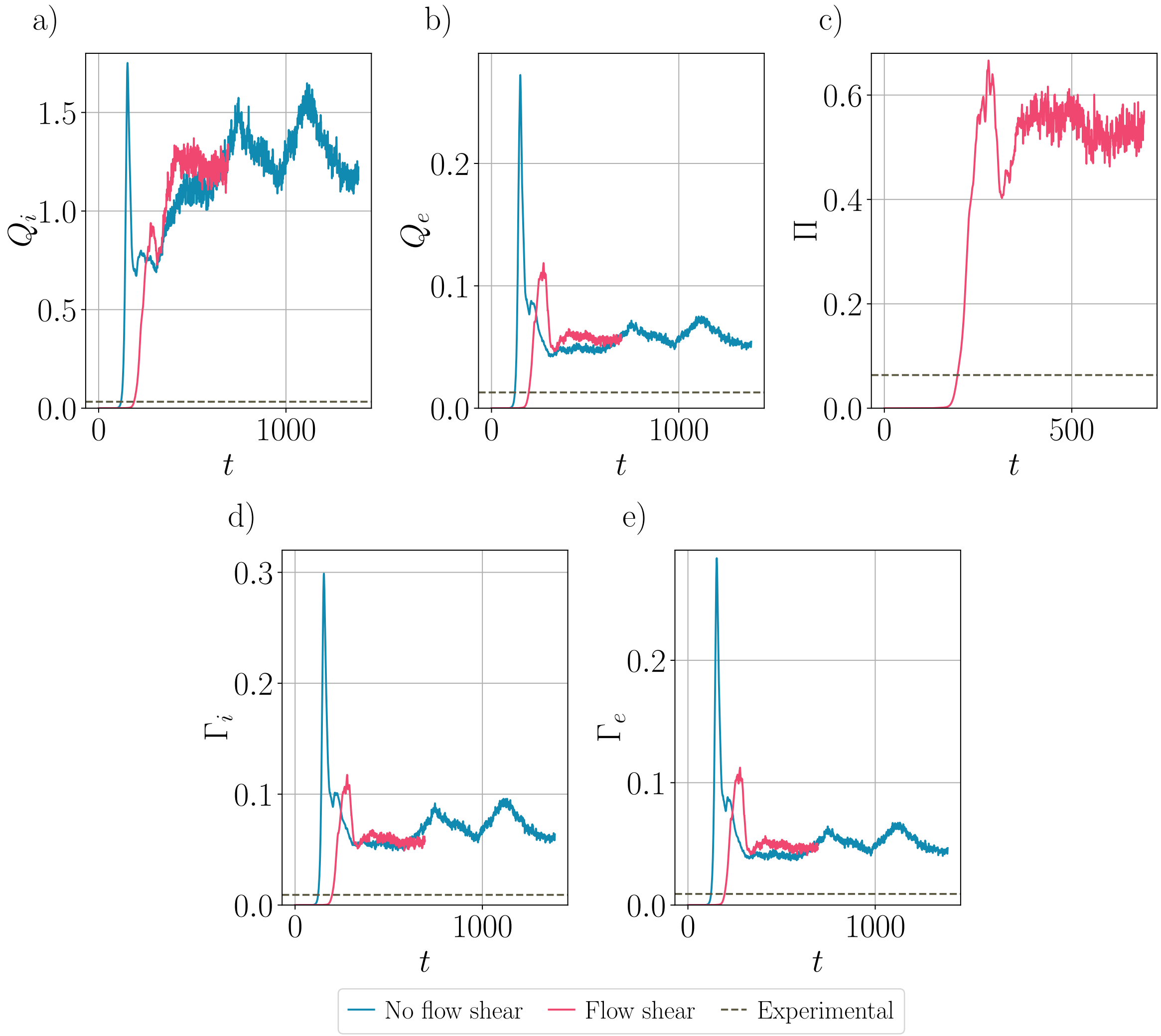

Figure 3.17: Time traces of a) total ion heat flux, b) electron heat flux, c) total momentum flux, d) total ion particle flux and e) electron particle flux for a set of electrostatic simulations. Experimental flux levels are shown by the dashed lines. The ion heat flux is dominated by the contribution from deuterium, which is two orders of magnitude higher than that of carbon.

in `GS2` is treated explicitly. This requires that the time step size must not exceed the Courant-Friedrichs-Lewy (CFL) constraint in order to avoid numerical instability from information propagating through the spatial grid in an unphysical way [115]. The linear part of the equation, which is evolved using an implicit time-stepping algorithm, is not constrained by the CFL condition. When $\delta A_{\|}$ fluctuations are included, the nonlinear term acquires a contribution to the gyrokinetic potential from $v_{\|}\delta A_{\|}$. The electrons stream rapidly along field lines at $v_{\|} \sim v_{\mathrm{th},e}$, so the nonlinear term can be dominated by the $v_{\|}\delta A_{\|}$ term, despite $\delta A_{\|}$ often not being the dominant field. This can reduce the CFL time step to be smaller than in electrostatic simulations, even if $\delta\phi$ is smaller with the inclusion of magnetic fluctuations. This CFL constraint, combined with the fact that the coupled system of equations triples in size with the addition of the parallel and perpendicular current equations, makes nonlinear electromagnetic simulations computationally expensive.

Numerical observations also indicate that above a threshold $\beta$ many fully electromagnetic simulations either do not appear to saturate, or at least become prohibitively computationally expensive to run [116, 44]. With CBC equilibrium parameters, the non-saturation threshold $\beta$ is approximately 0.8%, which is well-below the $\beta \simeq 1.2\%$ at which the KBM is destabilized. Some suggest that the origin of this non-saturation is down to computational expense; both larger and finer simulation domains are required as $\beta$ increases [116]. Others propose a physical origin, such as the nonzonal transition (NZT) [117, 118]. The NZT is posited to occur above a critical value of $\beta$, where sufficiently large fluctuations in the radial magnetic field can break up magnetic flux surfaces, increasing magnetic stochasticity [119]. This results in radial currents that short out structures such as the zonal flows that saturate ITG turbulence. With this reduced zonal flow activity, the ITG (or other dominant instability) can continue to grow and drive strong transport until another saturation mechanism is activated.

Despite these challenges, our `GS2` simulations produce a saturated state for equilibrium C with the addition of $\delta A_{\|}$ and $\delta B_{\|}$ fluctuations. In Figure 3.18, we show a time trace of the different ion and electron heat and particle fluxes without flow shear. This simulation was initialized from the saturated state of a nearby, self-consistent equilibrium with a slightly different density profile fitted[7]. That saturated state, in turn, was initialized with low amplitude noise as in the electrostatic simulations above. The turbulence appears to saturate at around $t = 1000$, with electron heat fluxes and both ion and electron particle fluxes closely matching to experiment. Different transport 'channels' correspond to the different field components of the radial drift $\boldsymbol{V}_\chi \equiv cB^{-1}\boldsymbol{b} \times \nabla\chi$, where $\chi$ contains the fluctuating electromagnetic fields. The majority of the ion heat flux, which saturates approximately 3 times too high at $Q_i \simeq 0.1$, comes from the electrostatic channel. The electron heat flux is also predominantly from the electrostatic component, but a significant amount also comes from the field-line bending component ($\delta A_\parallel$). The addition of electromagnetic effects provides a reduction in the turbulent transport of an order of magnitude, primarily in the ion-transport channel. Notably, we did not encounter particular difficulties when simulating this system with finite-$\beta$ effects included, other than the expected increased computation cost. Figure 3.19 shows the energy spectra as a function of $k_y$ for the three electromagnetic fields present in this simulation.

Using the first half of the simulation presented above as an initial condition, we then added equilibrium-flow-shear effects. We present time-traces of heat, momentum and particle fluxes in Figure 3.20, whilst energy spectra are presented in Figure 3.21. From $t = 1130$ to 1370, both parallel and perpendicular components of flow-shear were included. From the initial state, the fluxes initially jump up significantly, before relaxing to a level where $Q_i \simeq 0.17$, $Q_e \simeq 0.08$, $\Pi \simeq 0.15$ and $\Gamma_i \simeq \Gamma_e \simeq 0.03$. All of the fluxes increase, are higher than experiment, and become highly oscillatory in comparison to the behaviour without flow shear. This increase in transport, particularly via the $\delta A_\parallel$ contribution to the electron heat flux, is consistent with the linear results of Figure 3.20c) where the KBM is destabilized at low-$k_y$ with increasing $\gamma_{E\times B}$. These results suggest that the nominal (for equilibrium C) level of flow shear is not consistent with the experimental observations. One might expect that the shearing rate should be

---

[7] This initial condition was used because previous exploratory simulations had been performed with this equilibrium before equilibrium C was simulated. We have not tested whether there is sensitivity to the initial condition.

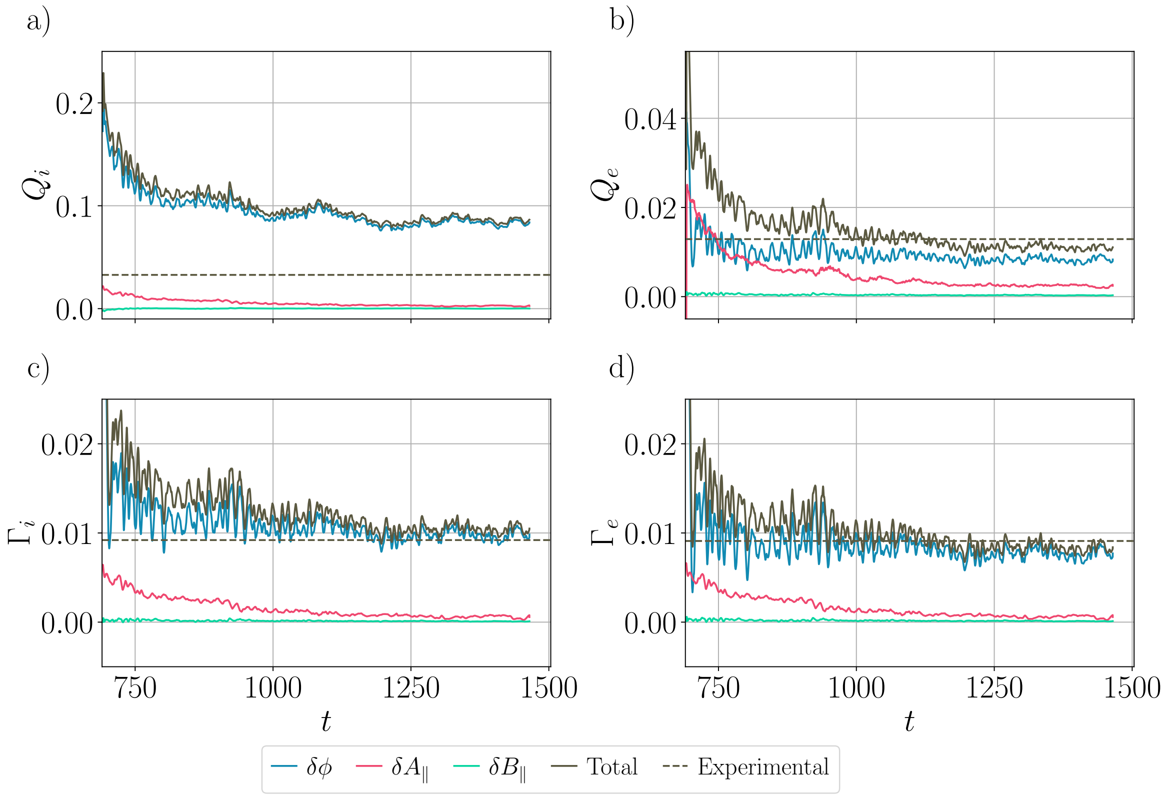

Figure 3.18: Time traces of a) ion heat flux, b) electron heat flux, c) ion particle flux and d) electron particle flux for fully electromagnetic simulations without equilibrium flow shear. Different transport channels, corresponding to different fluctuating fields, are shown in different colours. Experimental flux levels are shown by the dashed lines.

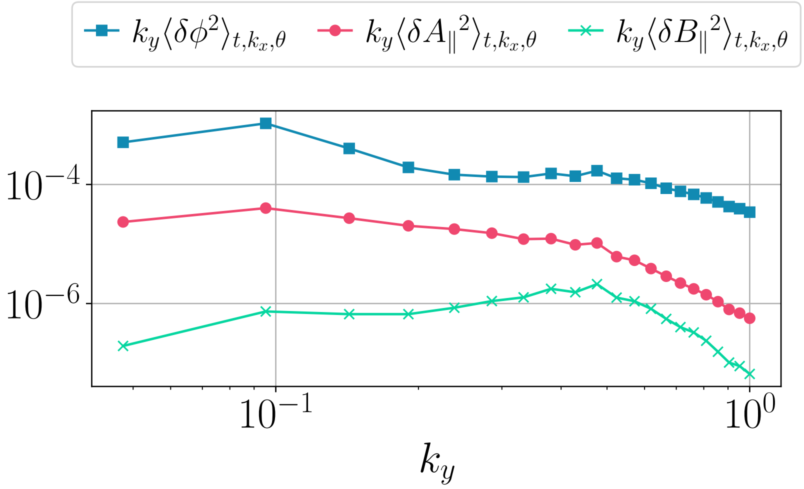

Figure 3.19: Energy spectra for equilibrium C, averaged over $t > 1200$ and $|k_x| < 1.5$. Different colours correspond to different electromagnetic fields.

decreased to bring all of the fluxes down and closer to experimental levels. This will be confirmed by results given in the next Section.

As noted in Section 3.2.2.1, the linear stability decreases when increasing $\gamma_{E\times B}$ to 0.08 when the parallel component of flow-shear is neglected. We tested this unexpected result to see whether a similar trend is observed in transport levels. To this end, we disable the parallel component of velocity shear for $t \gtrsim 1370$. The transport levels initially drop rapidly, before recovering and growing to some of the highest levels observed in the entire simulation. It was deemed computationally uneconomical to continue the simulation beyond the point shown since the time step size was prohibitively small – a single restart advanced $t$ by just 42 normalized units. A saturated state was therefore not reached, although we cannot say with certainty that saturation is a hopeless endeavour. Several features of the transition between self-consistent and purely-perpendicular flow-shear indicate a qualitative difference between the nature of turbulence between the two states. Perhaps the most obvious is the extreme nature of the transition itself – every flux channel drops close to zero before recovering. This is indicative of a significant re-structuring of the turbulence. Both the sign-change in the momentum flux and the less-oscillatory nature of the turbulence are also indicators of a qualitative difference between the two states. The fact that the linear stability trend is observed also in the overall transport levels may have implications for real fusion devices, although we cannot yet say whether the destabilization via purely-perpendicular flow shear might work in tandem with the destabilizing effect of the PVG. If not, then this effect would be unimportant in a real system, as we do not expect purely perpendicular flow shear, which would require $q \sim \rho^*$ [21], to exist in conventional tokamaks[8]. Such a small safety factor would breach the external-kink MHD stability limit [120, 121] and lead to a rapid loss of confinement. Nevertheless, this is an interesting result that warrants further study of the possible (de)stabilizing effect of equilibrium flow shear.

---

[8] In spherical tokamaks, the local safety factor can be small on the outboard side, so this effect could have more relevance there.

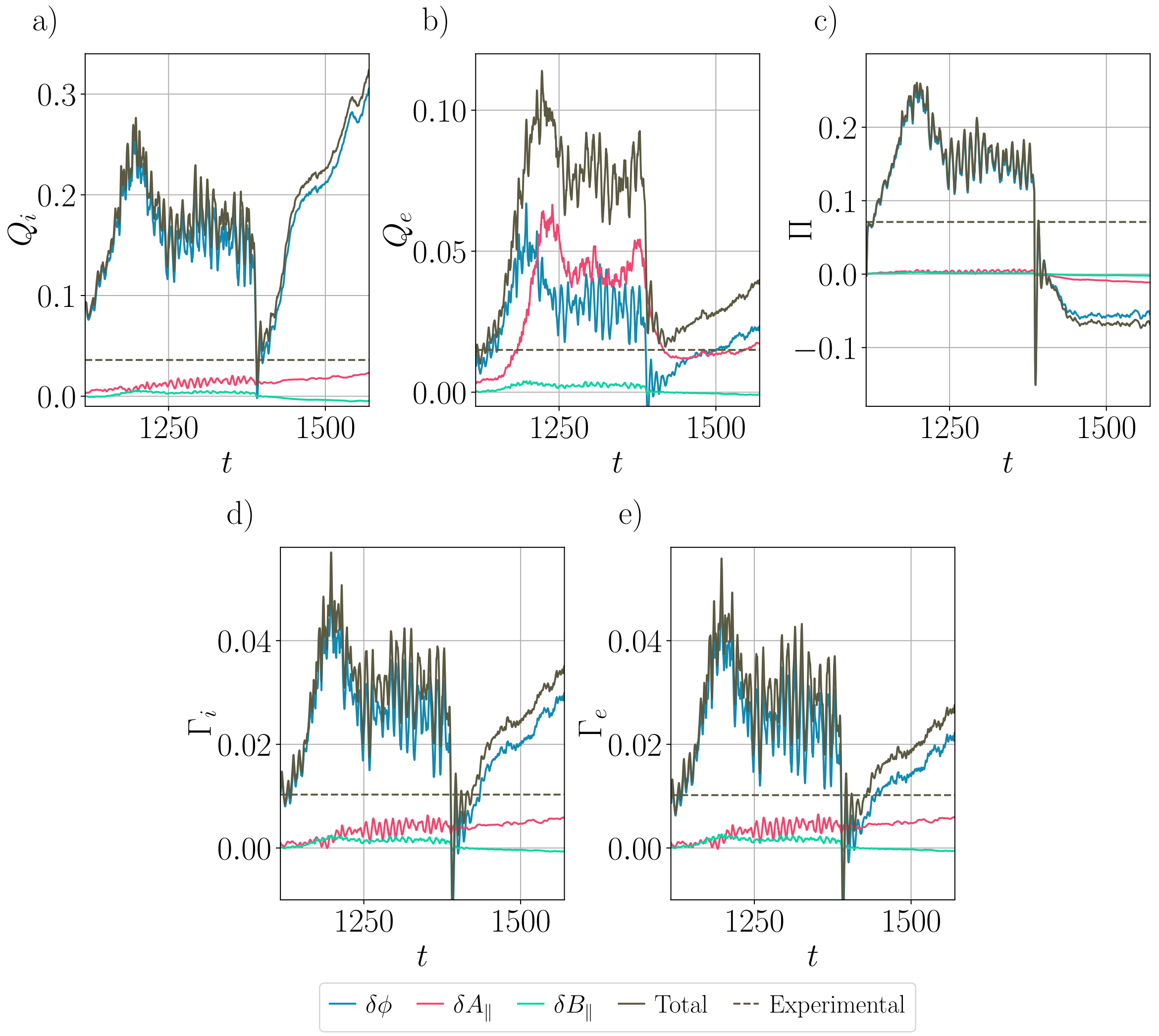

Figure 3.20: Time traces of a) ion heat flux, b) electron heat flux, c) species-summed momentum flux, d) ion particle flux and e) electron particle flux, with fully electromagnetic fluctuations and flow shear. Different transport channels are shown in different colours, and experimental flux levels are shown by the dashed lines. Both parallel and perpendicular flow shear are included for $1130 < t < 1370$, whilst only perpendicular flow shear is included for $t > 1370$.

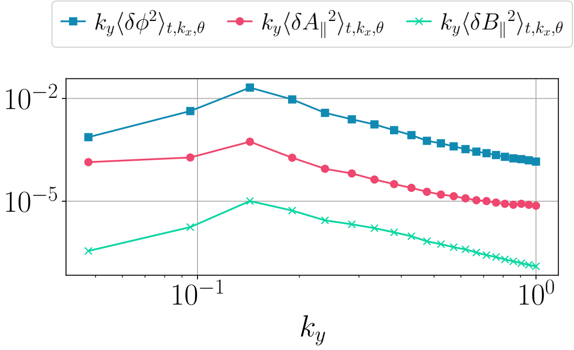

Figure 3.21: Energy spectra for equilibrium C with both parallel and perpendicular components flow shear enabled, averaged over $1250 < t < 1370$ and $|k_x| < 1.5$. Different colours correspond to different electromagnetic fields.

### 3.2.4 Nonlinear parameter scans

In the next Section, we present a variety of one-dimensional scans in the parameters shown to have a significant impact on the linear stability in Section 3.2.2. In doing so, we aim to determine how one might need to change the equilibrium parameters in order to match experimental fluxes in multiple channels simultaneously. We carried out parameter scans in $\gamma_{E\times B}$, $\hat{s}$, $T_i$ and $L_{T_i}^{-1}$, with fully electromagnetic fluctuations considered. The non-$\gamma_{E\times B}$ scans were performed without the inclusion of equilibrium flow-shear effects in order to isolate the effects of changing each parameter. For a proper comparison with experimental results, a realistic level of flow shear should be included in all simulations. This was not done for the scans in $T_i$, $L_{T_i}^{-1}$ and $\hat{s}$, so they should not be used for full comparisons with experiment.

#### 3.2.4.1 Flow shear

We present first the results of a scan in $\gamma_{E\times B}$. The fluxes across all transport channels are shown in Figure 3.22 as a function of $\gamma_{E\times B}$. We note that the $\gamma_{E\times B} = 0.12$ case may not be in a fully saturated state because the simulation cost became too high with the decreasing time step. We expect the saturated flux levels to be slightly lower than reported because at smaller shearing rates, the fluxes transiently increased above their saturated level. Nevertheless, the trends in the transient behaviour indicate that it should still saturate at a higher level than the smaller shearing rates. The inclusion

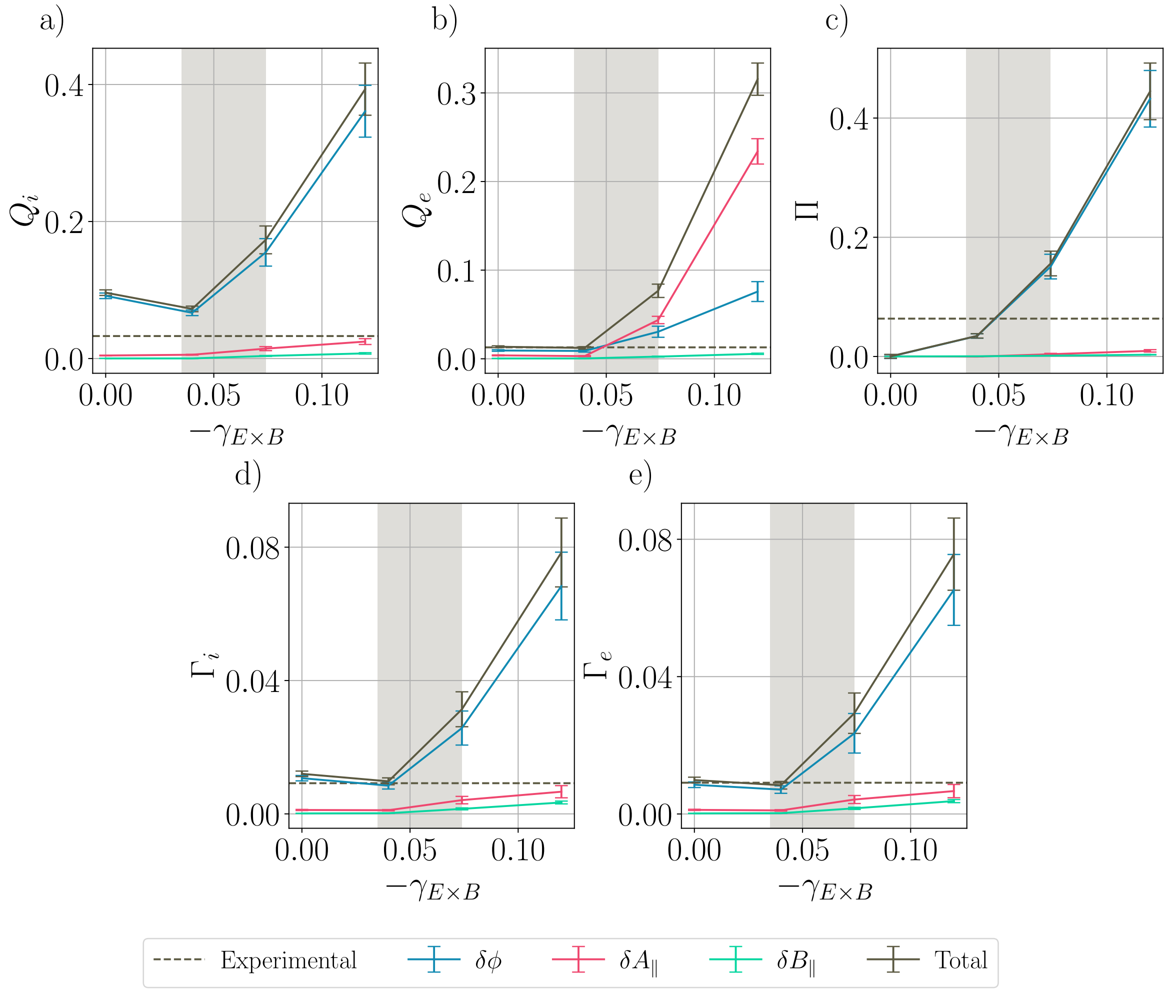

Figure 3.22: A scan in $\gamma_{E\times B}$ showing total and constituent contributions to the a) ion heat flux, b) electron heat flux, c) total momentum flux, d) ion particle flux and e) electron particle flux. The grey dashed line shows the experimental level. The error bars show the standard deviation around the time-averaged value. The shaded regions show the range of $\gamma_{E\times B}$ that is bounded by different fits to the experimental toroidal velocity profile at $r = 0.27$. Since the $\gamma_{E\times B}$ profile of equilibrium C is fitted to be as broad as possible within experimental bounds, the nominal values are on the upper limit of the shaded region. Narrower fits to the toroidal flow profile result in lower shearing rates at this radius.

of finite flow shear up to $\gamma_{E\times B} = 0.04$ leads to a reduction of fluxes in all channels other than momentum flux, which is a monotonically increasing function of $\gamma_{E\times B}$. Above $\gamma_{E\times B} = 0.04$, the heat and particle fluxes increase monotonically for both ions and electrons. The $\delta A_{\|}$ electromagnetic contribution to the electron heat flux becomes increasingly dominant as $\gamma_{E\times B}$ increases, which is again consistent with the linear result that at low-$k_y$, an EM mode is rapidly destabilized as the PVG strength increases. The results confirm that if any flux channels are to be matched to experiment, the shearing rate must be smaller than the fitted value for equilibrium C. A rough estimate for the value of toroidal flow shearing rate that minimizes the deviation from experimental flux levels is $\gamma_{E\times B} \simeq 0.05$. We can conclude from this scan that significant levels of equilibrium flow shear are not compatible with low transport in the high-$\beta$, high-pressure-gradient conditions of the mid-barrier.

#### 3.2.4.2 Ion temperature

A scan in $T_i$ for the two ion species is shown in Figure 3.23. As with the linear simulations presented in Section 3.2.2, increasing $T_i$ (and not $T_e$) affects $\beta_D$, $\alpha_{\mathrm{MHD}}$ and $T_i/T_e$, but the species collisionalities were not changed. We observe monotonic decrease in all flux channels as $\beta$ is increased. This reflects the linear stability trends observed in Figure 3.15. This scan fails to predict a simultaneous unification of the experimental fluxes at any value of $T_i$: increasing $T_i$ above nominal values brings the ion heat flux to experimental levels, but under-predicts the electron heat flux and particle fluxes. We included a value of $T_i = 1.15$ in this scan, despite this being far from consistent with the experimental measurements. This was done to test the response of the transport to the low-$k_y$ EM modes observed in the linear simulations. Those EM modes were relatively insensitive to changes in $\beta$, and had a growth rate of just 0.03 even at $\beta = 1.4$. As such, it is perhaps unsurprising that the heat flux is increasingly stabilized by increasing $T_i$. The heat flux is very sensitive to a reduction of $T_i$ (and therefore $\beta$) from its nominal value to 0.7. This result further supports the observation that electromagnetic effects are critical for sustaining this transport barrier in JET. The fact that increasing $T_i$ to

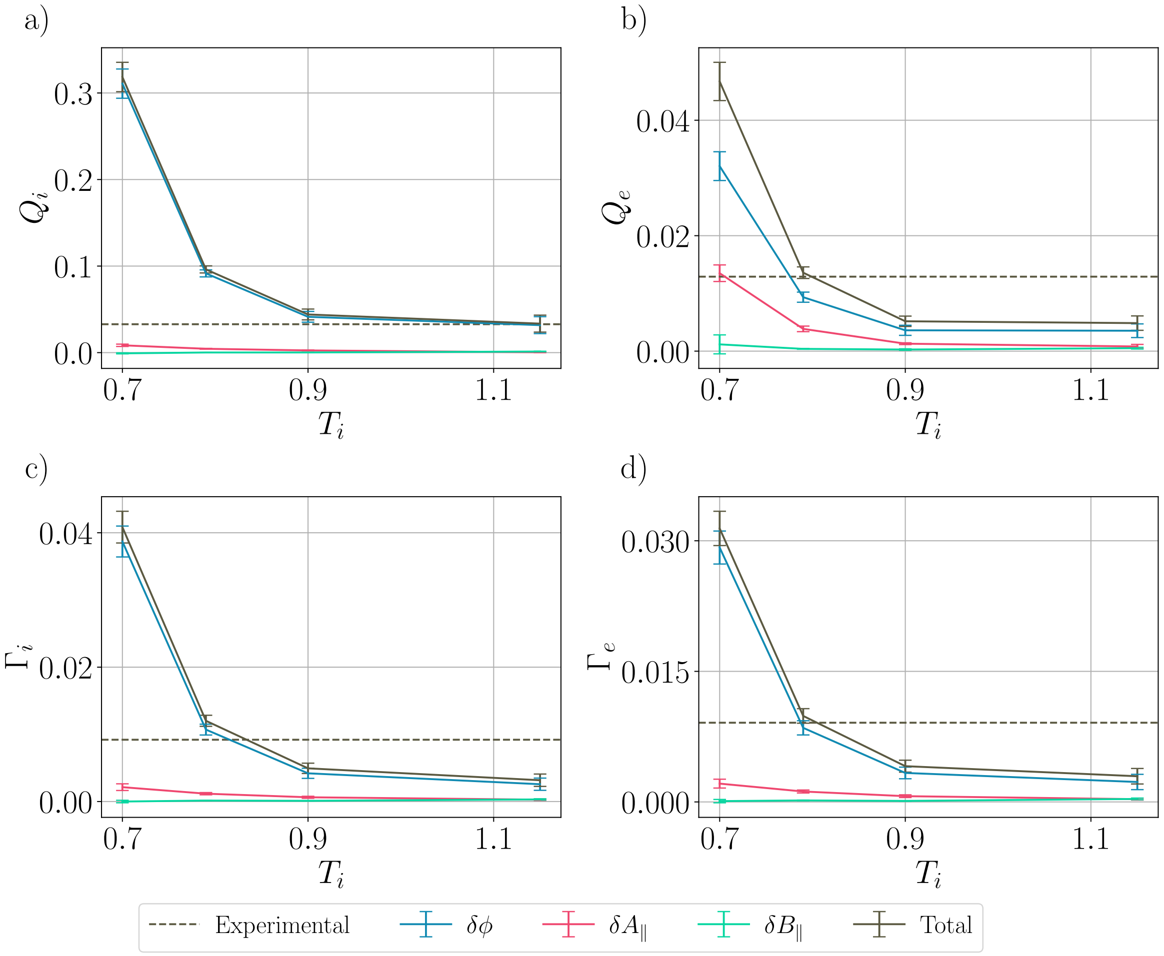

Figure 3.23: A scan in $T_i$ showing total and constituent contributions to a) the ion heat flux and b) the electron heat flux. The grey dashed line shows the experimental level. The error bars show the standard deviation around the time-averaged value. The nominal value of $T_i$ is 0.79.

1.15 continues to reduce the transport also suggests that the triggering of turbulence-enhancing KBMs may be avoided even at higher core pressures that would improve plasma performance further.

We would also like to comment on a possible mechanism for the saturation of the transport barrier – i.e. what process acts to limit the barrier height. The simulations suggest that even moderate increases in $\beta$ at otherwise-fixed equilibrium parameters would be insufficient to trigger barrier saturation. This is not to say that the onset of a virulent (possibly electromagnetic) mode does not lead to a deterioration of confinement at the top of the barrier. Rather, the mechanism that stabilizes such a mode is not rapidly removed by increasing $\beta$ alone within the range we have considered.

#### 3.2.4.3 Magnetic shear

We scanned in $\hat{s}$ from $-0.2$ to $-1.0$ without equilibrium flow shear. The species heat and particle fluxes associated with the three fluctuating electromagnetic fields are shown in Figure 3.24. As $-\hat{s}$ is decreased from its nominal value to 0.2, both ion and electron fluxes increase well above experimental levels. One notable feature of this increase is that the magnetic contribution to the fluxes (in particular from $\delta A_{\|}$) becomes significant to the extent that the electron heat flux is dominated by the contribution from $\delta A_{\|}$. The flux contribution is predominantly from $k_y \lesssim 0.3$ and is broad in $k_x$, extending to $k_x \simeq \pm 1$. Both the significant magnetic contribution to the heat fluxes and the shift in $k_y$ of the dominant flux contribution suggest that the low-$k_y$ electromagnetic instability shown in Figure 3.13, which is destabilized by increased magnetic shear, is the dominant driver of heat flux. The linear simulation results also imply that $\hat{s} = -1$ would have reduced transport compared with the nominal equilibrium due to the increased stability at low $k_y$. However, the heat flux increases in all channels as $-\hat{s}$ is increased from its nominal value to 1.0.

We turn our attention to the role of the zonal flow (ZF) in providing a saturation mechanism for the turbulence, and note that its structure (in $k_x$) changes qualitatively as $\hat{s}$ is varied. This is shown in Figure 3.25, which compares the non-zonal $\{k_x, k_y\}$

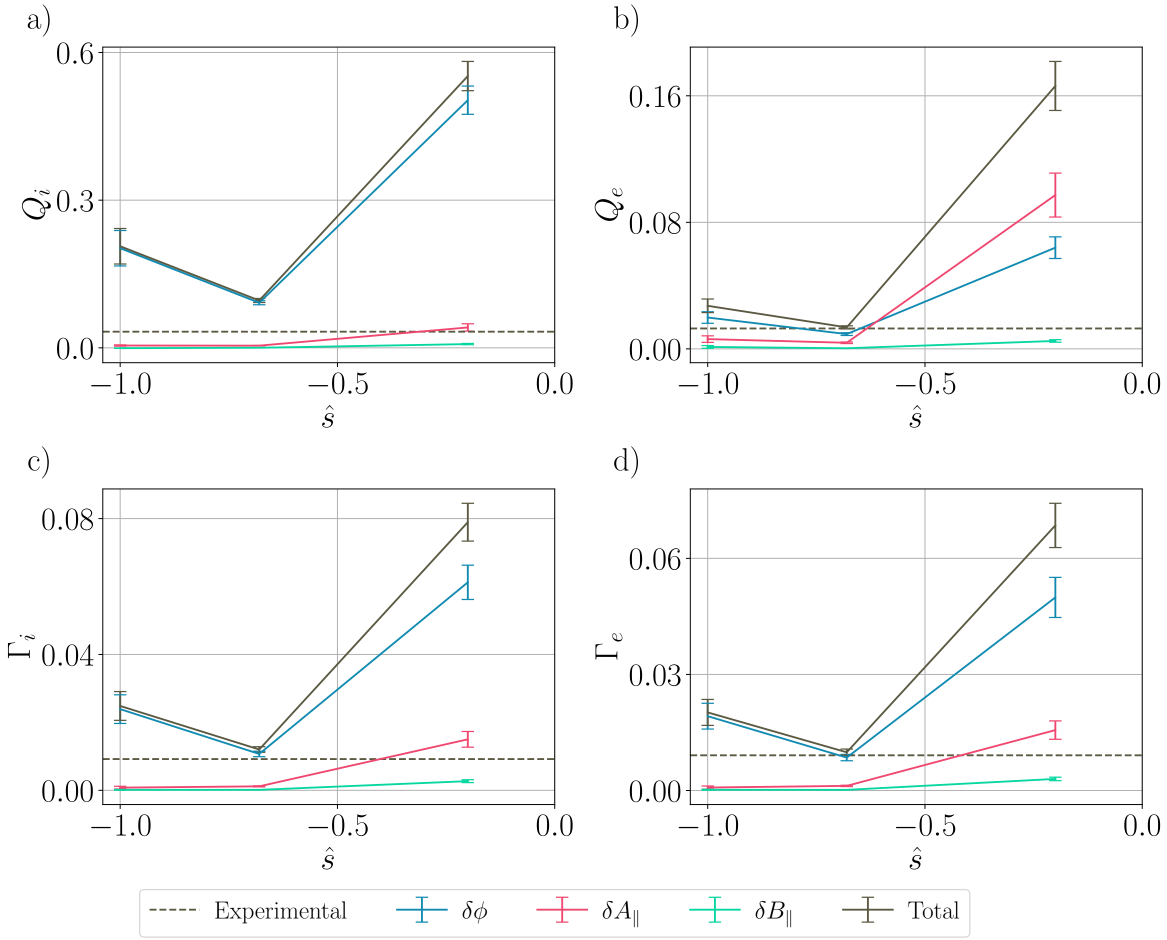

Figure 3.24: A scan in $\hat{s}$ showing total and constituent contributions to the a) ion heat flux, b) electron heat flux, c) ion particle flux and d) electron particle flux. The grey dashed line shows the experimental level. Error bars show the standard deviation around the time-averaged value. The nominal value of $\hat{s}$ is $-0.68$.

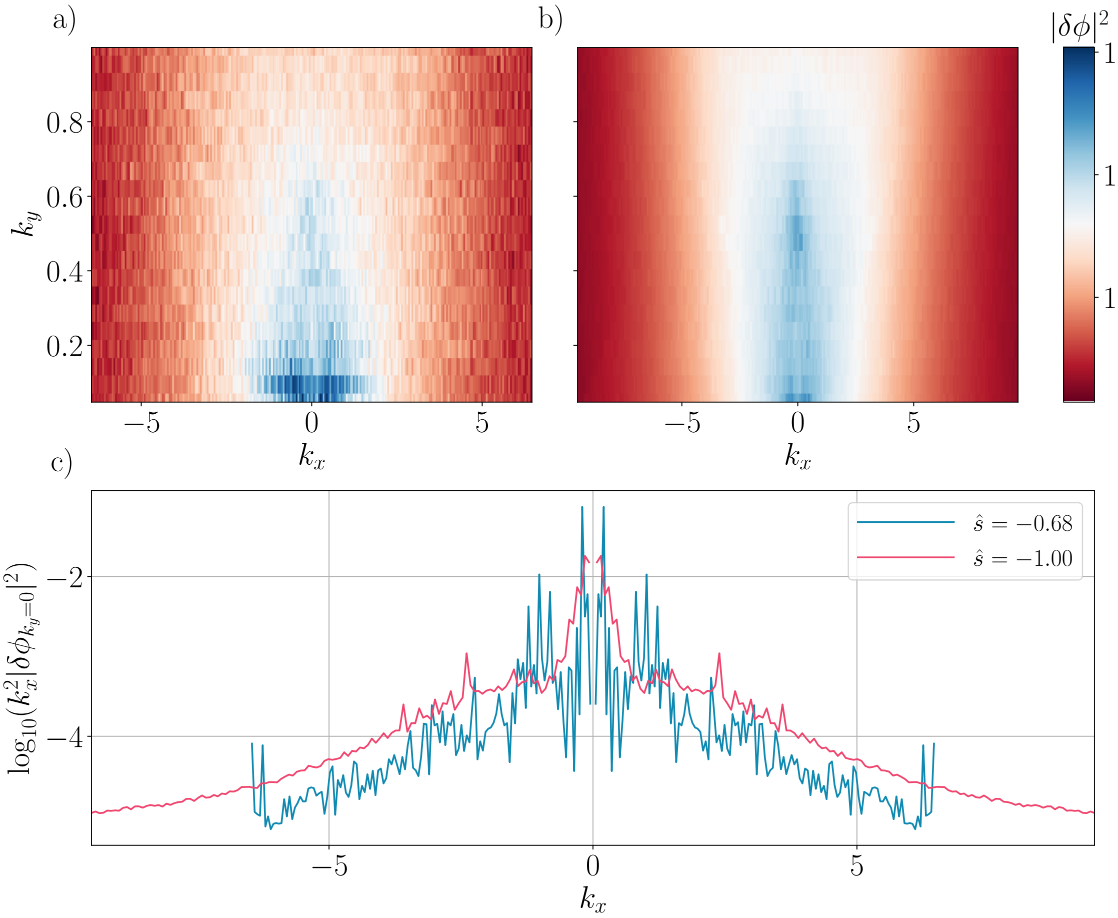

Figure 3.25: Non-zonal $\{k_x, k_y\}$ contributions to the potential for a) $\hat{s} = -0.68$ and b) $\hat{s} = -1$, and c) the zonal flow structure in $k_x$.

components of $\delta\phi$ and its corresponding zonal flow for two values of $\hat{s}$. All other simulation parameters were held fixed as $\hat{s}$ was changed, so $\Delta k_x$ increased by a factor of almost 50% as $|\hat{s}|$ was increased. This means that the $\hat{s} = -1.0$ simulation has worse resolution (due to the increased $\Delta k_x$) than the one with nominal $\hat{s}$. Additionally, since the number of $k_x$ values simulated was fixed, $k_{x,\max}$ was higher for the $\hat{s} = 1$ simulation. This is unlikely to have had an effect since both zonal and non-zonal mode amplitudes are orders of magnitude smaller at the highest $k_x$ values in the simulation, compared with modes at smaller $k_x$. Nevertheless, future investigations could simulate the same $k_{x,\max}$ to check this. We note that at the nominal value of $\hat{s}$, the ZF spectrum is more oscillatory than at $\hat{s} = -1$, and peaks at $k_x = 4\Delta k_x$ compared with $k_x = 2\Delta k_x$ for the $\hat{s} = -1$ case. The nominal-$\hat{s}$ ZF spectrum also features strong zonal flows around $k_x = 1$, which are not present for $\hat{s} = -1$. When $\hat{s}$ is decreased to $-1$, the relative importance of the low-$k_y$ modes decreases, and the spectrum becomes less broad in $k_x$. With the above observations in mind, we suggest a couple of possible explanations for the unexpected behaviour as $\hat{s}$ is decreased. First, we note that the particularly oscillatory nature of the nominal-$\hat{s}$ ZF spectrum requires a fine-enough $k_x$ grid to resolve it. It is possible that by increasing $\Delta k_x$ by 50% this oscillatory structure, which was resolved in the nominal-$\hat{s}$ simulation, could not be resolved in the increased-$|\hat{s}|$ case. We have not performed a simulation with increased $k_x$ resolution to validate this suggestion. An alternative explanation is connected to the qualitative change in the turbulent drive when $\hat{s}$ is changed. At the nominal value of $\hat{s}$, the long-wavelength EM linear instability appears to drive turbulence at low-$k_y$. As discussed in Section 3.2.2.2, decreasing $\hat{s}$ to $-1$ almost entirely stabilizes this linear EM instability. It may be possible that the low-$k_y$ modes couple more strongly to the zonal mode compared with the higher-$k_y$ ones, thereby increasing its stabilizing effect. We note that the linear simulations were only performed for $\theta_0 = 0$, whilst finite $\theta_0$ values are included in the nonlinear simulations. Further investigation is required to understand whether more negative magnetic shear really can increase transport, and if so – how.

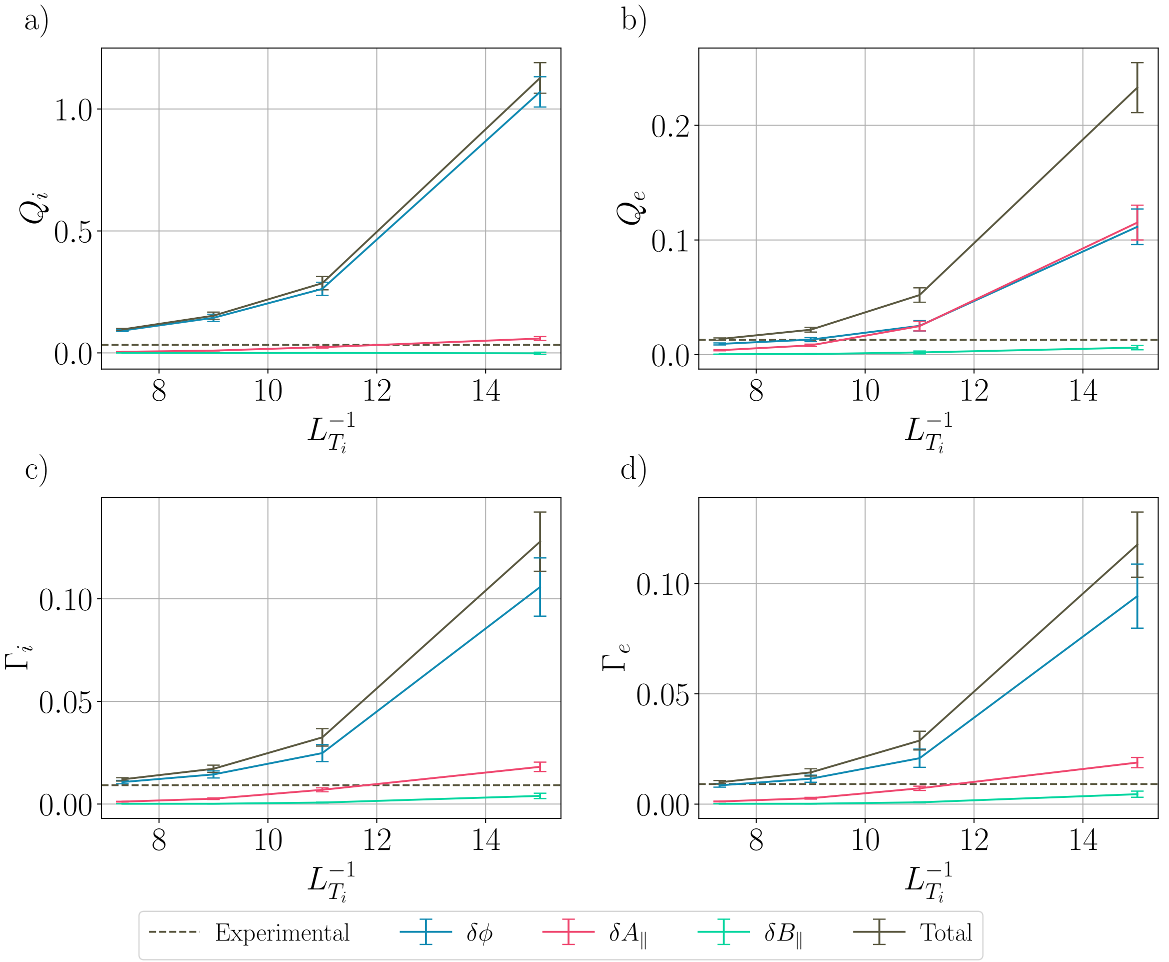

Figure 3.26: A scan in $L_{T_i}^{-1}$ showing total and constituent contributions to a) the ion heat flux and b) the electron heat flux. The grey dashed line shows the experimental level. Error bars show the standard deviation around the time-averaged value. The nominal value of $L_{T_i}^{-1}$ is 7.3.

#### 3.2.4.4 Inverse ion temperature length scale

In Figure 3.16 we show the results of a nonlinear scan in $L_{T_i}^{-1}$ for both ion species where $\beta'$ was changed consistently. As is expected from the linear simulation results, the heat flux increases monotonically with $L_{T_i}^{-1}$ in all flux channels. The ratio of electrostatic to magnetic contributions to the fluxes is relatively insensitive to changes in $L_{T_i}^{-1}$, suggesting that the nature of the turbulent drive does not change qualitatively as $L_{T_i}^{-1}$ is increased with these equilibrium parameters.

### 3.2.5 Possible steps for matching fluxes

Equilibrium C was constructed by varying the magnetic shear, ion density and ion temperature profiles to reduce the linear growth rates. However, there are still some plausible ways that it could be adapted to move the fluxes even closer to experimental levels. Based on the above scans, one of the obvious ways to do this is to re-fit the global toroidal velocity profile to one that is intermediate to equilibria A and C. Adjusting the velocity profile is not expected to significantly affect the other equilibrium parameters such as magnetic shear and temperature gradient.

Although there are a multitude of order-unity changes that could be made to the equilibrium to match the ion heat flux more closely, we have not attempted to optimize further the profiles. We are satisfied that local $\delta f$ gyrokinetics is able to capture the key stabilizing mechanism in the most exotic part of the particular transport barrier studied. This is evidenced by the close matching of experimental fluxes in multiple transport channels for equilibrium C, within experimentally relevant adjustments to the level of equilibrium flow shear. The general picture that we have built up from the studies in the mid-barrier region is that electromagnetic effects are critical for reducing transport by partially stabilizing the toroidal and slab-ITG instabilities that drive the turbulence. The strong negative magnetic shear is important in this part of the barrier for reducing the growth-rate of the virulent electromagnetic instability that is driven unstable at such high $\beta$. Moderate to strong levels of equilibrium flow-shear actually have a destabilizing impact in this high-$\beta$ region of the plasma, as the parallel component of flow shear can destabilize the electromagnetic instability. To reach sufficiently high pressures for electromagnetic stabilization to be important, enhanced confinement is required closer to the wall. This is explored in the next Section, where we study the region outside the foot of the ITB in more detail.

## 3.3 Outside the barrier

In this Section, we study the microstability and transport outside the bottom of the transport barrier, where $r = 0.65$. By matching experimental fluxes at multiple points in the radial profile, we can pin down various equilibrium profiles at these locations. This can constrain profiles in the intermediate regions. One example of this is the toroidal velocity gradient profile. We already saw in the previous Section that $\gamma_{E\times B}$ is expected to be around 0.05 in the mid barrier, which is smaller than the nominal flow shear for equilibrium C. To reduce the shearing rate at the mid-barrier radius, the flow shear profile could be fitted differently. As demonstrated by the toroidal flow profile fitted in equilibrium A, this can be achieved by fitting a narrower profile. By studying the transport in the outer-region we can understand whether fitting a narrower toroidal flow profile increases consistency with experimental fluxes at *multiple* radial locations. The equilibrium parameters at $r = 0.65$ for the three equilibria are shown in Table 3.4. At this radius, the three sets of equilibrium parameters are fairly similar, though the densities and density scale-lengths do differ significantly. This is due to the different fits to the density profiles and $Z_{\text{eff}}$. The most dramatic differences compared with the mid-barrier equilibria are in $\hat{s}$, $\beta'$, $L_{T_i}^{-1}$ and $T_i$. The flow-shear rate is also smaller for all three equilibria at the outer-region. At this radius, electromagnetic effects are expected to be unimportant since the approximate values of $\beta$ for the deuterium and electrons are 0.2% and 0.5%, respectively.

### 3.3.1 Linear stability

We begin by studying the linear stability of the three equilibria without equilibrium flow shear. In Figure 3.27 we show growth-rate spectra for each equilibrium as a function of $k_y$ and $\theta_0$ with and without fully electromagnetic fluctuations. The linear growth rates are broad in $k_y$, peaking between $k_y = 2$ and 3 depending on the equilibrium. The growth rates are sensitive to $\theta_0$, so perpendicular flow-shear is expected to have a strongly stabilizing effect. The dominant instability at all of the scales simulated is the ITG instability. There are no qualitative differences between the three equilibria, but C is the most stable at practically every $\{k_y, \theta_0\}$. As expected, the addition of magnetic fluctuations has little effect on the linear stability; this can be seen by comparing the growth-rate spectra in Figures 3.27d) to f) to the electrostatic results in Figures 3.27a) to c).

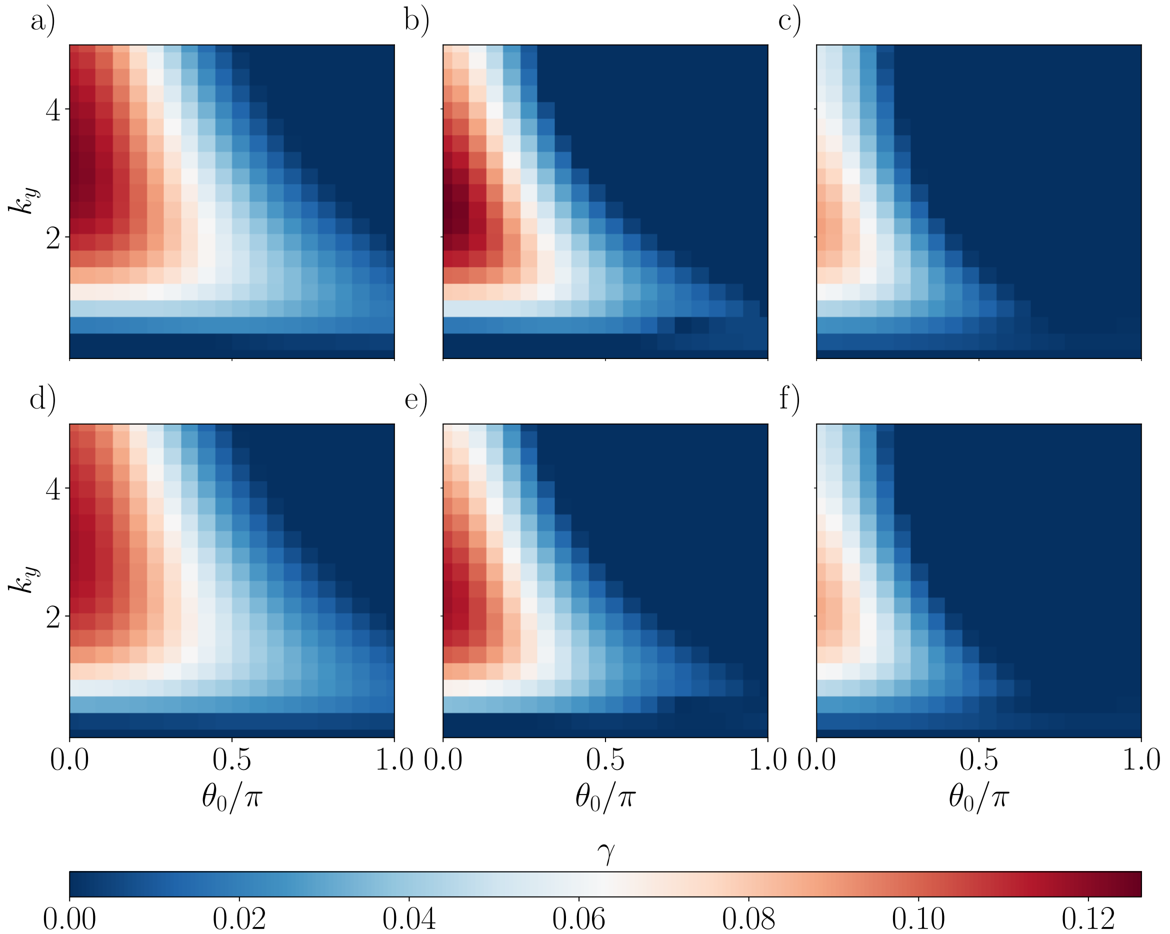

Figure 3.27: Electrostatic (top row) and electromagnetic (bottom row) growth-rate spectra for equilibria A (a and d), B (b and e) and C (c and f).

Table 3.4: Physical parameters for the three equilibria outside the foot of the barrier. As noted in Table 3.1, the contribution to $\beta$ for a given species $s$ can be calculated by multiplying $\beta_{\text{ref}}$ by $T_s$ and $n_s$.

| Parameter | A | B | C |
|---|---|---|---|
| $r$ | 0.65 | 0.65 | 0.65 |
| $R$ | 3.18 | 3.19 | 3.18 |
| $\hat{s}$ | 0.516 | 0.550 | 0.565 |
| $q$ | 2.012 | 2.023 | 2.021 |
| $-R_0'$ | 0.257 | -0.290 | 0.269 |
| $\kappa$ | 1.43 | 1.43 | 1.42 |
| $\kappa'$ | 0.02 | 0.02 | 0.084 |
| $\delta$ | 0.065 | 0.060 | 0.063 |
| $\delta'$ | 0.105 | 0.200 | 0.37 |
| $\beta_{\text{ref}}(\%)$ | 4.77 | 5.04 | 4.87 |
| $-\beta'$ | 0.087 | 0.097 | 0.081 |
| $\gamma_{E\times B}$ | 0.034 | 0.06 | 0.062 |
| $\omega_\psi$ | 0.06 | 0.056 | 0.057 |
| $T_i$ | 0.222 | 0.181 | 0.201 |
| $L_{T_i}^{-1}$ | 1.788 | 1.480 | 1.386 |
| $T_e$ | 0.234 | 0.232 | 0.239 |
| $L_{T_e}^{-1}$ | 1.717 | 1.732 | 1.757 |
| $n_D$ | 0.194 | 0.380 | 0.314 |
| $L_{n_D}^{-1}$ | 2.063 | 2.818 | 1.487 |
| $n_e$ | 0.485 | 0.487 | 0.402 |
| $L_{n_e}^{-1}$ | 2.063 | 2.078 | 0.734 |
| $n_C$ | 0.049 | 0.018 | 0.015 |
| $L_{n_C}^{-1}$ | 2.063 | -0.555 | -1.96 |
| $\beta(\%)$ | 0.80% | 0.89% | 0.77% |
| $\nu_D(\times 10^{-4})$ | 1.61 | 2.13 | 1.59 |
| $\nu_e(\times 10^{-3})$ | 8.91 | 8.85 | 7.34 |
| $\nu_C(\times 10^{-3})$ | 2.37 | 3.14 | 2.34 |

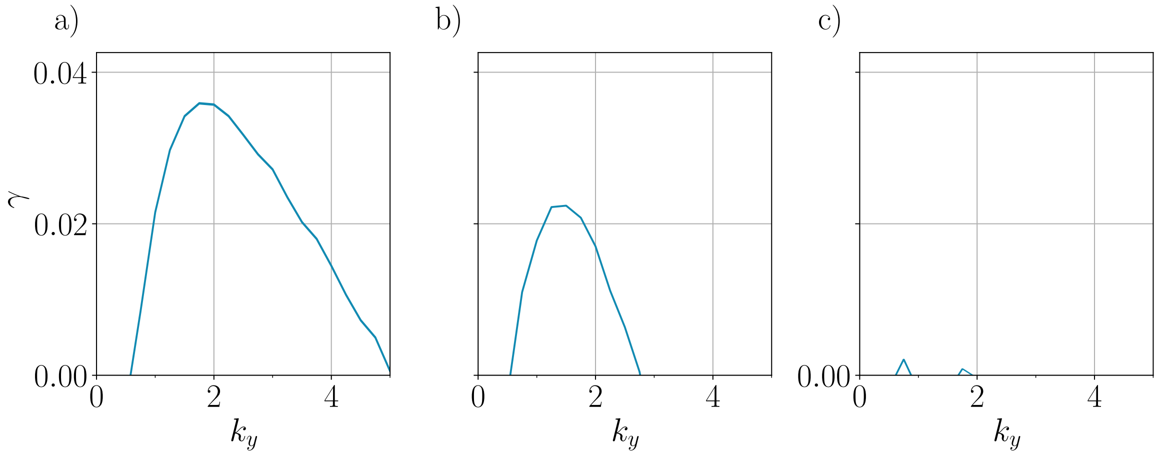

Figure 3.28: Electrostatic Floquet-averaged growth-rate spectra for equilibrium a) A, b) B and c) C. Both parallel and perpendicular components of equilibrium flow-shear are included.

We also studied the effect of adding both components of equilibrium flow shear for each equilibrium. Scans in the shearing rate were not performed as there is less uncertainty in the toroidal velocity profile outside the barrier. The Floquet-averaged growth rates are shown in Figure 3.28 as a function of $k_y$. Electromagnetic effects are not included. By comparison with Figures 3.27a) to c), one can see that the inclusion of flow shear has a significant stabilizing effect at all $k_y$ for all three equilibria. In particular, equilibrium C is almost completely stable over the course of a Floquet oscillation at all $k_y$. This does not guarantee that the turbulent transport will be zero – the transient growth cycle of the Floquet modes can still, in principle, drive 'subcritical' turbulence [122, 35, 123]. Nevertheless, the inclusion of flow-shear is expected to reduce the heat and particle fluxes.

### 3.3.2 Nonlinear results

We next present the results of nonlinear simulations in the outer region. We performed nonlinear electrostatic simulations of all three equilibria with and without equilibrium flow shear. The resolutions for all simulations were identical, and are shown in Table 3.5. Experimental flux levels are shown in Table 3.6. Electromagnetic simulations were performed but their results are not shown – the inclusion of magnetic fluctuations had

Table 3.5: Resolution parameters for nonlinear simulations in the outer region.

| Item | Value | Description |
|---|---|---|
| `ntheta` | 32 | Parallel grid points per $2\pi$ domain |
| `negrid` | 16 | Number of energy grid points |
| $2 \cdot$ `ngauss` | 10 | Number of passing pitch angles per sign of $v_\parallel$ |
| `vcut` | 3 | Ratio of $v$ to $v_{\mathrm{th},s}$ above which $h_s = 0$ is forced |
| $\Delta k_y$ | 0.150 | Grid spacing in $k_y$ |
| $k_{y,\mathrm{max}}$ | 3.153 | Maximum $k_y$ |
| $2\pi\hat{s}\Delta k_y/\Delta k_x$ | 4 | Sets $k_x$ grid spacing |
| $N_{k_x}$ | 256 | Number of $k_x$ values |

Table 3.6: Experimental flux levels calculated using JETTO, normalized to the gyro-Bohm values defined in Appendix B, for the three equilibria outside the foot of the barrier.

| Parameter | A | B | C |
|---|---|---|---|
| $Q_i(\times 10^{-2})$ | 3.52 | 3.50 | 3.79 |
| $Q_e(\times 10^{-2})$ | 2.62 | 1.94 | 2.07 |
| $\Pi(\times 10^{-2})$ | 8.26 | 7.56 | 8.01 |
| $\Gamma_i(\times 10^{-2})$ | 1.16 | 1.06 | 1.14 |
| $\Gamma_e(\times 10^{-2})$ | 1.18 | 1.07 | 1.16 |

little quantitative effect on any of the transport channels. Time traces of the heat, particle and momentum fluxes with and without equilibrium flow shear are shown in Figure 3.29. Without flow shear, both equilibria B and C are able to match the ion heat flux, whilst equilibrium A underpredicts it significantly. With the inclusion of flow shear, all equilibria underpredict the ion heat flux. Equilibrium B overpredicts all other transport channels with and without the inclusion of flow shear. Equilibria A and C are close to the experimental electron transport with and without flow shear, though A tends to overpredict it. C overpredicts the ion particle transport, but the addition of flow shear brings it closer to the experimental level, while A matches closely without flow shear. In general, all transport levels increase slightly for equilibrium

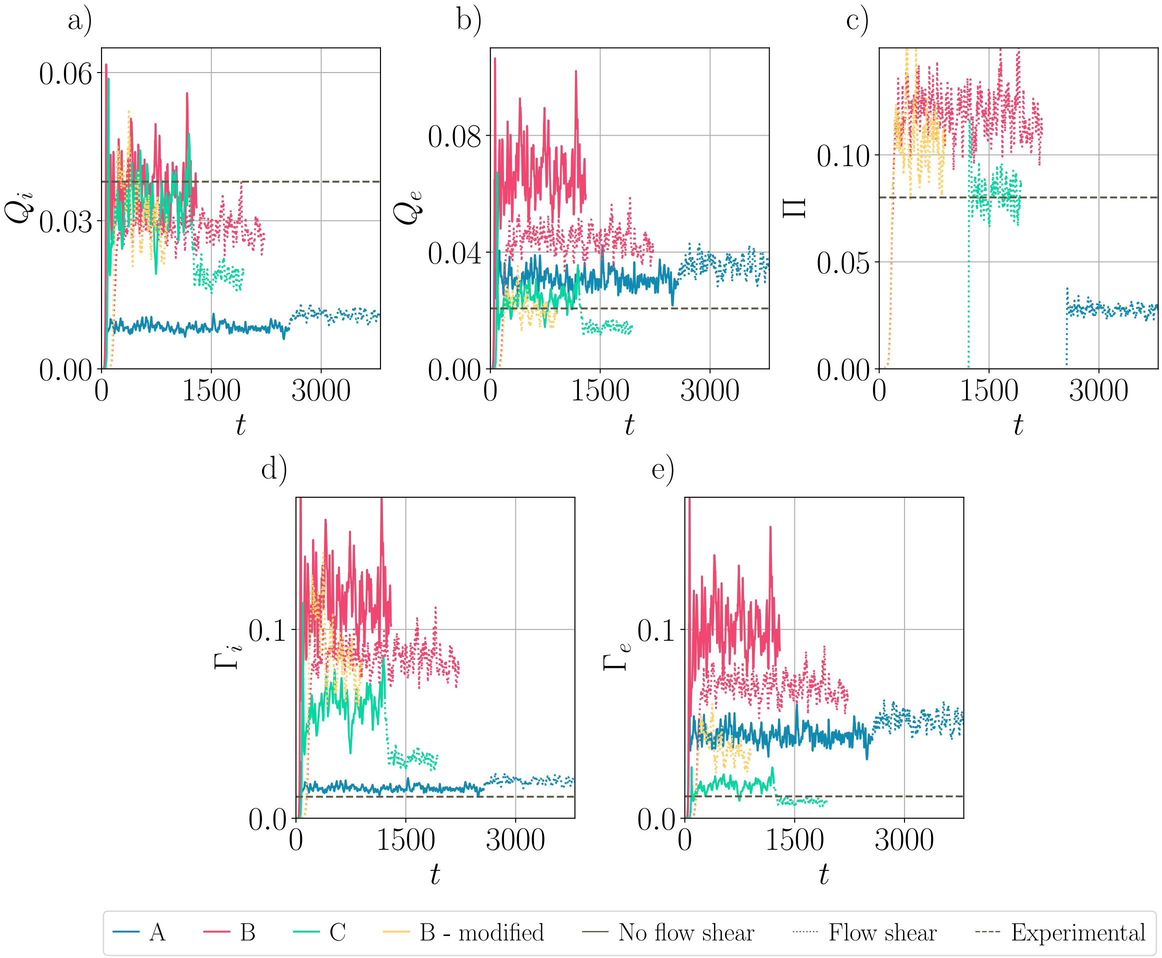

Figure 3.29: Time traces of a) ion heat flux, b) electron heat flux and c) momentum flux for equilibria A, B and C with and without equilibrium flow-shear effects (FS). Experimental flux levels corresponding to equilibrium C are shown by the dashed lines. Results are also shown for a modified version of equilibrium B where $L_{n_D}^{-1} = 3.4$, $L_{n_e}^{-1} = 1.7$, $L_{T_i}^{-1} = 1.8$, $L_{T_e}^{-1} = 1.2$ and $\alpha_{\mathrm{MHD}}$ was changed consistently. The discrepancies between ion and electron particle fluxes arise due to the presence of the carbon impurity – this also enables the electron particle flux to be lower than the total ion flux when the carbon particle flux is negative.

A when flow shear is added, despite the increased linear stability. The momentum transport matches closely for equilibrium C, whilst A and B are too low and too high, respectively. Whilst none of the three equilibria are able to match simultaneously every single transport channel, equilibrium C agrees with experiment across three of the five transport channels. Rather than further tweaking various gradients and parameters by 10% to obtain an exact match to every flux at once, we simply state that it is likely that a set of equilibrium profiles can be fitted within error bars that matches all transport channels closely. To illustrate this, we adjusted equilibrium B so that $L_{n_D}^{-1} = 3.4$, $L_{n_e}^{-1} = 1.7$, $L_{T_i}^{-1} = 1.8$ and $L_{T_e}^{-1} = 1.2$, with $\alpha_{\mathrm{MHD}}$ changed consistently. By doing so, the flux matching was improved for electron heat flux, momentum flux and electron particle flux. However, not much insight can be gained from this process, so we did not persist with adjusting other equilibria. Nevertheless, we have shown that multiple flux channels can be matched outside the transport barrier with local, electrostatic $\delta f$ gyrokinetic simulations, and that experimentally-relevant levels of equilibrium flow shear can have a significant impact.

## 3.4 Conclusions

In this Chapter we presented a study of a JET pulse that featured a strong ITB in the ion temperature. Due to the relatively large error bars on experimental measurements of key plasma parameters such as temperature and toroidal velocity, we fitted three profiles to the experimental data. This allowed us to sample a variety of possible self-consistent barrier configurations. By performing linear studies of the three equilibria in the mid-barrier region where the inverse temperature length scale is maximal, we established that the slab and toroidal ITG branches exist in competition. Electromagnetic effects were found to be stabilizing for both ITG branches, while a KBM was destabilized at low $k_y$. At sufficiently negative magnetic shear, it was shown that the KBM is stabilized. When full equilibrium flow-shear effects are considered, the KBM can be destabilized by PVG, suggesting that significant levels of flow shear might increase transport. This was confirmed by nonlinear simulations. Both electrostatic and electromagnetic nonlinear simulations were performed, and electromagnetic effects were critical for matching multiple transport channels to experimental levels. The addition of small amounts of flow shear has the potential to further improve the matching, but fluxes rapidly increase above experimental levels for $\gamma_{E\times B} \gtrsim 0.04$. Nonlinear scans in the global magnetic shear $\hat{s}$ showed that at smaller $-\hat{s}$, the KBM contributes to significant transport in all channels, well above experimental levels. Interestingly, increasing $-\hat{s}$ beyond the nominal levels also increased the transport. We suggested that this is due to a weaker coupling to the zonal mode, though it is unclear whether this is an issue of resolution, or if there may be a physical basis. We also simulated the region outside the foot of the barrier. From linear simulations, it was determined that the three equilibria display similar linear stability properties, with the growth rate spectra being dominated by a broad ITG mode. Electromagnetic effects are unimportant outside the barrier, and equilibrium flow shear was shown to have an important stabilizing effect both linearly and nonlinearly. From nonlinear simulations of the three equilibria with and without flow shear, we determined that multiple flux channels could be matched to experiment, and that plausible changes to the driving gradients could allow simultaneous matching to experiment of all transport channels.

From the simulations in these two radial locations, we have built up a physical picture of the key mechanisms that reduce turbulent transport in the transport barrier. At the mid-barrier region where the inverse temperature length scale is maximal, electromagnetic effects provide an order-of-magnitude reduction in the fluxes due to the high $\beta \sim 3\%$. The KBM that is typically driven unstable at such high $\beta$ is stabilized by the strongly negative magnetic shear that arises from the sharp cut-off in the pressure gradient at the upper end of the barrier. At such high $\beta$, equilibrium flow shear is *not* the dominant stabilizing effect. In fact, we suggest that it is counterproductive to have strongly sheared flows deep in the barrier. We claim that the strong equilibrium flow shear observed in many ITBs may be important for accessing this high-$\beta$ region, damping the electrostatic turbulence and enabling barrier formation at low $\beta$. However, we suggest that too high $\gamma_{E\times B}$ in the high-$\beta$ region would limit the maximum achievable

$\beta$ by destabilizing magnetic instabilities. Further work must be done to confirm that the increased confinement in the low-barrier region is provided by flow shear.

# Chapter 4

# Concluding remarks

In this Chapter we will present the key contributions of the Thesis, as well as outlining possible future work to build upon the findings discussed. This Thesis has primarily used local gyrokinetic simulations to make key discoveries about microstability in tokamak plasmas, particularly in high-performance conditions with high $\beta$ and steep pressure gradients. We find that experimental fluxes can be matched both deep in the ITB and outside the foot of the barrier with local $\delta f$ gyrokinetic simulations. The inclusion of electromagnetic fluctuations is critical for suppressing ITG in the region of steep temperature gradients, whilst negative magnetic shear is necessary to suppress the KBM. While flow shear is beneficial near the foot of the barrier for stabilizing ITG, it is deleterious for confinement deep inside the ITB. Flux surface elongation was also found to deteriorate the region of KBM second stability, contrary to the general understanding that elongation is uniformly stabilizing.

In Chapter 2, we focused on two JT-60SA-relevant equilibria and studied the effect of flux-surface shaping on their microstability and confinement. Electrostatic studies of these equilibria provided two important contributions. Firstly, we observed that in the equilibrium with a steep normalized pressure gradient $\alpha_{\mathrm{MHD}}$, both the linear stability and turbulent transport with maximally shaped $\{\delta, \kappa\} = \{0.5, 2\}$ flux surfaces were comparable to that with circular ones. This is in contrast to the lower pressure gradient equilibrium, where maximal shaping minimized the turbulent transport. As such, we might expect plasmas exhibiting steep pressure gradients to benefit from minimal shaping, which is in opposition to the typical picture presented in the literature.

This phenomenon is explained by the second key result of the electrostatic studies in Chapter 2: increased elongation can decrease stability at low triangularity. This can be understood as a competition between the FLR- and drive-damping effects introduced in Section 1.4.1, which is manifest once the normalized pressure gradient $\alpha_{\mathrm{MHD}}$ exceeds a certain value. As demonstrated in Figure 2.6b), for the nominal equilibrium parameters simulated here, that value is around 0.5. For small $\beta \ll 1\%$, where EM effects are unimportant, typical values of $q^2R(\log p)'$ must be of order 100 to reach $\alpha_{\mathrm{MHD}} \sim 1$. This occurs only in the pedestal region of plasmas containing edge transport barriers, so one may not expect these results to be relevant in the core of most tokamak plasmas. By extrapolation of the trends in Figure 2.5, this destabilizing effect of elongation may become more readily observable for negative triangularity. However, this has not been investigated, and is suggested as a possible topic for further exploration. These electrostatic studies guided us to search for similar results with fully EM fluctuations considered. With EM effects included, the KBM was destabilized at high $\beta$. We found that at sufficiently high $\beta$, increased shaping monotonically stabilized the KBM. We showed that this result can be understood as shaping reducing the effect of the magnetic fluctuations, and we refer to this as magnetic damping. Nevertheless, at sufficiently high $\beta$ where KBM second stability is accessible, we demonstrated in Figure 2.9 that increased elongation can remove second stability, rapidly increasing growth rates. Only linear simulations were performed with electromagnetic fluctuations included, and we suggest that nonlinear simulations be used to indicate whether the transport trends echo the linear stability at high $\beta$. At these high values of $\beta$, the trends suggest that decreasing $\kappa$ *below* unity may provide access to second stability at even lower $\beta$. Further studies would be required to validate this, and we acknowledge that MHD analysis predicts worse $\beta$ limits for less-elongated plasmas [68].

In Chapter 3, we studied a JET pulse containing an ion-temperature ITB, paying particular attention to the region of the ITB where $L_{T_i}^{-1}$ was maximal. Linear local, $\delta f$ gyrokinetic simulations were used to study the dominant microinstabilities, determining that slab and toroidal branches of ITG can coexist at these steep temperature gradients. The inclusion of electromagnetic fluctuations partially stabilized both ITB branches, and also allowed for the destabilization of a KBM. The addition of significant negative magnetic shear was shown to suppress the KBM. Strong equilibrium flow shear ($\gamma_{E\times B} \gtrsim 0.08$) was shown, linearly, to destabilize the KBM in these plasmas. Nonlinear gyrokinetic simulations were also performed; by and large, the trends in transport levels follow those observed in linear stability. Notably, the inclusion of EM effects in nonlinear simulations resulted in a more significant reduction in transport than might be expected from the reduced linear growth rates. This is consistent with previous studies of electromagnetic turbulence [47]. By performing a range of nonlinear gyrokinetic simulations, we were able to find local equilibrium parameters consistent with experimental measurements where multiple transport channels could simultaneously be matched to experimental levels at two radial locations. Linear and nonlinear parameter scans have allowed us to build up a picture of the key stabilization mechanisms in the mid-barrier. The EM effects stabilize the toroidal and slab ITG turbulence, whilst the stabilization of the KBM by magnetic shear is crucial for the reduction of transport levels. The addition of significant levels of flow shear destabilizes the KBM via the velocity shear parallel to the mean magnetic field, leading to a significant increase in transport, notably in the electron $\delta A_{\|}$ heat flux. We therefore suggest that the coincidence of significant equilibrium flow shear *and* high-$\beta$ is not compatible with the reduced transport levels and steep driving gradients of a transport barrier. However, the presence of strongly sheared equilibrium flows may enable the formation of transport barriers at low $\beta$. The matching of experimental fluxes demonstrates the viability of local gyrokinetics for studying transport barriers, and opens up the possibility of using a first principles model to simulate the formation of an ITB. To do this, one would need to be confident that fluxes could be matched across a wider range of radial positions than we have studied so far. In particular, we suggest that similar studies could be carried out at the barrier foot and top. Study of the top of the barrier is important to understand the barrier saturation mechanism, i.e. why high $L_{T_i}^{-1}$ cannot be sustained deeper into the core plasma for this pulse. Similarly, the physics at the foot of the barrier is critical for understanding how $L_{T_i}^{-1}$ is able to ramp up without increased transport. We believe, based on constraints placed on the equilibrium flow shear profiles in this study, that the flow shear profile should be peaked around the foot of the barrier, and is expected to provide significant stabilization until $\beta$ becomes high enough to significantly reduce the transport. If these proposed studies are successful in reproducing experimental transport levels, we are confident that a 1D transport solver, coupled to `GS2`, could demonstrate the formation of an ITB. Such simulations would be possible using `TRINITY` coupled to `GS2`[124].

One unanswered question that requires further study relates to the role of magnetic shear in stabilizing the KBM. We observed that at magnetic shear that is more negative than nominal, the transport levels increased despite the reduction in the KBM linear growth rates. Further work should be carried out to ensure that this result is not a consequence of insufficient simulation resolution. We suggest performing a simulation with the same $\Delta k_x$ as the nominal case. The persistence of increased transport with increased resolution would indicate a physical origin for our observation. Our studies indicate that the coupling of the zonal mode with EM effects could be an important starting point for such studies. The effect of magnetic shear on the magnetic damping may play a role – it was observed in Chapter 2 that when the KBM was stabilized by increased $|\boldsymbol{k}_\perp|$, the ITG was destabilized, possibly by the reduced $\delta A_\parallel$ stabilization. Alongside the above studies, ITB pulses from other tokamaks should be studied to see whether similar pictures of the ITB formation can be built up. The JT-60U tokamak, which was run with an optimized magnetic shear profile in a similar way to the JET pulse studied here, would be a good starting point for such studies.

# Appendix A

# Calculating geometric effects within the local framework

## A.1 Calculation of the local magnetic shear and perpendicular wavenumber

In this section we flesh out the details of how to determine the effect of shaping parameters on stability. As an example, we show an analytic calculation of the effect of elongation to leading order in $\epsilon \ll 1$. As discussed in Chapter 2, this involves determining the local magnetic shear and the perpendicular wavenumber. We note that the quantities in this Appendix are not normalized as in the rest of the Thesis.

The local safety factor $\tilde{q}$ is the ratio of the toroidal to poloidal component of the magnetic field:

$$\tilde{q} \equiv \frac{B \cdot \nabla \zeta}{B \cdot \nabla \theta} = \frac{I \mathcal{J}_r}{R^2 \psi'} \tag{A.1}$$

where we used the axisymmetric form of the magnetic field:

$$\boldsymbol{B} = I \nabla \zeta + \nabla \zeta \times \nabla \psi \tag{A.2}$$

and defined the Jacobian $\mathcal{J}_X$ for the transformation between $\{R, \zeta, Z\} \to \{X, \theta, \zeta\}$ where $X$ is any flux-surface label. This also allows us to define $\psi'$ in terms of the safety factor $q$:

$$\psi' = \frac{I}{2\pi q} \int_0^{2\pi} \mathrm{d}\theta \frac{\mathcal{J}_r}{R^2}, \tag{A.3}$$

where $'$ indicates a derivative with respect to $r$. Therefore, the local magnetic shear is

$$\tilde{s} \equiv r\frac{\tilde{q}'}{\tilde{q}} = r\biggl(\frac{I'}{I} + \frac{J}{\mathcal{J}_r} - 2\frac{R'}{R}\biggr). \tag{A.4}$$

where $J \equiv \mathcal{J}_r' - \mathcal{J}_r\psi''/\psi'$. To evaluate this, we use the Grad-Shafranov equation:

$$R^2\nabla\cdot\left(\frac{\nabla\psi}{R^2}\right) = -\frac{II' + 4\pi R^2 p'}{\psi'}. \tag{A.5}$$

By expanding the divergence and substituting explicit forms for $\nabla r$ and $\nabla\theta$ in terms of $R(r,\theta)$ and $Z(r,\theta)$:

$$\nabla r = \frac{R}{\mathcal{J}_r}\biggl(\frac{\partial R}{\partial\theta}\nabla Z - \frac{\partial Z}{\partial\theta}\nabla R\biggr); \tag{A.6}$$

$$\nabla\theta = \frac{R}{\mathcal{J}_r}\biggl(\frac{\partial Z}{\partial r}\nabla R - \frac{\partial R}{\partial r}\nabla Z\biggr), \tag{A.7}$$

we arrive at the following expression for $J/\mathcal{J}_r$:

$$\frac{J}{\mathcal{J}_r} = \frac{R^2}{\mathcal{J}_r^2|\nabla r|^2}\Biggl[2\biggl(R'^{\theta}R^{\theta} + Z'^{\theta}Z^{\theta}\biggr) - \mathcal{J}_r\frac{\partial}{\partial\theta}\biggl(\frac{1}{\mathcal{J}_r}\Bigl[R'R^{\theta} + Z'Z^{\theta}\Bigr]\biggr)\Biggr] + \frac{II' + 4\pi R^2 p'}{|\nabla\psi|^2}, \tag{A.8}$$

where superscript $\theta$ indicates a $\theta$-derivative. To get an expression for $I'/I$, we take the $r$-derivative of Equation (A.3) and move all terms under the integral:

$$0 = \int_0^{2\pi} \mathrm{d}\theta\Biggl[\frac{J}{R^2} + \frac{\mathcal{J}_r}{R^2}\biggl(\frac{I'}{I} - \frac{q'}{q} - \frac{2R'}{R}\biggr)\Biggr]. \tag{A.9}$$

This can be used in conjunction with Equation (A.8) integrated over $\theta$ to give an expression for $I'$:

$$\frac{I'}{I}\int_0^{2\pi}\mathrm{d}\theta\frac{\mathcal{J}_r}{R^2}\biggl(1 + \frac{I^2}{|\nabla\psi|^2}\biggr) = \int_0^{2\pi}\mathrm{d}\theta\frac{\mathcal{J}_r}{R^2}\biggl(\frac{q'}{q} + \frac{2R'}{R} - \frac{4\pi R^2 p'}{|\nabla\psi|^2}\biggr) + \int_0^{2\pi}\frac{\mathrm{d}\theta}{|\nabla r|^2}\Biggl(\frac{\partial}{\partial\theta}\biggl(\frac{1}{\mathcal{J}_r}\Bigl[R'R^{\theta} + Z'Z^{\theta}\Bigr]\biggr) - \frac{2}{\mathcal{J}_r}\biggl(R'^{\theta}R^{\theta} + Z'^{\theta}Z^{\theta}\biggr)\Biggr). \tag{A.10}$$

With these expressions, one can generate expressions for $\tilde{s}$ and thus $|\boldsymbol{k}_\perp|^2$.

## A.2 Analytical expressions for concentric elliptical flux-surfaces

We next use a simplified Miller parametrization that includes only elongation to determine the effect of elongating a circular plasma:

$$R(r,\theta) = R_0 + r\cos\theta \tag{A.11}$$

$$Z(r,\theta) = \kappa(r) r\sin\theta \tag{A.12}$$

We choose to order $\kappa' \sim \kappa/R_0$ – this means that $\kappa'$ does not enter to leading order in small inverse aspect ratio ($\epsilon \ll 1$):

$$Z'(r,\theta) = \kappa\sin\theta + \kappa'\epsilon R_0 \sin\theta = \kappa\sin\theta + \mathcal{O}(\epsilon). \tag{A.13}$$

We proceed in this limit to determine $\tilde{s}$ and $|\boldsymbol{k}_\perp|^2$, beginning with the following quantities:

$$\mathcal{J}_r(r,\theta) = R\big(R'Z^\theta - R^\theta Z'\big) = \kappa r R \tag{A.14}$$

$$|\nabla r|^2 \equiv \frac{R^2}{\mathcal{J}_r^2}\bigg(\big(R^\theta\big)^2 + \big(Z^\theta\big)^2\bigg) = \frac{1 + (\kappa^2-1)\cos^2\theta}{\kappa^2} \tag{A.15}$$

$$|\nabla\theta|^2 \equiv \frac{R^2}{\mathcal{J}_r^2}\bigg(\big(R'\big)^2 + \big(Z'\big)^2\bigg) = \frac{1 + (\kappa^2-1)\sin^2\theta}{r^2\kappa^2} \tag{A.16}$$

$$\nabla r\cdot\nabla\theta \equiv -\frac{R^2}{\mathcal{J}_r^2}\bigg(R'R^\theta + Z'Z^\theta\bigg) = -\frac{(\kappa^2-1)\sin\theta\cos\theta}{r\kappa^2} \tag{A.17}$$

$$\psi' = \frac{I\kappa\epsilon}{q} + \mathcal{O}(I\epsilon^3). \tag{A.18}$$

To determine $I'/I$, we calculate each of the three integrals that appear in Equation A.10 separately:

$$\int_0^{2\pi} \mathrm{d}\theta \frac{\mathcal{J}_r}{R^2}\bigg(1 + \frac{I^2}{|\nabla\psi|^2}\bigg) = \frac{2\pi q^2}{\epsilon} + \mathcal{O}(\epsilon) \tag{A.19}$$

$$\int_0^{2\pi} \mathrm{d}\theta \frac{\mathcal{J}_r}{R^2}\bigg(\frac{q'}{q} + \frac{2R'}{R} - \frac{4\pi R^2 p'}{|\nabla\psi|^2}\bigg) = \frac{2\pi}{\epsilon R_0}\bigg\{\kappa\epsilon\hat{s} + \frac{\alpha_{\mathrm{MHD}}}{2}\bigg\} + \mathcal{O}(\epsilon/R_0) \tag{A.20}$$

$$\int_0^{2\pi} \frac{\mathrm{d}\theta}{|\nabla r|^2}\Bigg(\frac{\partial}{\partial\theta}\bigg(\frac{1}{\mathcal{J}_r}\Big[R'R^\theta + Z'Z^\theta\Big]\bigg) - \frac{2}{\mathcal{J}_r}\bigg(R'^\theta R^\theta + Z'^\theta Z^\theta\bigg)\Bigg) = -\frac{2\pi}{R_0}\big(\kappa^2+1\big) + \mathcal{O}(\epsilon/R_0). \tag{A.21}$$

In the above, $\alpha_{\text{MHD}} \equiv -\beta(\log p)' q^2 R_0$. Combining these expressions, we find that

$$\frac{I'}{I}\frac{q^2}{\epsilon}R_0 = \kappa\left(\hat{s} - \frac{\kappa^2+1}{\kappa}\right) + \frac{\alpha_{\text{MHD}}}{2}\frac{1}{\epsilon} + \mathcal{O}(\epsilon). \tag{A.22}$$

Later, when calculating $\tilde{s}$ using Equation A.4, we will find that the leading order contribution cancels with a term in $J/\mathcal{J}_r$, so we retain the $\mathcal{O}(1)$ terms. Using this, we find:

$$\frac{J}{\mathcal{J}_r} = \frac{1}{\epsilon R_0}\left\{\frac{\kappa\hat{s} - \alpha_{\text{MHD}}\cos\theta}{1+(\kappa^2-1)\cos^2\theta}\right\}.$$

Comparing the size of the terms that comprise $\tilde{s}$ in Equation A.4, the largest is $J/\mathcal{J}_r$. Then, to leading order, we find

$$\tilde{s} = \frac{\kappa\hat{s} - \alpha_{\text{MHD}}\cos\theta}{1+(\kappa^2-1)\cos^2\theta}. \tag{A.23}$$

Now we can use $\tilde{s}$ to find $\nabla\tilde{\alpha}$ and thus $|\boldsymbol{k}_\perp|^2$. This requires us to evaluate the following integral as:

$$\int_0^\theta \mathrm{d}\hat{\theta}\tilde{q}' = \frac{q}{r}\left[\hat{s}\vartheta - \alpha_{\text{MHD}}\Lambda\right], \tag{A.24}$$

where

$$\Lambda(\theta,\kappa) \equiv \frac{1}{2\kappa\sqrt{\kappa^2-1}}\log\left(\frac{1+\sqrt{1-\kappa^{-2}}\sin\theta}{1-\sqrt{1-\kappa^{-2}}\sin\theta}\right) \tag{A.25}$$

and

$$\vartheta(\theta,\kappa) \equiv \arctan\left(\frac{\tan\theta}{\kappa}\right). \tag{A.26}$$

By expressing $\boldsymbol{k}_\perp$ in the normalized `GS2` coordinates $x$ and $y$ defined in Section 1.3.3, we can write

$$|\boldsymbol{k}_\perp|^2 = k_y^2\left[(\hat{s}\theta_0)^2|\nabla x|^2 + 2\hat{s}\theta_0\nabla x\cdot\nabla y + |\nabla y|^2\right], \tag{A.27}$$

where $\theta_0 \equiv k_x/(\hat{s}k_y)$. Evaluating this yields the following expression for $|\boldsymbol{k}_\perp|^2$:

$$\begin{aligned}|\boldsymbol{k}_\perp|^2 = k_y^2\Big[&\big(\hat{s}(\vartheta-\theta_0) - \alpha_{\text{MHD}}\Lambda\big)^2\big(1+(\kappa^2-1)\cos^2\theta\big) + 1 + (\kappa^2-1)\sin^2\theta \\ &-2\big(\hat{s}(\vartheta-\theta_0) - \alpha_{\text{MHD}}\Lambda\big)(\kappa^2-1)\sin\theta\cos\theta\Big] + \mathcal{O}(\epsilon).\end{aligned} \tag{A.28}$$

We note that the normalizing coefficients of $x$ and $y$ in Equations 1.25 and 1.26 act to cancel out factors of $q$, $\kappa$, $\tilde{\psi}'$ and so forth, such that the only common prefactor is $k_y^2$. These expressions reduce to the typical $\hat{s} - \alpha_{\mathrm{MHD}}$ results when $\kappa = 1$, since $\Lambda(\theta, 1) = \sin\theta$ and $\vartheta(\theta, 1) = \theta$. In Figure A.1 we plot for this model the local shear at the outboard midplane, and the integral of $|\boldsymbol{k}_\perp|^2$ over the outboard side, as a function of $\alpha_{\mathrm{MHD}}$ and $\kappa$. Comparing Figures A.1a) and b) to Figures 2.6b) and c), we see good agreement despite ignoring the effects of triangularity, Shafranov shift and finite-aspect-ratio.

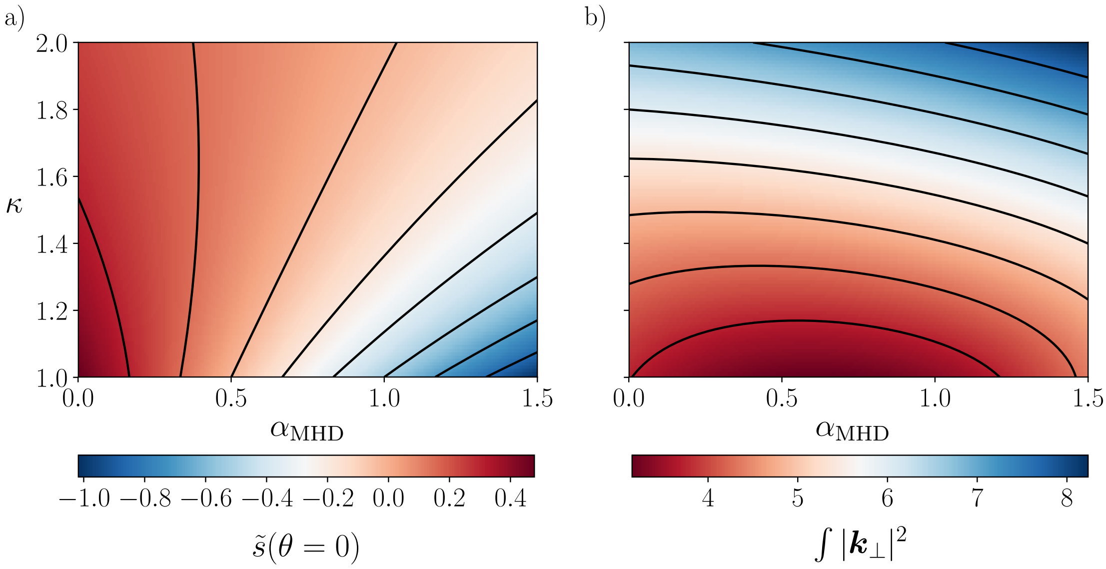

Figure A.1: Profiles calculated from our simple analytical model that includes just elongation and pressure-gradient effects in the small-inverse-aspect-ratio limit. We show a) the local magnetic shear at the outboard midplane and b) the integral of $|\boldsymbol{k}_\perp|^2$ over $-\pi/2 \leq \theta \leq \pi/2$, as a function of $\alpha_{\mathrm{MHD}}$ and $\kappa$. The value of $\hat{s}$ is 0.48, $k_y = 1$ and $k_x = 0$.

# Appendix B

# Normalizations

## B.1 Converting between normalizing quantities in `GS2` and `GKV`

`GS2` and `GKV` use different variables to normalize the various dimensional quantities appearing in the governing equations. In this section, we will explicitly include all normalizing quantities for clarity. Unlike `GS2`, `GKV` uses $R_{ax}$, the major radius of the magnetic axis, to normalize macroscopic length scales such as $L_T^{-1}$. `GKV` uses different flux-tube coordinates compared with `GS2`:

$$x_{\texttt{GKV}} = a_{\texttt{GKV}}(\rho - \rho_0) \tag{B.1}$$

$$y_{\texttt{GKV}} = \frac{a_{\texttt{GKV}}\rho_0}{q(\rho_0)}(q(\rho)\theta - \zeta) \tag{B.2}$$

where $a_{\texttt{GKV}} \equiv \sqrt{2\Phi_{\mathrm{LCFS}}/B_{ax}}$ is the plasma minor radius, $\rho \equiv \sqrt{\Phi/\Phi_{\mathrm{LCFS}}}$, $\Phi$ is the toroidal magnetic flux and the subscript (LCFS) indicates its value at the last closed flux surface. Inverse length scales $L_X^{-1}$ in `GKV` are defined correspondingly as

$$\left.\frac{R_{ax}}{L_X^{-1}}\right|_{\texttt{GKV}} \equiv -R_{ax}\frac{d\log X}{dx_{\texttt{GKV}}} = -\frac{R_{ax}}{a_{\texttt{GKV}}}\frac{d\log X}{d\rho}, \tag{B.3}$$

so can be related to `GS2` quantities as:

$$\left.\frac{a}{L_X^{-1}}\right|_{\texttt{GS2}} \equiv -a\frac{d\log X}{dr} = \left.\frac{R_{ax}}{L_X^{-1}}\right|_{\texttt{GKV}}\frac{a_{\texttt{GKV}}}{R_{ax}}a\frac{d\rho}{dr}, \tag{B.4}$$

where $a$ is the minor radius of the LCFS.

With the different definitions for flux-tube coordinates, wavenumbers must also be renormalized for direct comparison between the two codes. We focus only on $k_y$ as all the simulations in Section 2.1 are performed at $k_x = 0$ for both codes. Using the definitions for $y$ and $y_{\texttt{GKV}}$ given in Equations 1.26 and B.2, respectively, we can relate $k_y$ for the two codes as follows:

$$k_{y,\texttt{GKV}} = k_{y,\texttt{GS2}} \frac{\tilde{\psi}_0' q(\rho_0)}{B_0 a_{\texttt{GKV}} \rho_0} \tag{B.5}$$

In `GS2`, the reference gyroradius to which the wavenumber is normalized is defined as

$$\rho_{\text{ref}}|_{\texttt{GS2}} \equiv \frac{\sqrt{2T_{\text{ref}} m_{\text{ref}}} c}{Z_{\text{ref}} e B_0}, \tag{B.6}$$

where $T_{\text{ref}}$ is the reference species temperature (we use the main-ion temperature at $r = 0$), $m_{\text{ref}}$ is the reference species mass (we use the main-ion mass) and $Z_{\text{ref}}$ is the reference species charge (we use unity for a deuterium plasma). A similar normalization is used in `GKV`, except the reference species is presumed to be hydrogen, and the thermal speed is defined to be smaller by a factor of $\sqrt{2}$:

$$\rho_{\text{ref}}|_{\texttt{GKV}} \equiv \frac{\sqrt{T_{\text{ref}} m_H} c}{e B_{ax}}. \tag{B.7}$$

By combining Equations B.5, B.6 and B.7, we can relate the normalized wavenumber in `GKV` to that of `GS2` according to:

$$(k_y \rho_{\text{ref}})|_{\texttt{GKV}} = (k_y \rho_{\text{ref}})|_{\texttt{GS2}} \frac{q(\rho_0)}{\rho_0} \frac{\tilde{\psi}_0'}{a_{\texttt{GKV}} B_{ax}} Z_{\text{ref}} \sqrt{\frac{m_H}{2 m_{\text{ref}}}}. \tag{B.8}$$

Time scales in `GKV` are normalized by the ratio of $R_{ax}$ to the thermal velocity of the reference hydrogen species. This means that the mode frequencies $\omega$ in `GS2` can be related to those of `GKV` via:

$$\left(\omega \frac{R_{ax}}{v_{\text{th,ref}}}\right)\Bigg|_{\texttt{GKV}} = \left(\omega \frac{a}{v_{\text{th,ref}}}\right)\Bigg|_{\texttt{GS2}} \frac{\sqrt{2} R_{ax}}{a} \sqrt{\frac{m_H}{m_{\text{ref}}}}. \tag{B.9}$$

## B.2 Normalized quantities in `GS2`

In Table B.1 we present the dimensional parameters as given in the text, along with the quantities used to normalize them. We note that $a$ is the minor radius of the LCFS, $\rho^* \equiv \rho_{\text{ref}}/a$, $n_{\text{ref}}$ is the electron density at $r = 0$ and the reference thermal speed is $v_{\text{th,ref}} \equiv \sqrt{2T_{\text{ref}}/m_{\text{ref}}}$.

Table B.1: All dimensional parameters used throughout this thesis that are presented without their normalizations for brevity. The quantities used to normalize them are shown along with a description of the parameter. Quantities with(without) an asterisk in their description are divided(multiplied) by the normalizing factor.

| Parameter | Normalizing factor | Description |
|---|---|---|
| $\lvert \boldsymbol{k}_\perp \rvert$, $k_x$, $k_y$ | $\rho_{\mathrm{ref}}$ | Perpendicular wavenumber |
| $k_\parallel$ | $a$ | Parallel wavenumber |
| $\omega$ | $a/v_{\mathrm{th,ref}}$ | Real frequency of fluctuations |
| $\gamma$ | $a/v_{\mathrm{th,ref}}$ | Linear growth rate |
| $Q_s$ | $n_{\mathrm{ref}} v_{\mathrm{th,ref}} T_{\mathrm{ref}} \rho^{*2}$ | Heat flux for species $s$ * |
| $\Pi_s$ | $n_{\mathrm{ref}} a m_{\mathrm{ref}} v_{\mathrm{th,ref}}^2 \rho^{*2}$ | Momentum flux for species $s$ * |
| $\Gamma_s$ | $n_{\mathrm{ref}} v_{\mathrm{th,ref}} \rho^{*2}$ | Particle flux for species $s$ * |
| $r$ | $a$ | Flux-surface minor radius * |
| $R$ | $a$ | Major radius of flux-surface centre * |
| $\kappa'$ | $a$ | Radial derivative of $\kappa$ |
| $\delta'$ | $a$ | Radial derivative of $\delta$ |
| $\beta'$ | $a$ | Normalized $p'$ |
| $\gamma_{E\times B}$ | $a/v_{\mathrm{th,ref}}$ | Toroidal flow shear rate |
| $\omega_\psi$ | $a/v_{\mathrm{th,ref}}$ | Toroidal angular velocity |
| $m_s$ | $m_{\mathrm{ref}}$ | Mass of species $s$ * |
| $T_s$ | $T_{\mathrm{ref}}$ | Temperature of species $s$ * |
| $n_s$ | $n_{\mathrm{ref}}$ | Density of species $s$ * |
| $c_s$ | $v_{\mathrm{th,ref}}$ | Sound speed * |
| $L_X^{-1}$ | $a$ | Inverse scale length of $X$ |
| $\nu_s$ | $a/v_{\mathrm{th,ref}}$ | Collisionality of species $s$ |

# Appendix C

# Slab ITG

## C.1 Derivation of the dispersion relation

In this Appendix we present an analytical study of the slab branch of the ITG instability. We derive a dispersion relation for a deuterium-electron plasma in unsheared slab geometry, including FLR effects, $\delta A_\parallel$ fluctuations and PVG. The background magnetic field is $\boldsymbol{B} = B\hat{\boldsymbol{z}}$, the mean flow velocity $\boldsymbol{u} \equiv u(x)\hat{\boldsymbol{z}}$ is low ($u \ll v_{\mathrm{th},s}$), and the two species are assumed to have equal temperature and density. We solve the linearized gyrokinetic equation in this geometry for a species $s$:

$$\frac{dh_s}{dt} + v_\parallel \boldsymbol{b}\cdot\nabla h_s = \frac{ef_{0,s}}{T_s}\frac{d\chi}{dt} - \frac{c}{B}\big(\boldsymbol{b}\times\nabla\langle\chi\rangle_{\boldsymbol{R}_s}\big)\cdot\bigg(\nabla f_{0,s} + v_\parallel\nabla u\bigg), \tag{C.1}$$

where $\mathrm{d}/\mathrm{d}t \equiv \partial/\partial t + \boldsymbol{u}\cdot\nabla$ and $\chi = J_0(\alpha_s)(\phi - (v_\parallel/c)\delta A_\parallel)$ since we ignore compressive magnetic fluctuations. We can neglect the advective terms $(\boldsymbol{u}\cdot\nabla)$ since $u \ll v_{\mathrm{th,ref}}$ and fluctuations are assumed to vary slowly parallel to the magnetic field. We assume solutions for fluctuating quantities $D$ of the form:

$$D(t,y,z) = \sum_{k_y,k_\parallel,\omega} \hat{D}_{k_y,k_\parallel,\omega}\exp(-i\omega t)\exp(ik_y y)\exp(ik_\parallel z) \tag{C.2}$$

for a complex frequency $\omega$, and choose only $x$-variation in the background temperature and density profiles, which allows us to set $|\boldsymbol{k}_\perp| = k_y$. This allows us to get a form for each Fourier component of $h_s$ (dropping ˆs and wavenumber labels for convenience) as

$$h_s = \frac{ef_{0,s}}{T_s}\frac{\omega - \omega^T_{*,s}}{\omega - v_\parallel k_\parallel}\left[\phi - \frac{v_\parallel}{c}\delta A_\parallel\right]J_0(\alpha_s), \tag{C.3}$$

where

$$\omega_{*,s}^T \equiv \omega_{*,s}\left[1+\eta_s\left(\frac{m_s v^2}{2T_s}-\frac{3}{2}\right)-\frac{m_s v_\parallel u' L_{n_s}}{T_s}\right]$$

and $\omega_{*,s} \equiv -k_y c T_s/(Z_s e B L_{n_s})$. We explicitly normalize quantities in this derivation for clarity. To relate $\delta\phi$ and $\delta A_\parallel$ and thus close the problem we use the quasineutrality and parallel current equations (Equations 1.22 and 1.23, respectively). After some algebra we reach the dispersion relation:

$$\left[b_i-\beta\left(\tilde{\Gamma}_{2,i}+\frac{m_i}{m_e}\tilde{\Gamma}_{2,e}\right)\right]\left(2+\tilde{\Gamma}_{0,i}+\tilde{\Gamma}_{0,e}\right)+\beta\left[\tilde{\Gamma}_{1,i}+\sqrt{\frac{m_i}{m_e}}\tilde{\Gamma}_{1,e}\right]^2=0, \tag{C.4}$$

where $b_s \equiv (k_y\rho_s)^2/2$, and

$$\tilde{\Gamma}_{n,s} \equiv \zeta_s Z_{n,s}-\bar{\zeta}_{*,s}\left\{\Gamma_0(b_s)Z_{n,s}+\eta_s\left(\Gamma_0(b_s)\left[Z_{n+2,s}-\frac{3}{2}Z_{n,s}\right]+\Gamma_1(b_s)Z_{n,s}\right)\right.$$
$$\left.-\,2\Gamma_0(b_s)Z_{n+1,s}\frac{u' L_{n_s}}{v_{\mathrm{th},s}}\right\}. \tag{C.5}$$

Here, $\bar{\zeta}_{*,s} \equiv \omega_{*,s}/(k_\parallel v_{\mathrm{th},s})$, $\zeta_s \equiv \omega/(|k_\parallel| v_{\mathrm{th},s})$ and the $\Gamma_n(b_s)$ come from integrating the Bessel functions; the relevant orders are:

$$\Gamma_0(b_s)=I_0(b_s)\mathrm{e}^{-b_s} \tag{C.6}$$

and

$$\Gamma_1(b_s)=\big((1-b_s)I_0(b_s)+b_s I_1(b_s)\big)\mathrm{e}^{-b_s}, \tag{C.7}$$

while the

$$Z_{n,s} \equiv \frac{1}{\sqrt{\pi}}\int_{-\infty}^{\infty}\mathrm{d}u\frac{u^n \mathrm{e}^{-u^2}}{u-\zeta_s}$$

result from integrating over parallel velocity with the resonant denominator for finite $k_\parallel$. Each order can be related back to the zeroth order expression via:

$$Z_{1,s}=1+\zeta_s Z_{0,s}$$

$$Z_{2,s}=\zeta_s Z_{1,s}$$
$$Z_{3,s}=\frac{1}{2}+\zeta_s^2 Z_{1,s}$$
$$Z_{4,s}=\zeta_s Z_{3,s}$$

Although one can simplify this dispersion relation significantly by only keeping terms to leading order in $\sqrt{m_i/m_e}$, we solve this dispersion numerically without making any further approximations to find how the linear spectra respond to changes in various parameters.

## C.2 Parameter dependence of slab ITG

In this Section we present the dependence of slab ITG growth-rate spectra on parameters such as $L_{T_i}^{-1}$, $\beta$ and $\gamma_{E\times B}$, with all quantities now in their normalized form according to Appendix $B$. It is known from the literature that slab ITG scales like $\omega \sim (k_{\|}^2 c_s^2 \omega_{*,i}\eta_i/2)^{1/3}$, where $c_s \equiv \sqrt{2T_e/m_i}$ is the sound speed [14]. At first glance, this suggests that the linear slab-ITG growth rate scales like $(L_{T_i})^{-1/3}$. We show in Figure C.1 a contour map of the growth rate as a function of $k_{\|}$ and $L_{T_i}^{-1}$ at fixed $k_y\rho_{\mathrm{ref}} = 1$. For a given $k_{\|}$, the growth rate is indeed not a linear function of $L_{T_i}^{-1}$. However, the $k_{\|}$ of the fastest growing mode also increases with $L_{T_i}^{-1}$ such that the maximum overall growth rate (i.e. for any $k_{\|}$) actually scales linearly with $L_{T_i}^{-1}$.

We show in Figure 3.8 a coarse scan in $\beta$ for a single $k_{\|} = 0.5$ with $k_x = 0$, $T_i = T_e$, $L_{T_i}^{-1} = 15$, $L_{T_e}^{-1} = 2$ and $L_{n_i}^{-1} = L_{n_e}^{-1} = 0$. The addition of field line bending only weakly stabilizes the slab branch of ITG at low $k_y$, whilst very slightly destabilizing the high-$k_y$ end of a given mode. Increasing the strength of PVG by increasing $u'$ has a destabilizing effect on the electrostatic slab modes at all $k_y$, as illustrated in Figure C.2. This result is qualitatively similar at finite $\beta$.

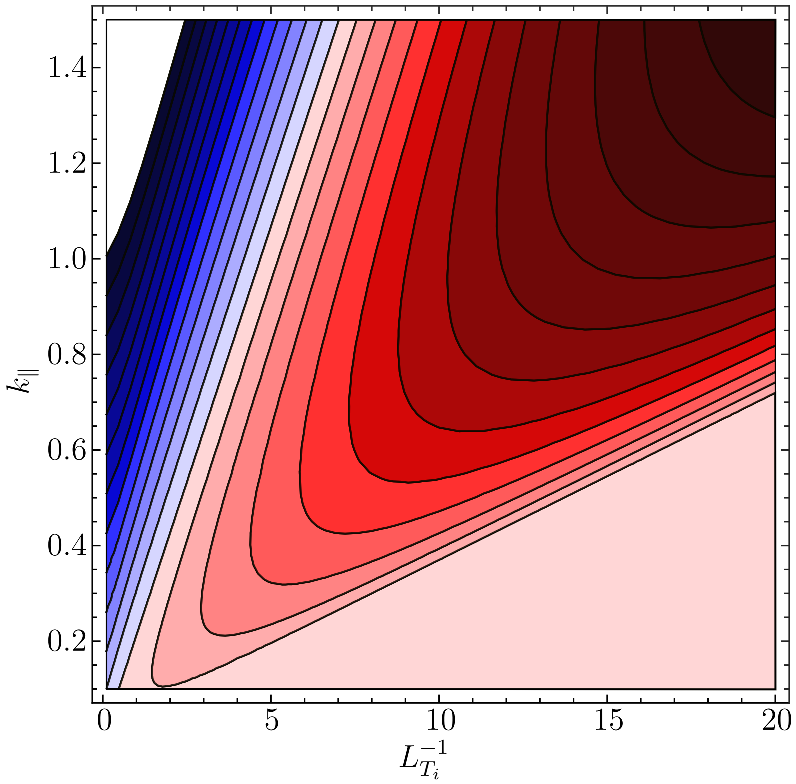

Figure C.1: Numerical solutions for the slab-ITG growth rate as a function of $k_\parallel$ and $L_{T_i}^{-1}$ at fixed $k_y = 1$. For the results shown, adiabatic electrons were used, $k_x = 0$, $\beta = 0$, $u' = 0$ and $L_{n_i}^{-1} = 0.01$. The solver did not converge well for the white region in the top left or the large light-red region in the bottom right.

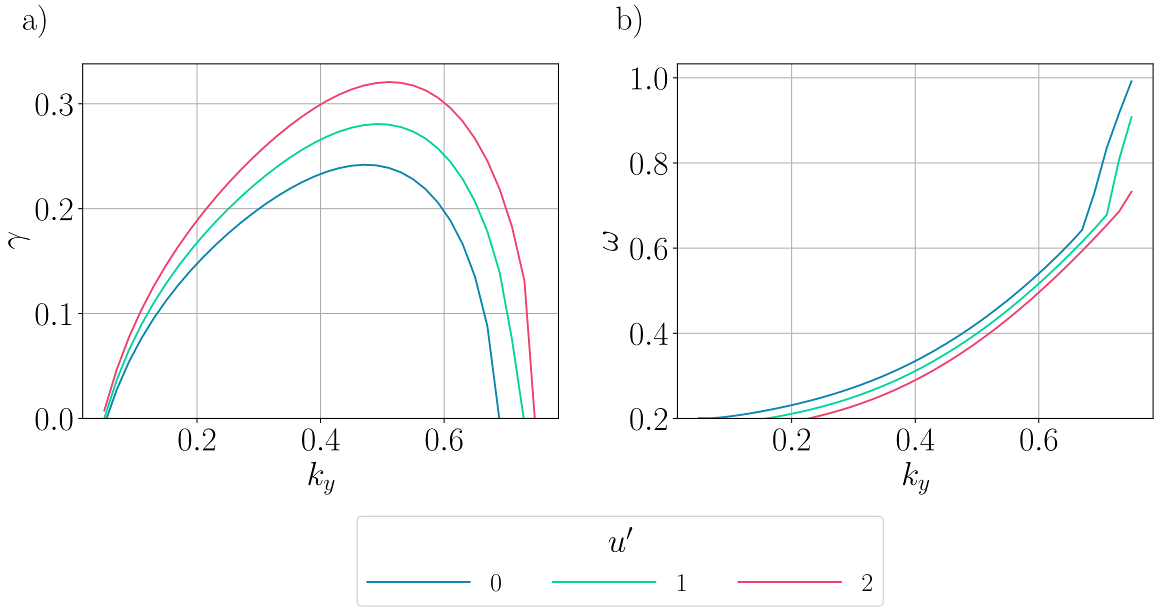

Figure C.2: Numerical solutions for a) growth-rate and b) real-frequency spectra in unsheared slab geometry with electrostatic fluctuations (including FLR effects). The fixed parameters for the deuterium-electron plasma shown are $T_i = T_e$, $n_e = n_i$, $L_{n_i}^{-1} = L_{n_e}^{-1} = 0$, $L_{T_i}^{-1} = 15$ $L_{T_e}^{-1} = 2$, $k_x = 0$ and $k_\parallel = 0.2$.

# Appendix D

# Purely-perpendicular flow shear

In this Appendix, we provide a possible explanation for the unexpected behaviour seen in Figures 3.10b) and 3.11b), whereby increasing $\gamma_{E\times B}$ from 0.04 to 0.08 led to increased Floquet-averaged growth rates at some values of $k_y$. `GS2` has no centrifugal term built into it, which might otherwise explain this observation. We begin with a simple thought experiment, which we will then tie into the implementation of flow shear when solving the gyrokinetic equation using `GS2`.

## D.1 Simple model

Consider a system that has the potential to support two modes labelled by their distinct eigenfunctions ($\hat{\chi}_1$, $\hat{\chi}_2$), with different real frequencies ($\omega_1$, $\omega_2$) and growth rates ($\gamma_1$, $\gamma_2$). Expressing the overall potential as a linear superposition of these eigenfunctions with complex coefficients $c_1$ and $c_2$ that are representative of the initial state, we can write an expression for the absolute value of the potential:

$$|\hat{\chi}|^2 = |c_1|^2\hat{\chi}_1^2\mathrm{e}^{2\gamma_1 t} + |c_2|^2\hat{\chi}_2^2\mathrm{e}^{2\gamma_2 t} + 2|c_1c_2^*|\hat{\chi}_1\hat{\chi}_2\mathrm{e}^{(\gamma_1+\gamma_2)t}\cos\big(\tau\big), \tag{D.1}$$

where $\tau \equiv t|\Delta\omega| \pm \arg[c_1c_2^*]$, $\Delta\omega \equiv \omega_1 - \omega_2$ and the $\pm$ corresponds to $\Delta\omega \gtrless 0$. The third term represents beating between the two competing modes and is a transient phenomenon that decays with a timescale that depends on the difference between the modes' growth rates. To see this, we consider a case where $\gamma_1 > \gamma_2$ and calculate the instantaneous growth rate of $|\hat{\chi}|$ as

$$\frac{d\log|\hat{\chi}|}{dt} = \gamma_1\left[1 - \frac{|A|\mathrm{e}^{-t\Delta\gamma}\Big(\frac{\Delta\gamma}{\gamma_1}\big(|A|\mathrm{e}^{-t\Delta\gamma}+\cos(\tau)\big) + \frac{|\Delta\omega|}{\gamma_1}\sin(\tau)\Big)}{1+|A|\mathrm{e}^{-t\Delta\gamma}\big[|A|\mathrm{e}^{-t\Delta\gamma}+2\cos(\tau)\big]}\right], \tag{D.2}$$

where $A^* \equiv c_2\hat{\chi}_2/c_1\hat{\chi}_1$, $\varphi \equiv \arg[A]$ and $\Delta\gamma \equiv \gamma_1 - \gamma_2$. In the case where $\gamma_1 \sim \gamma_2$, the growth-rate relative to $\gamma_1$ is a slowly-decaying oscillatory function with a frequency that tends to increase with the difference between the real-frequencies of the two modes. The amplitude of the oscillations also increases with $\Delta\omega$.

## D.2 Connection to `GS2`'s flow-shear algorithm

To tie this simple model for competing modes together with the effect of flow shear, we note that the only effect of perpendicular flow shear in `GS2` is to make $k_x$ time-dependent according to Equation 1.32. For all flow-shear simulations shown in this Thesis, $k_x$ changes continuously in time, however the original implementation in `GS2` was discrete [112]. For the purposes of this simple model of two competing modes, we invoke the discrete implementation of flow-shear as it is simpler to understand. In this algorithm, a finite number $N_0$ of extended $\theta$ domains are simulated, each of which can be labelled by a different value of $\theta_0$. During the course of one Floquet oscillation, $\theta_0$ for a given extended twist-and-shift chain changes with time. As an approximation, the nearest value of $\theta_0$ to the true value is used. This means that after one remapping time $t_r \equiv 2\pi/(N_0\gamma_{E\times B})$, a chain which evolves with one value of $\theta_0$ is mapped onto a chain with an adjacent value of $\theta_0$. This is a discrete process, and so at every remap, there will be a transient period whereby the initial state evolves towards the dominant eigenmode for the new value of $\theta_0$.

For an infinitesimally small perpendicular shearing rate such that $t_r \gg (\Delta\gamma)^{-1}$, each remap will occur long after the transient period has expired. The resultant average growth rate between remaps will therefore be $\gamma_1$, the growth rate of the dominant mode without flow shear. If the shearing rate is larger, such that $t_r \sim (\Delta\gamma)^{-1}$, remapping will truncate the transient period before it has completed. The average growth rate in this case is dependent on the amplitude of oscillations in the growth rate relative to $\gamma_1$, as well as the point in the transient period at which the truncation occurs. This truncation of the transient behaviour by increased perpendicular flow shear is critical to the stabilizing effect of increased perpendicular flow shear. It can also be used to

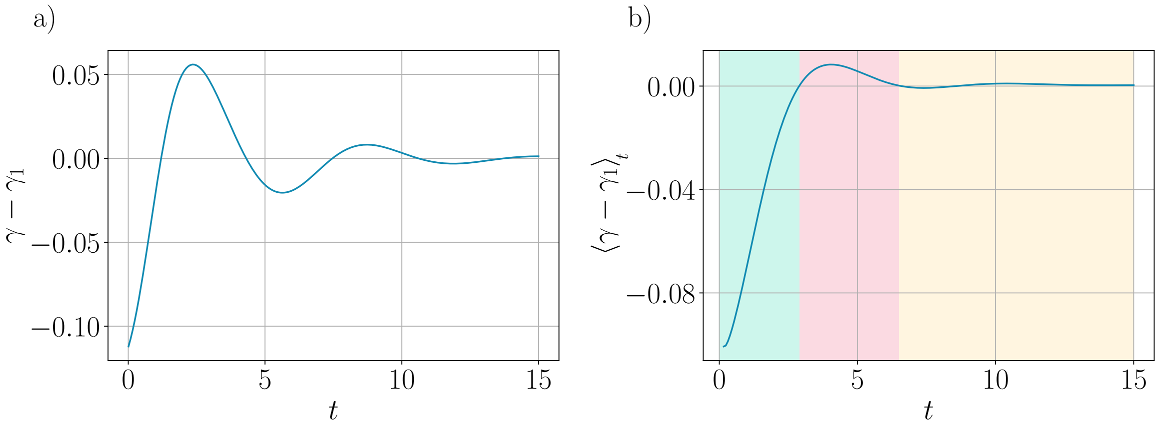

Figure D.1: Time traces of transient relaxation towards a dominant mode using Equation D.2 showing a) the growth rate relative to $\gamma_1$ and b) the average growth rate relative to $\gamma_1$. The colours of shaded regions in b) indicate the net effect of truncating the transience in each region – green indicates stabilization, red destabilization and yellow no significant change relative to $\gamma_1$. Large (small) truncation times, such as those in the yellow (green) region, correspond to a small (large) shearing rate. The parameters used to generate this Figure are $c_1 = 0.9$, $c_2 = -0.01 - 0.1i$, $\omega_1 = 0.5$, $\omega_2 = -0.5$, $\gamma_1 = 1.0$ and $\gamma_2 = 0.9$.

explain why in certain scenarios, an increased rate of purely-perpendicular equilibrium flow shear could have a destabilizing effect on the Floquet-averaged growth rate. This is illustrated schematically using Figure D.1, which shows a transient period and the associated average growth during that transient period, relative to the dominant growth rate $\gamma_1$. If $t_r$ lies in the red shaded region, the effect of perpendicular flow shear can be to increase the Floquet-averaged growth rate relative to the unsheared case. This is, of course, an overly simplistic model. The physical system can naturally support more than two modes, which complicates the picture mathematically. More importantly, the study of a single transient period cannot be used to prove that over the course of an entire Floquet period the average growth rate is increased above the unsheared case. Each transient phase is seeded via another (partially completed) previous one, creating a complex history of initial conditions $c_1$, $c_2$, etc. Interestingly, this model suggests that degenerate modes with the same growth rate but equal and opposite real frequencies could be particularly susceptible to the transient effects discussed above (since $\Delta\gamma \to 0$). This is particularly relevant to the equilibria studied in Chapter 3, since the slab-ITG auxiliary modes were found to be made up of two degenerate modes with opposing signs of $k_{\|}$ (and thus $\omega$).

# References

[1] M. Kotschenreuther, G. Rewoldt, and W. M. Tang. Comparison of initial value and eigenvalue codes for kinetic toroidal plasma instabilities. *Computer Physics Communications*, 88, 8 1995. ISSN 00104655. doi: 10.1016/0010-4655(95) 00035-E.

[2] W. Dorland, F. Jenko, M. Kotschenreuther, and B. N. Rogers. Electron temperature gradient turbulence. *Physical Review Letters*, 85:5579–5582, 12 2000. ISSN 0031-9007. doi: 10.1103/PhysRevLett.85.5579.

[3] V. Masson-Delmotte, P. Zhai, A. Pirani, et al. The physical science basis. Contribution of working group I to the sixth assessment report of the intergovernmental panel on climate change. Cambridge University Press, 2021.

[4] D. G. Infield. Summary report on the post-accident review meeting on the Chernobyl accident: Safety series no 75-INSAG-1. *Physics Bulletin*, 38:230–230, 6 1987. ISSN 0031-9112. doi: 10.1088/0031-9112/38/6/032.

[5] M. A. Delucchi and M. Z. Jacobson. Providing all global energy with wind, water, and solar power, part II: Reliability, system and transmission costs, and policies. *Energy Policy*, 39:1170–1190, 3 2011. ISSN 03014215. doi: 10.1016/j.enpol.2010.11.045.

[6] Jeff Tollefson and Elizabeth Gibney. Nuclear-fusion lab achieves 'ignition': what does it mean? *Nature*, 612(7941):597–598, December 2022.

[7] M. Keilhacker, A. Gibson, C. Gormezano, et al. High fusion performance from deuterium-tritium plasmas in JET. *Nuclear Fusion*, 39:209–234, 2 1999. ISSN 0029-5515. doi: 10.1088/0029-5515/39/2/306.

[8] R. J. Bickerton, J. W. Connor, and J. B. Taylor. Diffusion driven plasma currents and bootstrap tokamak. *Nature Physical Science*, 229:110–112, 1 1971. ISSN 0300-8746. doi: 10.1038/physci229110a0.

[9] M. D. Kruskal and R. M. Kulsrud. Equilibrium of a magnetically confined plasma in a toroid. *Physics of Fluids*, 1:265, 1958. ISSN 00319171. doi: 10.1063/1.1705884.

[10] H. Grad and H. Rubin. Proc. of the 2nd UN conf. on the peaceful uses of atomic energy 1-13 Sep Geneva, Switzerland vol 31. page p190, 1958. URL `https://inis.iaea.org/search/search.aspx?orig_q=RN:39082383`.

[11] V. D. Shafranov. Plasma equilibrium in a magnetic field. *Reviews of Plasma Physics*, 2:103, 1 1966.

[12] R. A. Pitts, A. Kukushkin, A. Loarte, et al. Status and physics basis of the ITER divertor. *Physica Scripta*, T138:014001, 12 2009. ISSN 0031-8949. doi: 10.1088/0031-8949/2009/T138/014001.

[13] P. N. Guzdar, L. Chen, W. M. Tang, and Rutherford P. H. Ion-temperature-gradient instability in toroidal plasmas. *Physics of Fluids*, 26:673, 1983. ISSN 00319171. doi: 10.1063/1.864182.

[14] F. Romanelli. Ion temperature-gradient-driven modes and anomalous ion transport in tokamaks. *Physics of Fluids B: Plasma Physics*, 1:1018–1025, 5 1989. ISSN 0899-8221. doi: 10.1063/1.859023.

[15] W. Horton. Drift waves and transport. *Reviews of Modern Physics*, 71:735–778, 4 1999. ISSN 0034-6861. doi: 10.1103/RevModPhys.71.735.

[16] J W Connor and H R Wilson. Survey of theories of anomalous transport. *Plasma Physics and Controlled Fusion*, 36:719–795, 5 1994. ISSN 0741-3335. doi: 10.1088/0741-3335/36/5/002.

[17] M. Ottaviani, M.A. Beer, S.C. Cowley, et al. Unanswered questions in ion-temperature-gradient-driven turbulence. *Physics Reports*, 283:121–146, 4 1997. ISSN 03701573. doi: 10.1016/S0370-1573(96)00056-7.

[18] H. Biglari, P. H. Diamond, and P. W. Terry. Influence of sheared poloidal rotation on edge turbulence. *Physics of Fluids B: Plasma Physics*, 2:1–4, 1 1990. ISSN 0899-8221. doi: 10.1063/1.859529.

[19] A. M. Dimits, G. Bateman, M. A. Beer, et al. Comparisons and physics basis of tokamak transport models and turbulence simulations. *Physics of Plasmas*, 7: 969–983, 3 2000. ISSN 1070-664X. doi: 10.1063/1.873896.

[20] Plamen G. Ivanov, A. A. Schekochihin, W. Dorland, et al. Zonally dominated dynamics and dimits threshold in curvature-driven itg turbulence. *Journal of Plasma Physics*, 86:855860502, 10 2020. ISSN 0022-3778. doi: 10.1017/S0022377820000938.

[21] I. G. Abel, G. G. Plunk, E. Wang, et al. Multiscale gyrokinetics for rotating tokamak plasmas: fluctuations, transport and energy flows. *Reports on Progress in Physics*, 76:116201, 11 2013. ISSN 0034-4885. doi: 10.1088/0034-4885/76/11/116201.

[22] M. A. Beer, S. C. Cowley, and G. W. Hammett. Field-aligned coordinates for nonlinear simulations of tokamak turbulence. *Physics of Plasmas*, 2:2687–2700, 8 1995. ISSN 1070-664X. doi: 10.1063/1.871232.

[23] N Christen. *Bistable turbulent transport in fusion plasmas with rotational shear*. PhD thesis, University of Oxford, 2021.

[24] Nicolas Christen, Michael Barnes, and Felix I. Parra. Continuous-in-time approach to flow shear in a linearly implicit local gyrokinetic code. *Journal of Plasma Physics*, 87:905870230, 4 2021. ISSN 0022-3778. doi: 10.1017/S0022377821000453.

[25] T. M. Antonsen, J. F. Drake, P. N. Guzdar, et al. Physical mechanism of enhanced stability from negative shear in tokamaks: Implications for edge transport and the L-H transition. *Physics of Plasmas*, 3, 6 1996. ISSN 1070-664X. doi: 10.1063/1.871928.

[26] M. A. Beer, G. W. Hammett, G. Rewoldt, et al. Gyrofluid simulations of turbulence suppression in reversed-shear experiments on the tokamak fusion test reactor. *Physics of Plasmas*, 4:1792–1799, 5 1997. ISSN 1070-664X. doi: 10.1063/1.872279.

[27] R. Koch. Plasma heating by neutral beam injection. *Fusion Science and Technology*, 45:183–192, 3 2004. ISSN 1536-1055. doi: 10.13182/FST04-A482.

[28] J. S. deGrassie, D. R. Baker, K. H. Burrell, et al. Toroidal rotation in neutral beam heated discharges in DIII-D. *Nuclear Fusion*, 43:142–156, 2 2003. ISSN 0029-5515. doi: 10.1088/0029-5515/43/2/307.

[29] P. J. Catto. Parallel velocity shear instabilities in an inhomogeneous plasma with a sheared magnetic field. *Physics of Fluids*, 16:1719, 1973. ISSN 00319171. doi: 10.1063/1.1694200.

[30] S. L. Newton, S. C. Cowley, and N. F. Loureiro. Understanding the effect of sheared flow on microinstabilities. *Plasma Physics and Controlled Fusion*, 52: 125001, 12 2010. ISSN 0741-3335. doi: 10.1088/0741-3335/52/12/125001.

[31] M. Artun and W. M. Tang. Gyrokinetic analysis of ion temperature gradient modes in the presence of sheared flows. *Physics of Fluids B: Plasma Physics*, 4: 1102–1114, 5 1992. ISSN 0899-8221. doi: 10.1063/1.860118.

[32] K. H. Burrell, T. N. Carlstrom, E. J. Doyle, et al. Physics of the L-mode to H-mode transition in tokamaks. *Plasma Physics and Controlled Fusion*, 34:1859–1869, 12 1992. ISSN 0741-3335. doi: 10.1088/0741-3335/34/13/014.

[33] K. H. Burrell, E. J. Doyle, P. Gohil, et al. Role of the radial electric field in the transition from L (low) mode to H (high) mode to VH (very high) mode in the DIII-D tokamak. *Physics of Plasmas*, 1:1536–1544, 5 1994. ISSN 1070-664X. doi: 10.1063/1.870705.

[34] K. C. Shaing, E. C. Crume, and W. A. Houlberg. Bifurcation of poloidal rotation and suppression of turbulent fluctuations: A model for the L-H transition in tokamaks. *Physics of Fluids B: Plasma Physics*, 2:1492–1498, 6 1990. ISSN 0899-8221. doi: 10.1063/1.859473.

[35] M. Barnes, F. I. Parra, E. G. Highcock, et al. Turbulent transport in tokamak plasmas with rotational shear. *Physical Review Letters*, 106:175004, 4 2011. ISSN 0031-9007. doi: 10.1103/PhysRevLett.106.175004.

[36] F. L. Waelbroeck, T. M. Antonsen, P. N. Guzdar, and A. B. Hassam. Theory of drift-acoustic instabilities in the presence of sheared flows. *Physics of Fluids B: Plasma Physics*, 4:2441–2447, 8 1992. ISSN 0899-8221. doi: 10.1063/1.860469.

[37] Alfven and H. On the existence of electromagnetic-hydromagnetic waves. *Arkiv. Mat. Astron. Fys*, 1943. URL `http://ci.nii.ac.jp/naid/10024498371/en/`.

[38] ITER Physics Expert Group. Chapter 3: Mhd stability, operational limits and disruptions. *Nuclear Fusion*, 39:2251–2389, 12 1999. ISSN 0029-5515. doi: 10.1088/0029-5515/39/12/303.

[39] J Weiland and A Hirose. Electromagnetic and kinetic effects on the ion temperature gradient mode. *Nuclear Fusion*, 32:151–155, 1 1992. ISSN 0029-5515. doi: 10.1088/0029-5515/32/1/I13.

[40] A. Hirose. On finite $\beta$ stabilization of the toroidal ion temperature gradient mode. *Physics of Plasmas*, 7:433–436, 2 2000. ISSN 1070-664X. doi: 10.1063/1.873866.

[41] J. Q. Dong, P. N. Guzdar, and Y. C. Lee. Finite beta effects on ion temperature gradient driven modes. *Physics of Fluids*, 30:2694–2702, 9 1987. ISSN 0031-9171. doi: 10.1063/1.866034.

[42] J. V. W. Reynders. Finite-$\beta$ modification of the ion-temperature-gradient-driven instability in a sheared slab geometry. *Physics of Plasmas*, 1:1953–1961, 6 1994. ISSN 1070-664X. doi: 10.1063/1.870651.

[43] J. Y. Kim, W. Horton, and J. Q. Dong. Electromagnetic effect on the toroidal ion temperature gradient mode. *Physics of Fluids B: Plasma Physics*, 5:4030–4039, 11 1993. ISSN 0899-8221. doi: 10.1063/1.860623.

[44] M. J. Pueschel, M. Kammerer, and F. Jenko. Gyrokinetic turbulence simulations at high plasma beta. *Physics of Plasmas*, 15:102310, 10 2008. ISSN 1070-664X. doi: 10.1063/1.3005380.

[45] J. Citrin, J. Garcia, T. Görler, et al. Electromagnetic stabilization of tokamak microturbulence in a high-$\beta$ regime. *Plasma Physics and Controlled Fusion*, 57: 014032, 1 2015. ISSN 0741-3335. doi: 10.1088/0741-3335/57/1/014032.

[46] M. J. Pueschel and F. Jenko. Transport properties of finite-$\beta$ microturbulence. *Physics of Plasmas*, 17:062307, 6 2010. ISSN 1070-664X. doi: 10.1063/1.3435280.

[47] M. J. Pueschel, T. Görler, F. Jenko, et al. On secondary and tertiary instability in electromagnetic plasma microturbulence. *Physics of Plasmas*, 20:102308, 10 2013. ISSN 1070-664X. doi: 10.1063/1.4825227. URL `http://aip.scitation.org/doi/10.1063/1.4825227`.

[48] P. B. Snyder and G. W. Hammett. Electromagnetic effects on plasma microturbulence and transport. *Physics of Plasmas*, 8:744–749, 3 2001. ISSN 1070-664X. doi: 10.1063/1.1342029.

[49] B. G. Hong, W. Horton, and D-I. Choi. Pressure gradient-driven modes in finite beta toroidal plasmas. *Plasma Physics and Controlled Fusion*, 31:1291–1303, 7 1989. ISSN 0741-3335. doi: 10.1088/0741-3335/31/8/006.

[50] F. Zonca, L. Chen, J. Q. Dong, and R. A. Santoro. Existence of ion temperature gradient driven shear alfvén instabilities in tokamaks. *Physics of Plasmas*, 6: 1917–1924, 5 1999. ISSN 1070-664X. doi: 10.1063/1.873449.

[51] E. A. Belli and J. Candy. Fully electromagnetic gyrokinetic eigenmode analysis of high-beta shaped plasmas. *Physics of Plasmas*, 17:112314, 11 2010. ISSN 1070-664X. doi: 10.1063/1.3495976.

[52] W. Guttenfelder, J. L. Peterson, J. Candy, et al. Progress in simulating turbulent electron thermal transport in NSTX. *Nuclear Fusion*, 53:093022, 9 2013. ISSN 0029-5515. doi: 10.1088/0029-5515/53/9/093022.

[53] B. Patel. Confinement physics for a steady state net electric burning spherical tokamak, 2021.

[54] C. Mercier. MHD stability criteria for localized displacements. *Proc 7th Int. Conf. on Plasma Physics and Controlled Nuclear Fusion (Innsbruck, 1986)*, 1: 701, 1978.

[55] A. Sykes, M. F. Turner, P. J. Fielding, and F. A. Haas. MHD theory of ballooning modes applied to JET, and the effect of anisotropic pressure on ballooning modes. *Proc 7th Int. Conf. on Plasma Physics and Controlled Nuclear Fusion (Innsbruck, 1986)*, page 625, 1978.

[56] L. E. Zakharov. High-wave-number MHD-mode stability in high-pressure tokamaks. *Proc 7th Int. Conf. on Plasma Physics and Controlled Nuclear Fusion (Innsbruck, 1986)*, 1:689, 1978.

[57] A. Hirose, L. Zhang, and M. Elia. Higher order collisionless ballooning mode in tokamaks. *Physical Review Letters*, 72, 6 1994. ISSN 0031-9007. doi: 10.1103/PhysRevLett.72.3993.

[58] O. Beeke, M. Barnes, M. Romanelli, et al. Impact of shaping on microstability in high-performance tokamak plasmas. *Nuclear Fusion*, 61:066020, 6 2021. ISSN 0029-5515. doi: 10.1088/1741-4326/abf660.

[59] J. E. Kinsey, R. E. Waltz, and J. Candy. The effect of plasma shaping on turbulent transport and E×B shear quenching in nonlinear gyrokinetic simulations. *Physics of Plasmas*, 14, 10 2007. ISSN 1070-664X. doi: 10.1063/1.2786857.

[60] E. A. Belli, G. W. Hammett, and W. Dorland. Effects of plasma shaping on nonlinear gyrokinetic turbulence. *Physics of Plasmas*, 15, 9 2008. ISSN 1070-664X. doi: 10.1063/1.2972160.

[61] P. Angelino, X. Garbet, L. Villard, et al. Role of plasma elongation on turbulent transport in magnetically confined plasmas. *Physical Review Letters*, 102, 5 2009. ISSN 0031-9007. doi: 10.1103/PhysRevLett.102.195002.

[62] J. Ball, F. I. Parra, M. Landreman, and M.l Barnes. Optimized up–down asymmetry to drive fast intrinsic rotation in tokamaks. *Nuclear Fusion*, 58, 2 2018. ISSN 0029-5515. doi: 10.1088/1741-4326/aa9a50.

[63] H. Weisen, J. Moret, S. Franke, et al. Effect of plasma shape on confinement and MHD behaviour in the TCV tokamak. *Nuclear Fusion*, 37, 12 1997. ISSN 0029-5515. doi: 10.1088/0029-5515/37/12/I07.

[64] Y. Camenen, A. Pochelon, R. Behn, et al. Impact of plasma triangularity and collisionality on electron heat transport in TCV L-mode plasmas. *Nuclear Fusion*, 47, 7 2007. ISSN 0029-5515. doi: 10.1088/0029-5515/47/7/002.

[65] A. Marinoni, M. E. Austin, A. W. Hyatt, et al. H-mode grade confinement in L-mode edge plasmas at negative triangularity on DIII-D. *Physics of Plasmas*, 26, 4 2019. ISSN 1070-664X. doi: 10.1063/1.5091802.

[66] A. Pochelon, T. P. Goodman, M. Henderson, et al. Energy confinement and MHD activity in shaped TCV plasmas with localized electron cyclotron heating. *Nuclear Fusion*, 39, 11 1999. ISSN 0029-5515. doi: 10.1088/0029-5515/39/11Y/321.

[67] J. Ball and F. I. Parra. Intuition for the radial penetration of flux surface shaping in tokamaks. *Plasma Physics and Controlled Fusion*, 57:035006, 3 2015. ISSN 0741-3335. doi: 10.1088/0741-3335/57/3/035006.

[68] F. Troyon, R. Gruber, H. Saurenmann, et al. MHD-limits to plasma confinement. *Plasma Physics and Controlled Fusion*, 26, 1 1984. ISSN 0741-3335. doi: 10.1088/0741-3335/26/1A/319.

[69] R. L. Miller, M. S. Chu, J. M. Greene, et al. Noncircular, finite aspect ratio, local equilibrium model. *Physics of Plasmas*, 5, 4 1998. ISSN 1070-664X. doi: 10.1063/1.872666.

[70] T. Watanabe and H. Sugama. Velocity–space structures of distribution function in toroidal ion temperature gradient turbulence. *Nuclear Fusion*, 46, 1 2006. ISSN 0029-5515. doi: 10.1088/0029-5515/46/1/003.

[71] M. Nakata, M. Nunami, T. Watanabe, and H. Sugama. Improved collision operator for plasma kinetic simulations with multi-species ions and electrons. *Computer Physics Communications*, 197, 12 2015. ISSN 00104655. doi: 10.1016/j.cpc.2015.08.007.

[72] M. Nakata, A. Matsuyama, N. Aiba, et al. Local gyrokinetic vlasov simulations with realistic tokamak MHD equilibria. *Plasma and Fusion Research*, 9:1403029–1403029, 2014. ISSN 1880-6821. doi: 10.1585/pfr.9.1403029.

[73] C. M. Roach, D. Dickinson, and D. J. Applegate. GS2Tools, 2019. URL `https://git.ccfe.ac.uk/croach/GS2TOOLS`.

[74] D. R. Mikkelsen, M. Nunami, T. Watanabe, et al. Verification of gyrokinetic microstability codes with an LHD configuration. *Physics of Plasmas*, 21, 11 2014. ISSN 1070-664X. doi: 10.1063/1.4902124.

[75] M. Nakata, M. Nunami, H. Sugama, and T. Watanabe. Isotope effects on trapped-electron-mode driven turbulence and zonal flows in helical and tokamak plasmas. *Physical Review Letters*, 118, 4 2017. ISSN 0031-9007. doi: 10.1103/PhysRevLett.118.165002.

[76] F. Wagner, G. Becker, K. Behringer, et al. Regime of improved confinement and high beta in neutral-beam-heated divertor discharges of the ASDEX tokamak. *Physical Review Letters*, 49:1408–1412, 11 1982. ISSN 0031-9007. doi: 10.1103/PhysRevLett.49.1408.

[77] J. W. Connor, T. Fukuda, X. Garbet, et al. A review of internal transport barrier physics for steady-state operation of tokamaks. *Nuclear Fusion*, 44:R1–R49, 4 2004. ISSN 0029-5515. doi: 10.1088/0029-5515/44/4/R01.

[78] E. J. Synakowski, S. H. Batha, M. A. Beer, et al. Local transport barrier formation and relaxation in reverse-shear plasmas on the Tokamak Fusion Test Reactor. *Physics of Plasmas*, 4:1736–1744, 5 1997. ISSN 1070-664X. doi: 10.1063/1.872275.

[79] S. Ide. Latest progress in steady state plasma research on the Japan Atomic Energy Research Institute Tokamak-60 Upgrade. *Physics of Plasmas*, 7:1927–1934, 5 2000. ISSN 1070-664X. doi: 10.1063/1.874017.

[80] C. M. Greenfield, M. Murakami, J. R. Ferron, et al. High performance advanced tokamak regimes in DIII-D for next-step experiments. *Physics of Plasmas*, 11: 2616–2626, 5 2004. ISSN 1070-664X. doi: 10.1063/1.1692133.

[81] C. M. Greenfield, D. P. Schissel, B. W. Stallard, et al. Transport and performance in DIII-D discharges with weak or negative central magnetic shear. *Physics of Plasmas*, 4:1596–1604, 5 1997. ISSN 1070-664X. doi: 10.1063/1.872360.

[82] E. J. Strait, L. L. Lao, M. E. Mauel, et al. Enhanced confinement and stability in DIII-D discharges with reversed magnetic shear. *Physical Review Letters*, 75: 4421–4424, 12 1995. ISSN 0031-9007. doi: 10.1103/PhysRevLett.75.4421.

[83] T. Fujita, S. Ide, H. Shirai, et al. Internal transport barrier for electrons in jt-60u reversed shear discharges. *Physical Review Letters*, 78:2377–2380, 3 1997. ISSN 0031-9007. doi: 10.1103/PhysRevLett.78.2377.

[84] F. M. Levinton, M. C. Zarnstorff, S. H. Batha, et al. Improved confinement with reversed magnetic shear in TFTR. *Physical Review Letters*, 75:4417–4420, 12 1995. ISSN 0031-9007. doi: 10.1103/PhysRevLett.75.4417.

[85] Y. Koide, M. Kikuchi, M. Mori, et al. Internal transport barrier on q=3 surface and poloidal plasma spin up in JT-60U high-$\beta_p$ discharges. *Physical Review Letters*, 72:3662–3665, 6 1994. ISSN 0031-9007. doi: 10.1103/PhysRevLett.72.3662.

[86] S. J. Wukitch, R. L. Boivin, P. T. Bonoli, et al. Double transport barrier experiments on Alcator C-Mod. *Physics of Plasmas*, 9:2149–2155, 5 2002. ISSN 1070-664X. doi: 10.1063/1.1467347.

[87] C. L. Fiore, P. T. Bonoli, D. R. Ernst, et al. Control of internal transport barriers on Alcator C-Mod. *Physics of Plasmas*, 11:2480–2487, 5 2004. ISSN 1070-664X. doi: 10.1063/1.1652785.

[88] K. H. Burrell. Effects of E×B velocity shear and magnetic shear on turbulence and transport in magnetic confinement devices. *Physics of Plasmas*, 4:1499–1518, 5 1997. ISSN 1070-664X. doi: 10.1063/1.872367.

[89] G. D. Conway, D. N. Borba, B. Alper, et al. Suppression of plasma turbulence during optimized shear configurations in JET. *Physical Review Letters*, 84:1463–1466, 2 2000. ISSN 0031-9007. doi: 10.1103/PhysRevLett.84.1463.

[90] G. Tresset, X. Litaudon, D. Moreau, et al. A dimensionless criterion for characterizing internal transport barriers in JET. *Nuclear Fusion*, 42:304, 5 2002. ISSN 00295515. doi: 10.1088/0029-5515/42/5/304.

[91] C. D. Challis, Y. F. Baranov, G. D. Conway, et al. Effect of q-profile modification by LHCD on internal transport barriers in JET. *Plasma Physics and Controlled Fusion*, 43:861–879, 7 2001. ISSN 0741-3335. doi: 10.1088/0741-3335/43/7/303.

[92] J W Connor, G Bracco, R J Buttery, et al. EU-US transport task force workshop on transport in fusion plasmas, Transport barrier physics, Varenna, 4-7 September 2000. *Plasma Physics and Controlled Fusion*, 43:355–368, 3 2001. ISSN 0741-3335. doi: 10.1088/0741-3335/43/3/310.

[93] M. Romanelli, A. Zocco, and F. Crisanti. Fast ion stabilization of the ion temperature gradient driven modes in the Joint European Torus hybrid-scenario plasmas: a trigger mechanism for internal transport barrier formation. *Plasma Physics and Controlled Fusion*, 52:045007, 4 2010. ISSN 0741-3335. doi: 10.1088/0741-3335/52/4/045007.

[94] A. Di Siena, R. Bilato, T. Görler, et al. New high-confinement regime with fast ions in the core of fusion plasmas. *Physical Review Letters*, 127:025002, 7 2021. ISSN 0031-9007. doi: 10.1103/PhysRevLett.127.025002.

[95] X. Litaudon, F. Crisanti, B. Alper, et al. Towards fully non-inductive current drive operation in JET. *Plasma Physics and Controlled Fusion*, 44:302, 7 2002. ISSN 07413335. doi: 10.1088/0741-3335/44/7/302.

[96] J. Pamela and JET EFDA Contributors. Overview of jet results ov/1-4. 2003.

[97] J. Mailloux, B. Alper, Y. Baranov, et al. Progress in internal transport barrier plasmas with lower hybrid current drive and heating in jet (joint european torus). *Physics of Plasmas*, 9(5):2156–2164, 2002. doi: 10.1063/1.1469026.

[98] C. D. Challis, X. Litaudon, G. Tresset, et al. Influence of the q-profile shape on plasma performance in JET. *Plasma Physics and Controlled Fusion*, 44:301, 7 2002. ISSN 07413335. doi: 10.1088/0741-3335/44/7/301.

[99] S. Ide, O. Naito, T. Fujita, et al. Application of LHCD to sustainment and control of a reversed magnetic shear plasma in JT-60U. *Proc. 16th Int. Conf. on Fusion Energy (Montreal, 1996)*, 3:253–264, 1997.

[100] G. Cenacchi and A. Taroni. JETTO: A free boundary plasma transport code (basic version). *ENEA, ISSN/0393-6633*, 1988.

[101] L. L. Lao, H. St. John, R. D. Stambaugh, et al. Reconstruction of current profile parameters and plasma shapes in tokamaks. *Nuclear Fusion*, 25:1611–1622, 11 1985. ISSN 0029-5515. doi: 10.1088/0029-5515/25/11/007.

[102] C. D. Challis, J. G. Cordey, H. Hamnén, et al. Non-inductively driven currents in JET. *Nuclear Fusion*, 29:563–570, 4 1989. ISSN 0029-5515. doi: 10.1088/0029-5515/29/4/002.

[103] A. R. Esterkin and A. D. Piliya. Fast ray tracing code for LHCD simulations. *Nuclear Fusion*, 36:1501–1512, 11 1996. ISSN 0029-5515. doi: 10.1088/0029-5515/36/11/I05.

[104] L. Eriksson, T. Hellsten, and U. Willen. Comparison of time dependent simulations with experiments in ion cyclotron heated plasmas. *Nuclear Fusion*, 33: 1037–1048, 7 1993. ISSN 0029-5515. doi: 10.1088/0029-5515/33/7/I07.

[105] A. Baciero. Profile maker, 2008.

[106] T Fujita, S. Ide, H. Kimura, et al. Enhanced core confinement in jt-60u reversed shear discharges. *Proc 16th Int. Conf., Fusion Energy (Montreal, 1996)*, 1:227, 1997.

[107] R C Wolf. Internal transport barriers in tokamak plasmas*. *Plasma Physics and Controlled Fusion*, 45:R1–R91, 1 2003. ISSN 0741-3335. doi: 10.1088/0741-3335/45/1/201.

[108] S. C. Cowley, R. M. Kulsrud, and R. Sudan. Considerations of ion-temperature-gradient-driven turbulence. *Physics of Fluids B: Plasma Physics*, 3:2767–2782, 10 1991. ISSN 0899-8221. doi: 10.1063/1.859913.

[109] J. Parisi, F. I. Parra, C. M. Roach, et al. Toroidal and slab ETG instability dominance in the linear spectrum of JET-ILW pedestals. *Nuclear Fusion*, 60: 126045, 12 2020. ISSN 0029-5515. doi: 10.1088/1741-4326/abb891.

[110] R. E. Waltz, R. L. Dewar, and X. Garbet. Theory and simulation of rotational shear stabilization of turbulence. *Physics of Plasmas*, 5:1784–1792, 5 1998. ISSN 1070-664X. doi: 10.1063/1.872847.

[111] M. D. H. Cole, S. L. Newton, S. C. Cowley, et al. Electromagnetic effects in the stabilization of turbulence by sheared flow. *Plasma Physics and Controlled Fusion*, 56, 1 2014. ISSN 015007. doi: 10.1088/0741-3335/56/1/015007.

[112] G. W. Hammett, W. Dorland, N. F. Loureiro, and T. Tatsuno. Implementation of large scale E×B shear flow in the GS2 gyrokinetic turbulence code, 2006.

[113] C M Roach, I G Abel, R J Akers, et al. Gyrokinetic simulations of spherical tokamaks. *Plasma Physics and Controlled Fusion*, 51(12):124020, nov 2009. doi: 10.1088/0741-3335/51/12/124020. URL `https://dx.doi.org/10.1088/0741-3335/51/12/124020`.

[114] A. Casati, C. Bourdelle, X. Garbet, and F. Imbeaux. Temperature ratio dependence of ion temperature gradient and trapped electron mode instability thresholds. *Physics of Plasmas*, 15:042310, 2008. ISSN 1070664X. doi: 10.1063/1.2906223.

[115] R. Courant, K. Friedrichs, and H. Lewy. On the partial difference equations of mathematical physics. *IBM Journal of Research and Development*, 11:215–234, 3 1967. ISSN 0018-8646. doi: 10.1147/rd.112.0215.

[116] Y Chen, S.E Parker, B.I Cohen, et al. Simulations of turbulent transport with kinetic electrons and electromagnetic effects. *Nuclear Fusion*, 43:1121–1127, 10 2003. ISSN 0029-5515. doi: 10.1088/0029-5515/43/10/013.

[117] R. E. Waltz. Nonlinear subcritical magnetohydrodynamic beta limit. *Physics of Plasmas*, 17:072501, 7 2010. ISSN 1070-664X. doi: 10.1063/1.3449075.

[118] M. J. Pueschel, D. R. Hatch, T. Görler, et al. Properties of high-beta microturbulence and the non-zonal transition. *Physics of Plasmas*, 20:102301, 10 2013. ISSN 1070-664X. doi: 10.1063/1.4823717.

[119] W. M. Nevins, E. Wang, and J. Candy. Magnetic stochasticity in gyrokinetic simulations of plasma microturbulence. *Physical Review Letters*, 106:065003, 2 2011. ISSN 0031-9007. doi: 10.1103/PhysRevLett.106.065003.

[120] V.D. Shafranov. About the stability of the plasma column in the presence of a longitudinal magnetic field and the conductive casing. *At. Energy*, 1:38, 1956.

[121] M. Kruskal and J. L. Tuck. The instability of a pinched fluid with a longitudinal magnetic field. *Proceedings of the Royal Society of London. Series A. Mathematical and Physical Sciences*, 245:222–237, 6 1958. ISSN 0080-4630. doi: 10.1098/rspa.1958.0079.

[122] E. G. Highcock, M. Barnes, A. A. Schekochihin, et al. Transport bifurcation in a rotating tokamak plasma. *Physical Review Letters*, 105:215003, 11 2010. ISSN 0031-9007. doi: 10.1103/PhysRevLett.105.215003.

[123] A. A. Schekochihin, E. G. Highcock, and S. C. Cowley. Subcritical fluctuations and suppression of turbulence in differentially rotating gyrokinetic plasmas. *Plasma Physics and Controlled Fusion*, 54:055011, 5 2012. ISSN 0741-3335. doi: 10.1088/0741-3335/54/5/055011.

[124] M. Barnes, I. G. Abel, W. Dorland, et al. Direct multiscale coupling of a transport code to gyrokinetic turbulence codes. *Physics of Plasmas*, 17:056109, 5 2010. ISSN 1070-664X. doi: 10.1063/1.3323082.

[125] P. Helander. Available energy and ground states of collisionless plasmas. *Journal of Plasma Physics*, 83:715830401, 8 2017. ISSN 0022-3778. doi: 10.1017/S0022377817000496.